Interface Effects in $Y_2Zr_2O_7$ Thin Films

Elisa Gilardi

Max-Planck-Institut für Festkörperforschung
Dissertation an der Universität Stuttgart
2016

Interface Effects in $Y_2Zr_2O_7$ Thin Films

Von der Fakultät Chemie der Universität Stuttgart
zur Erlangung der Würde eines

Doktors der Naturwissenschaft (Dr. rer. nat.)

genehmigte Abhandlung

Vorgelegt von

Elisa Gilardi

aus Vigevano, Italien

Hauptberichter:	Prof. Dr. Joachim Maier
Mitberichter:	Prof. Dr. Anke Weidenkaff
Prüfungsvorsitzeder:	Prof. Dr. Thomas Schleid
Tag der Einreichung:	09.11.2015
Tag der mündliche Prüfung:	07.01.2016

Max-Planck-Institut für Festkörperforschung
Universität Stuttgart

2016

Erklärung über die Eigensändigkeit der Dissertation

Ich versichere, dass ich die vorliegende Arbeit mit dem Titel 'Interface Effects in $Y_2Zr_2O_7$ Thin Films' selbständig verfasst und keine andere angegebenen Quellen und Hilfsmittel benutzt habe; aus fremden Quelle entnommene Passagen und Gedanken sind als solche kenntlich gemacht.

Declaration of Authorship

I hereby certify that the dissertation entitled 'Interface Effects in $Y_2Zr_2O_7$ Thin Films' is entirely my own work except where otherwise indicated. Passages and ideas from other sources have been clearly indicated.

Name/Name: Elisa Gilardi

Unterschrift/Signed:

Datum/Date: 09.11.2015

TABLE OF CONTENTS

ABSTRACT

The study of thin films and heterostructures has been extensively used in recent years to investigate the relevance of grain boundaries and interface effects (film/film and film/substrate) on the ionic transport properties of several oxides. It is worth noting that thanks to their configuration such systems allow for the direct investigation of aspects (e.g. interface effects in epitaxial films) that otherwise are not easily accessible in ceramics. In this way, it is possible to study for example the redistribution of charge carriers due to space charge effects (heterogeneous doping) or the enhancement of the ionic migration owing to strain effects.

This thesis focuses on the study of selected ionically conducting thin films and multilayers, with the aim of investigating the role of interface effects (both space charge and strain effects) on the overall ionic transport properties.

In order to address these aspects, the defective fluorite $Y_2Zr_2O_7$ has been taken as a model system, because of its high chemical stability and substantial ionic conductivity (*via* oxygen vacancies). Thanks to these properties, this oxide has been considered also as possible candidate for applications as electrolyte in solid oxide fuel cells (SOFCs). While for others $A_2B_2O_7$ compositions many contributions can be found in the literature, there is a substantial lack of information about $Y_2Zr_2O_7$.

The first part of this work deals with the investigation of the electrical properties of $Y_2Zr_2O_7$ both ceramics pellet and thin films with different microstructures (epitaxial vs. textured). As epitaxial layers can be considered structurally similar to single crystals, the comparison between textured and epitaxial films allowed for obtaining important information on the role of grain boundaries on the overall ionic transport.

In particular, textured thin films of 100 nm thickness have been grown via pulsed laser deposition (PLD) technique on Al_2O_3 (0 0 0 1) and Al_2O_3 (1 -1 0 2) while it was possible to obtain epitaxial thin films on MgO (1 1 0). The microstructure of the films was characterized by X - ray diffraction (XRD), pole figures, high resolution transmission electron microscopy (HR - TEM) and atomic force microscopy (AFM).

XRD characterization indicated a preferential alignment along the (1 1 1) direction on both Al_2O_3 (0 0 0 1) and Al_2O_3 (1 -1 0 2) with a minor (2 2 0) orientation. Pole figures on Al_2O_3 (0 0 0 1) confirmed the textured structure of the films.

Samples grown on MgO (1 1 0) instead were epitaxial, oriented along the (1 1 0) direction. Pole figures and HR-TEM analysis confirmed the single orientation of the crystallographic planes and the absence of grain boundaries. AFM images indicated a uniform surface with low roughness (RMS on the order of one unit cell) on all $Y_2Zr_2O_7$ thin films.

The electrical properties were analyzed via electrochemical impedance spectroscopy (EIS) at different temperatures and different oxygen partial pressures. Remarkably, the comparison of the Arrhenius plots obtained from ceramic pellet, textured and epitaxial thin films pointed out a minor blocking effect of the grain boundaries on the ionic conductivity. Only a small difference in conductivity and activation energy was detected between these samples.

A further detailed study of the electrical properties of $Y_2Zr_2O_7$ thin films was carried out by analyzing the conductances of epitaxial layers of different thickness (from 70 nm up to 300 nm). The EIS measurement revealed a significant enhancement of the conductance at the interface between the $Y_2Zr_2O_7$ layer and the MgO substrate. After annealing at high temperature (700 °C) for several hours there was a clear decrease of the interfacial conductance. Along with this, HR-TEM analysis showed a high density of misfit dislocations at the interface, which is structurally required to release the compressive strain stemming from the large mismatch between film and substrate. Interestingly, the misfit dislocation density also decreased after annealing.

These results are complemented by electron energy-loss spectroscopy (EELS) measurements performedat the O-*K*-edge (1*s* to 2*p* electronic transition). The analysis of the spectra revealed an increase of the oxygen first peak intensity (stemming from the transitions to the *d*-states of Zr hybridized with oxygen 2*p* states) near the $Y_2Zr_2O_7$/MgO interface in the samples not exposed to the heat-treatment at 700 °C, indicating a different local environment surrounding the oxygen ions. This enhancement does not appear in the samples after annealing.

The interpretation of the enhanced interfacial conductance takes into account both space-charge and mobility effects. The segregation of negatively charged defects at the interface yielding the accumulation of $V_O^{\bullet\bullet}$ in the space charge zone can only partially explain the experimental results. Indeed, an additional increase in the charge carriers' mobility also emerges from the analysis of the conductance as function of the film thickness.

The interface structural modifications after annealing (lower misfit dislocation density) together with the strain relaxation (decreased mobility) can explain the variation in conductance.

For the study of the effect of the strain on the ionic conductivity, multilayers of $Y_2Zr_2O_7$ and 8 mol% yttria stabilized zirconia with different number of interfaces but same overall thickness have been deposited (from 1 up to 9 interfaces) and characterized *via* EIS and XRD. For comparison, also single layers have been included in the measurement. XRD characterization indicated the epitaxial growth of multilayers along the (1 1 0) orientation and high quality of the interfaces. Remarkably, the EIS characterization pointed out a negligible role of the strain on the ionic conductivity despite the substantial lattice mismatch of 1.6%.

ZUSAMMENFASSUNG

Dünne Schichten und Heterostrukturen wurden in den letzten Jahren ausgiebig genutzt, um die Bedeutung von Korngrenz- und Grenzflächeneffekten (zwischen zwei Schichten und zwischen Schicht und Substrat) für die ionischen Transporteigenschaften von verschiedenen Oxiden zu untersuchen. Es ist bemerkenswert, dass diese Systeme dank ihrer Struktur die direkte Untersuchung von Aspekten (wie zum Beispiel Grenzflächeneffekten in epitaktischen Schichten) ermöglichen, welche ansonsten in Keramiken nicht einfach zugänglich sind. Auf diese Art und Weise ist es möglich, zum Beispiel die Umverteilung von Ladungsträgern aufgrund von Raumladungseffekten (heterogene Dotierung) oder die Erhöhung der Ionenwanderung infolge von Spannungseffekten zu untersuchen.

Die vorliegende Arbeit konzentriert sich auf die Untersuchung von ausgewählten ionisch leitenden dünnen Schichten und Multilayers, mit dem Ziel den Einfluss von Grenzflächeneffekten (sowohl Raumladungs- als auch Spannungseffekte) auf die ionischen Transporteigenschaften zu erforschen.

Aufgrund ihrer hohen chemischen Stabilität und beachtlichen ionischen Leitfähigkeit (durch Sauerstoffleerstellen) wurde die Defektfluoritverbindung $Y_2Zr_2O_7$ als Modellmaterial verwendet. Dank der oben genannten Eigenschaften wurde dieses Oxid auch als potenzieller Elektrolyt für Festoxidbrennstoffzellen berücksichtigt. Während es für andere $A_2B_2O_7$-Verbindungen viele Beiträge in der Literatur gibt, mangelt es erheblich an Informationen über $Y_2Zr_2O_7$.

Im ersten Teil dieser Dissertation werden die elektrischen Eigenschaften von keramischen Presslingen und dünnen Schichten aus $Y_2Zr_2O_7$ mit unterschiedlichen Mikrostrukturen (epitaktisch und texturiert) erforscht. Da epitaktische Schichten

strukturell ähnlich wie Einkristalle betrachtet werden können, liefert der Vergleich von epitaktischen und texturierten Proben wichtige Informationen über den Effekt der Korngrenzen auf die gesamte ionische Leitung.

Insbesondere wurden texturierte Schichten mit einer Dicke von 100 nm mittels Laserablation auf Al_2O_3 (0001) und Al_2O_3 (1-102) abgeschieden, während es möglich war, epitaktische Filme auf MgO (110) herzustellen. Die Mikrostruktur der Proben wurde mittels Röntgenbeugung, Polfiguren, hochaufgelöster Transmissionselektronenmikroskopie und Rasterkraftmikroskopie charakterisiert.

Die Röntgenstrukturanalyse ergab eine bevorzugte Orientierung entlang der (111) Richtung auf Al_2O_3 (0001) und Al_2O_3(1-102) mit einem geringen Anteil an (220) Orientierung. Polfiguren an Al_2O_3 (0001) bestätigen den texturierten Charakter der Schichten. Proben, die auf MgO (110) abgeschieden wurden, waren stattdessen epitaktisch und entlang der (110) Richtung orientiert. Die Polfiguren und Untersuchungen mittels hochaufgelöster Transmissionselektronenmikroskopie bestätigten die Ausrichtung der kristallographischen Ebenen und die Abwesenheit von Korngrenzen. Mittels Rasterkraftmikroskopie aufgenommene Bilder zeigten für alle $Y_2Zr_2O_7$-Dünnschichten eine gleichmäßige Oberfläche mit geringer Rauigkeit auf (Mittelrauwert in der Größenordnung einer Elementarzelle).

Die elektrischen Eigenschaften der Dünnschichten wurden mittels Impedanzspektroskopie bei verschiedenen Temperaturen und Sauerstoffpartialdrücken untersucht. Bemerkenswerterweise zeigt der Vergleich der Daten von keramischem Pressling, texturierten und epitaktischen Schichten nur einen leicht blockierenden Effekt der Korngrenzen auf die ionische Leitfähigkeit. Nur ein geringer Unterschied in Leitfähigkeit und Aktivierungsenergie zwischen diesen Proben wurde beobachtet.

Eine weitere ausführliche Untersuchung der elektrischen Eigenschaften von $Y_2Zr_2O_7$-Dünnschichten wurde durchgeführt, indem die Leitfähigkeiten von epitaktischen Schichten verschiedener Dicke (70 nm bis 300 nm) analysiert wurden. Die Impedanzmessung zeigte eine wesentliche Erhöhung der Leitfähigkeit an der Grenzfläche zwischen der $Y_2Zr_2O_7$-Schicht und dem MgO-Substrat. Nach Glühen bei hoher Temperatur (700°C) über mehrere Stunden ergibt sich ein deutlicher Abfall der Grenzflächenleitfähigkeit. Weiterhin zeigte die Analyse mit hochaufgelöster

Transmissionselektronenmikroskopie eine hohe Dichte an Fehlanpassungsversetzungen an der Grenzfläche, welche strukturell notwendig sind, um die Druckspannung, die von der großen Fehlanpassung zwischen Schicht und Substrat stammt, abzubauen. Interessanterweise nahm die Dichte der Fehlanpassungsversetzungen auch nach dem Glühen ab.

Diese Ergebnisse werden ergänzt von Elektronenenergieverlustspektroskopiemessungen die an der O-*K*-Kante durchgeführt wurden (1*s* zu 2*p* Elektronenübergang). Die Auswertung der Spektren ergab eine Erhöhung der Intensität des ersten Sauerstoffpeaks (dieser stammt vom Übergang zu den *d*-Zuständen von Zr hybridisiert mit Sauerstoff 2*p*-Zuständen) nahe der $Y_2Zr_2O_7$/MgO-Grenzfläche in den Proben die nicht bei 700°C ausgelagert wurden, was auf eine andere lokale Umgebung der Sauerstoffionen hinweist. Diese Erhöhung tritt in den ausgelagerten Proben nicht auf.

Die Interpretation der erhöhten Grenzflächenleitfähigkeit berücksichtigt sowohl Raumladungs- als auch Mobilitätseffekte. Die Segregation von negativ geladenen Defekten an der Grenzfläche, was zur Anhäufung von Sauerstoffleerstellen in der Raumladungszone führt, kann nur teilweise die experimentellen Ergebnisse erklären. Tatsächlich ergibt sich eine weitere Zunahme der Mobilität der Ladungsträger aus der Analyse der Leitfähigkeit als Funktion der Schichtdicke.

Die strukturellen Veränderungen der Grenzfläche nach dem Glühen (geringere Dichte der Fehlanpassungsversetzungen) können, zusammen mit der Relaxation der Spannung (verringerte Mobilität), die Veränderungen in der Leitfähigkeit erklären.

Zur Untersuchung des Einfluss der Spannung auf die ionische Leitfähigkeit wurden Multilayers aus $Y_2Zr_2O_7$ und 8 mol% Yttrium-dotiertem Zirkonoxid mit unterschiedlicher Anzahl an Grenzflächen aber gleicher Gesamtschichtdicke abgeschieden (eine bis neun Grenzflächen) und mittels Impedanzspektroskopie und Röntgenbeugung charakterisiert. Zum Vergleich wurden auch Einzelschichten untersucht. Die Analyse mittels Röntgenbeugung zeigt ein epitaktisches Wachstum der Multilayer entlang der (110) Richtung und eine hohe Qualität der Grenzflächen. Bemerkenswerterweise ergibt sich aus den Ergebnissen der Impedanzspektroskopie nur ein vernachlässigbarer Effekt der Spannung auf die ionische Leitfähigkeit, trotz der deutlichen Gitterfehlanpassung von 1,6%.

1 INTRODUCTION

Thin films and multilayered hetero-structures of mixed and ionic conducting oxides have attracted growing attention in the recent years. This is related to the numerous fields of application, in which oxide thin films play a crucial role: e.g. conductive transparent layers for photovoltaic applications [1, 2], micro solid oxide fuel cells (μ-SOFC) [3, 4], gas sensors [5, 6], solid state lithium batteries [7] and resistive switching [8, 9]. As far as ionically conducting oxides are concerned, one should note that thanks to the reduced thickness of the electrolyte, thin films can allow for successfully diminishing the operation temperature of μ-SOFC down to the intermediate temperature range (500°-700°) [2, 8]. Another important advantage of dealing with thin films is that they offer the possibility of (i) obtaining samples with specific and unique geometries (e.g. multilayers systems) and (ii) investigating peculiar physicochemical properties, which are not easily accessible in ceramics as for example the role of strain [10] and interface effects [11] or the comparison between polycrystalline materials and epitaxial films (serving as single crystals) [4, 12-15].

As pointed out below, this thesis presents a series of studies on selected ionically conducting thin films and multilayers, which were performed with the purpose of investigating the role of interface effects (both space charge and strain effects) on the overall ionic transport. In the following different interface effects which are relevant in the framework of the present study are described.

1.1 Interface effects and ionic conductivity

Various effects are known, both structural and electrostatic, that can modify the ionic transport mechanism at interfaces.

The structural effects (strain) stem mainly from the crystallographic mismatch between thin film and substrate (i.e. the difference of the lattice parameters) [11].

It is known from thermodynamic considerations that strain in thin films could have a significant impact on the ionic transport properties of materials [16-20]. This has been experimentally observed in many multilayer systems, in particular for oxygen vacancy conducting materials, in which tensile (or compressive) strain had a beneficial (or detrimental) effect on the conductivity. For example the comparison between multilayers of YSZ/Sc_2O_3, YSZ/Lu_2O_3 and YSZ/Y_2O_3, in which the mismatch between YSZ and the second oxide progressively increased from –4.28 % (meaning that the film was under compression) to +1.02 % and finally to +3.09 %, showed a corresponding improvement of the conductivity resulting from the variation of the mismatch from compressive to tensile [16]. A similar effect has been observed in YSZ/$Gd_2Zr_2O_7$ multilayers, with an increased ionic conductivity attributed to the tensilely strained YSZ layer [21]. However, as it has been pointed out in recent review articles (see Ref. [22] and Ref. [23]), the impact of strain effects on the ionic transport is rather unclear. An emblematic example in this sense is given by a recent study on epitaxial multilayers of CeO_2/8YSZ, in which - despite the existing literature in related systems - only marginal effects of the lattice tensile strain on the ionic transport were observed [24]. This points towards the need for additional studies on the role of strain effects on the conductivity, in which great care should be given at investigating films with the proper microstructure (epitaxial) and at fully characterizing the film/substrate interface, since the presence of possible misfit dislocations might release part of the nominal misfit strain) [22, 25].

As a matter of fact, a large mismatch between film and substrate or two adjacent layers cannot be completely accommodated by the elastic strain but rather by the formation of misfit dislocations at the interface. Only recently, the role of dislocations on the ionic conductivity has been started to be investigated [26-32]. For example improved conductivity and even superionic conductivity (~ 1 Ω^{1} cm^{-1}) have been observed in YSZ epitaxial single layers grown via pulsed laser deposition on MgO (1 1 0) and have been attributed to the high density of misfit dislocations, under the assumption that each dislocation line can act as a fast transport pathway [29]. However, lower beneficial effect has been reported on YSZ deformed single crystal [28, 30]. Dislocations can have the opposite effect and release the tensile strain deriving from the lattice mismatch, thus lowering its beneficial effect on the oxygen transport as it was observed upon the comparison of multilayers of YSZ/$Gd_2Zr_2O_7$ and GDC/ZrO_2 [21, 33].

The impact of misfit dislocations was studied also in textured thin films of $CeO_{0.9}Gd_{0.2}O_{2-\delta}$, which were deposited on Al_2O_3 and exposed to different heat-treatments. The decrease of the activation energy (from 0.86 eV to 0.74 eV) and the increase of the ionic conductivity upon annealing performed in different oxygen partial pressures was attributed to the decreased dislocation density upon exposure to the high temperature [31].

Recent theoretical and experimental works on $SrTiO_3$ seem to agree with this interpretation. Metlenko et al. [27] investigated by experimental and computational techniques the diffusion of oxygen ions along edge dislocations in $SrTiO_3$. From oxygen trace diffusion studies, the authors did not observe any fast diffusion along the dislocations and with theoretical simulation they confirmed that the oxygen vacancies were indeed attracted to the dislocation cores but that the oxygen transport mechanism was hindered leading to a higher activation energy. Similar outcomes on the segregation of rather immobile oxygen vacancies at the core of edge dislocations have been obtained by DFT calculations on CeO_2 [32] and $SrTiO_3$ [26]. In $SrTiO_3$ no evidence of fast pipe diffusion along the dislocations has been found while in CeO_2 hindering effect of the dislocations on oxygen vacancies migration has been predicted. In this case the strain effect in the proximity of the dislocation cores induces the segregation of dopants around the dislocations, leading to the formation of dopant enriched and depleted zones, which drive the redistribution of oxygen vacancies. The resulting vacancy-vacancy and vacancy-dopant interactions slow down the ionic conductivity.

In addition to structural features electrostatic effects (the occurrence of space charge regions) can deeply influence the local physicochemical properties of interfaces. In particular, such effects induce a local redistribution of the mobile charge carriers, which can lead to strong modifications of all properties that depend on the concentration of mobile charge carriers, e.g. electrical properties and charge storage capacity [15, 34, 35]. A number of relevant examples can be found in the literature, which are briefly discussed in the following.

When the interfaces are isolated or their range of influence is comparable with that of an isolated interface, this situation is described as a ‘trivial size effect’ [36]. A noteworthy example of trivial size effect is the interface between Al_2O_3 and AgCl. In AgCl the majority mobile charge carriers are silver ion vacancies, whose concentration is quite small, while their mobility is rather high. At the interface with Al_2O_3 the oxide adsorbs Ag^+ ions, leading to an increase of the Ag vacancies concentration in AgCl and thus to a larger ionic conductivity [36].

A different and more exciting situation occurs when interfaces perceive each other. This case is described as ‘true size effect’ [36]. A seminal work in this field [37] showed a strongly enhanced ionic conductivity measured parallel to the interfaces in CaF_2/BaF_2 multilayers with increasing interface density. In this case the overlapping of the space charge zones led to a significant improvement of the fluorine interstitial concentration in CaF_2 and fluorine vacancies in BaF_2 yielding to an enhancement of the parallel effective ionic conductivity by several orders of magnitude compared to the bulk [38]. This situation can be also interpreted as a transfer of fluorine ions from BaF_2 into the neighboring CaF_2 phase.

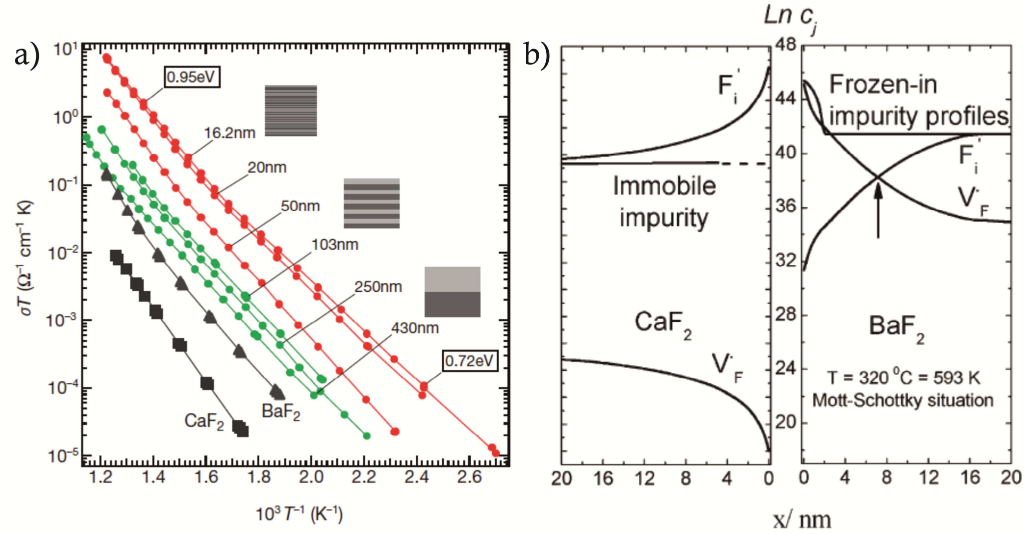

Figure 1 a) Ionic conductivity in CaF_2/BaF_2 heterostructures as a function of temperature plotted for different layer thicknesses (Reproduced from Ref. [38] with permission of Nature Publishing Group). b) Defect concentration profiles at 320°C at the interface between CaF_2 and BaF_2 films. (Reprinted from Ref. [37] with permission of John Wiley and Sons, Inc.)

Space charge zones can occur not only at interfaces in epitaxial thin films but in principle at all extended defects such as grain boundaries and dislocations as long as a local excess charge is present (e.g. in grain boundaries or dislocation cores). In this context, the role of dislocations in oxides has been barely touched upon. For example, it was shown that the presence of dislocations in TiO_2 (rutile) single crystals can modify the electrical transport properties by several orders of magnitude [39]. More recently, TEM investigations have shown that the interface between 8 mol% Y_2O_3-doped ZrO_2 single crystals and CeO_2 epitaxial films exhibited a regular pattern of misfit dislocation associated with a significant reduction of cerium [40].

The different effects showed above and the possible interaction between them make the study of interfaces in ionically conducting oxide materials particularly interesting. Moreover, a deeper understanding of these phenomena might disclose new opportunities for tuning of the electrical conduction properties through interface effects.

1.2 Motivation

Aim of this thesis is to investigate interface effects and the redistribution of the ionic charge carriers in epitaxial thin films and heterojunctions of selected oxide multilayered structures. For this purpose, different oxygen ions conducting materials are considered, namely $Y_2Zr_2O_7$ and 8 mol % Y_2O_3-doped ZrO_2 (8YSZ). In the appendix, also the less studied thin films of the oxygen interstitial conducting lanthanum silicate apatite are considered.

Ceramic pellets as well as polycrystalline and epitaxial films were investigated to assess the impact of grain boundaries on the oxygen ions transport.

For the characterization of strain effects on the ionic conductivity, the model system constituted by epitaxial multilayers of 8YSZ and $Y_2Zr_2O_7$ (lattice mismatch of 1.6 %) with variable thicknesses has been considered.

2 THEORETICAL BACKGROUND

2.1 Crystal structure of $Y_2Zr_2O_7$

The crystal structure of $Y_2Zr_2O_7$ (a defective fluorite) is face centered cubic and belongs to the space group *Fd-3m*, (lattice constant a=10.463 Å [41]). It is closely related to the pyrochlore crystal structure with the general formula $A_2B_2O_7$, in which all atoms occupy specific lattice positions. According to Wyckoff's notation, by fixing the origin on the B^{4+} cation, in pyrochlores the A cation occupy the *16d* site, the B cation the *16c* site, while two different kinds of oxygen are identified, namely O sitting on the *48f* position, which is involved in the oxygen migration, and O occupying the *8a* position, which is immobile. From this, it follows that the structural vacancy always sits on the *8b* position [42].

In the defective fluorite structure instead the positions of A^{3+} and B^{4+} are crystallographically equivalent, therefore the symmetry is higher and the structural vacancies can sit not only on the *8b* site but in every oxygen position [43, 44]. Therefore, defective fluorites can be treated as heavily A^{3+}- doped BO_2.

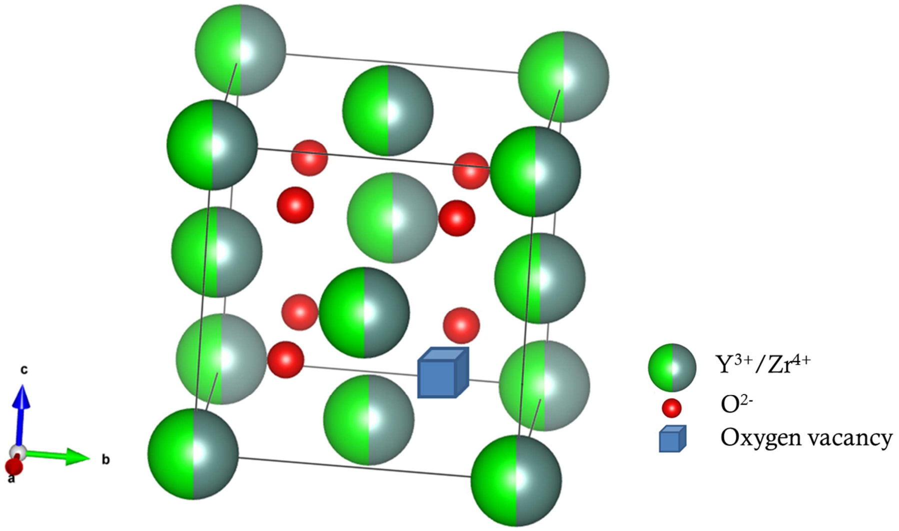

Figure 2: Crystal structure of $Y_2Zr_2O_7$. The cationic positions can be occupied by Y^{3+} or Zr^{4+} while one of the eight oxygen positions is occupied by an oxygen vacancy.

The ratio between the ionic radii of the cations $r(A^{3+})/r(B^{4+})$ is critical for determining which structure (pyrochlore or defective fluorite) is adopted by each composition. According to literature [45], a composition with a ratio lower than 1.26 tends to prefer a defective fluorite structure since the cations with similar ionic radii can easily exchange position, while for a ratio larger than 1.26, the pyrochlore structure is more favorable. For instance, among the zirconates, Yb^{3+} and Y^{3+} lead to a defective fluorite structure, while Sm^{3+} and Nd^{3+} yield a pyrochlore structure. For a ratio close to 1.26 ($Gd_2Zr_2O_7$) the final structure seems to depend on the heating treatment [46] (values are summarized in Table 1). The ordered structure offers a facilitated conduction pathway, which support the ionic conduction via oxygen vacancies. Therefore pyrochlores exhibit higher ionic conductivity and lower activation energy compared to the defective fluorite structure [42, 47-49].

Table 1: Ratio between the ionic radii of different cations and Zr^{4+}.

Cation	Yb^{3+}	Y^{3+}	Gd^{3+}	Sm^{3+}	Nd^{3+}
$r(A^{3+})/r(Zr^{4+})$	1.16	1.20	1.26	1.29	1.33

2.2 Crystal defects

Perfect crystals would be inert in terms of the transport of mass and charge. Ionic conductivity, electronic conductivity and diffusion depend on the deviation from perfect crystalline order or in other words the presence of defects. Crystal defects can be classified on the basis of their dimensions from zero-dimensional up to three-dimensional defects.

Zero-dimensional defects are point defects such as lattice vacancies and interstitial ions. A certain number of point defects are always present in a crystal (at temperatures > 0 K), because of the increased entropy, which lower the total free energy of the system [50]. In ionic solids the formation of pairs of opposite charge defects keeps the crystal electrostatically neutral.

One-dimensional defects can be considered as formed by displacements of parts of the crystal, as for example *edge* and *screw* dislocations. Two-dimensional defects are for example the boundaries between grains of the same composition but different orientations or interfaces between films and substrate [51]. Three-dimensional defects are e.g. pores and precipitates.

2.2.1 Point defect formation and association equilibrium

The electrical response of a material to temperature and atmosphere variations depends on the concentration of defect formation enthalpies, the presence of impurities or dopants and obviously the mobility of the charge carriers. Differently from pyrochlore structure, the defective fluorite compounds can be treated as heavily doped fluorites: in our case $Y_2Zr_2O_7$ can be considered a highly doped yttria stabilized zirconia with 50 % cationic doping [42, 52].

In the following, the derivation of the defect chemistry of $Y_2Zr_2O_7$ is described according to the Kröger-Vink notation [53]. For the derivation of a defect chemical model intrinsic, it is convenient to start by considering the Schottky and Frenkel disorder of zirconia and the corresponding mass action laws:

$$nil \rightleftarrows V_{Zr}^{////} + 2V_O^{\bullet\bullet} \qquad K_S = [V_{Zr}^{////}][V_O^{\bullet\bullet}]^2 = \exp\left(-\frac{\Delta G_S^0}{kT}\right), \tag{2.1}$$

$$Zr_{Zr}^{\times} \rightleftarrows Zr_i^{\bullet\bullet\bullet\bullet} + V_{Zr}^{////} \qquad K_F = [Zr_i^{\bullet\bullet\bullet\bullet}][V_{Zr}^{////}] = \exp\left(-\frac{\Delta G_F^0}{kT}\right). \tag{2.2}$$

Where K_S and K_F are the mass-action equilibrium constants for the Schottky and Frenkel reaction, respectively.

Other intrinsic defect reaction of importance is the electronic disorder reaction *(band-band transfer)*:

$$nil \rightleftarrows e^{/} + h^{\bullet} \qquad K_B = n \cdot p = \exp\left(-\frac{\Delta G_B^0}{kT}\right). \tag{2.3}$$

Where n is the electron and p the hole concentration and K_B the equilibrium constant of the electronic disorder.

Also the oxygen incorporation (excorporation) equilibrium in oxidizing (reducing) atmosphere are relevant for the formation of defects:

$$\frac{1}{2}O_{2(g)} + V_O^{\bullet\bullet} \rightleftharpoons O_O^{\times} + 2h^{\bullet} \qquad K_{ox} = \frac{p^2}{[V_O^{\bullet\bullet}] \cdot pO_2^{1/2}} = \exp\left(-\frac{\Delta G_{ox}^0}{kT}\right), \tag{2.4}$$

$$O_O^{\times} \rightleftharpoons V_O^{\bullet\bullet} + 2e' + \frac{1}{2}O_{2(g)} \qquad K_{red} = [V_O^{\bullet\bullet}] \cdot n^2 \cdot pO_2^{1/2} = K_{red}^0\left(-\frac{\Delta G_{red}^0}{kT}\right) \tag{2.5}$$

K_{ox} and K_{red} are the mass action equilibrium constant for the oxidation and reduction reaction.

However, due to the high yttrium content (note that yttrium substitutes zirconium and thus acts as an acceptor), the concentration of the oxygen vacancies, which are the majority mobile charge carriers of the system, is fixed by the yttrium concentration over a broad range of temperatures and oxygen partial pressures:

$$Y_2O_3 + 2Zr_{Zr}^{\times} + O_O^{\times} \rightarrow 2Y_{Zr}' + V_O^{\bullet\bullet} + 2ZrO_2 . \tag{2.6}$$

Strictly speaking as oxygen vacancies are present in high concentration, activities (a_j) have to be used in place of concentrations [54], as for example for Eq (2.4)

$$\overline{K}_{ox} = \frac{c_h^2}{a_{V_O^{\bullet\bullet}} \cdot pO_2^{1/2}} . \tag{2.7}$$

$\overline{K}$ is the true thermodynamic mass action constant, and contains the activity coefficient ($f_{V_O^{\bullet\bullet}}$): $\overline{K}_{ox} = K_{ox} f_{V_O^{\bullet\bullet}}$. As a consequence of the high concentration of oxygen vacancy, $f_{V_O^{\bullet\bullet}}$ is strongly influenced by their concentration and therefore by $\left[Y_{Zr}^{/}\right]$, but almost independent on the minor charge carriers concentration. It is worth noticing that $f_{V_O^{\bullet\bullet}}$ is temperature dependent, while its pO$_2$ dependence is negligible since $\left[V_O^{\bullet\bullet}\right]$ remains constant over a broad range of oxygen partial pressures.

A simplified yet reliable defect model can be obtained by neglecting defects with excessive enthalpy of formation. For example in the case of oxide with fluorite structure Schottky and Frenkel defects can be neglected due to their high enthalpy of formation.

From these considerations follows the simplified electroneutrality condition, which takes into account only the majority charged defect:

$$\left[Y'_{Zr}\right] = 2\left[V_O^{\bullet\bullet}\right] \tag{2.8}$$

This holds for a broad range of partial pressures and temperatures, in particular for those considered in this study.

At this high defect concentration association of defects can occur. If defects of opposite charge are very close together they can associate or form a cluster. This can be described for example as [51, 55]:

$$Y_{Zr}' + V_O^{\bullet\bullet} \rightleftharpoons \left(Y_{Zr}' - V_O^{\bullet\bullet}\right)^{\bullet} \qquad K_{ass} = \frac{\left[\left(Y_{Zr}' - V_O^{\bullet\bullet}\right)^{\bullet}\right]}{\left[Y_{Zr}'\right]\left[V_O^{\bullet\bullet}\right]} \tag{2.9}$$

Where K_{ass} is the corresponding mass-action equilibrium constant. This clearly shows that with increasing yttrium content in zirconia, defect association increases, which leads to an increase of the activation energy. Increased interactions finally lead to a reduction of the ionic conductivity [56, 57].

The concentration of oxygen vacancies $\left[V_O^{\bullet\bullet}\right]$ and their mobility u defines their conductivity as follow:

$$\sigma_{V_O^{\bullet\bullet}} = 2e\left[V_O^{\bullet\bullet}\right]u_{V_O^{\bullet\bullet}} \tag{2.10}$$

The total electrical conductivity of the material is given by the sum of the partial conductivity of the all mobile charged defects j in the material $\sigma = \sum_j \sigma_j$ [58].

2.2.2 Line defects

Dislocations are line defects created by tilting and rotating two parts of the crystal with respect to each other along a crystallographic plane. The boundary between the slip and unslipped part constitutes the dislocation line, if the dislocation line is perpendicular to the direction of slip a *edge* dislocation is formed, while if it is parallel it creates a *screw* dislocation. An *edge* dislocation can be thought also as an extra plane inserted into part of the regular crystalline lattice. More complex dislocation forms can be treated as being composed by *edge* and *screw* dislocations.

Line defects are not present in the thermodynamic equilibrium since their formation energy is too large compared to the change of entropy associated with their presence. Moreover, their concentration cannot be calculated according to the thermodynamics and strongly depends on the sample's history [51]. Characteristic of the dislocations is the Burgers vector $\vec{b}$ which defines a unit slip distance parallel to the direction of the slip. It is determined by carrying out a circuit count of atoms on lattice positions around the dislocation and comparing it with an analogous path in a perfect crystal: the difference defines the Burgers vector. For an *edge* dislocation Burgers vector and dislocation line are perpendicular, while for a *screw* dislocation they are parallel (Figure 3).

Obviously dislocations induce strain fields in their surrounding. The extent of the local strain depends on the dislocation type, the Burgers vector and the shear modulus of the material [50].

As explained above, the role of line defects on the ionic conduction is still controversial and subject of ongoing investigations. (see Paragraph 1.1).

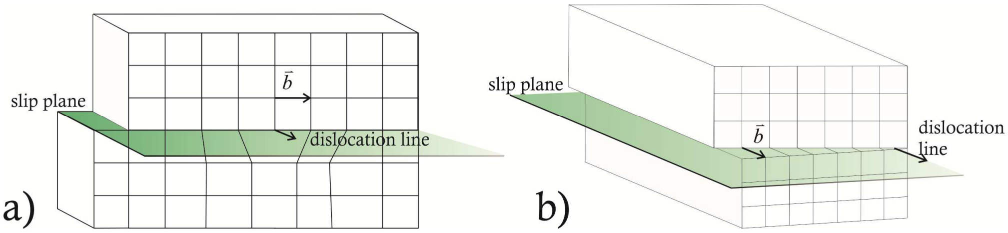

Figure 3: Schematic drawing of a) an *edge* dislocation and b) a *screw* dislocation showing the Burgers vector ($\vec{b}$), dislocation line and slip plane. In the *edge* dislocation burgers vector and dislocation line are perpendicular to each other, while in the *screw* dislocation they are parallely aligned.

2.2.3 Space charge model

As mentioned above (see paragraph 1.1), local excess charge at the grain boundaries, interfaces in thin films or dislocations induces a rearrangement of the mobile charge carriers leading to defect concentration distributions, which are very different from the bulk [59, 60].

In such situations, the concentration of the different chemical species can be determined starting from considering the equilibrium condition, at which the electrochemical potential of each mobile defect *j* must be constant in space (here the one-dimensional case is considered):

$$\tilde{\mu}_j(x_1) = \tilde{\mu}_j(x_2) \tag{2.11}$$

where x_1 and x_2 represent two different locations in the sample. Eq. (2.11) can be written in terms of chemical potential μ and electrostatic potential ϕ:

$$\tilde{\mu}_j(x) = \mu_j(x) + z_j e\phi(x) \tag{2.12}$$

Where z_j is the charge number of the charge carrier *j* and *e* is the electron charge.

For diluted concentrations of the species *j*, the chemical potential can be expressed as

$$\mu_j = \mu_j^0 + kT\,ln(c_j), \tag{2.13}$$

where μ_j^0 is the standard chemical potential. According to (2.11)

$$\mu_j^0 + kT\ln\left(c_j\left(x_1\right)\right) + z_j e\phi(x_1) = \mu_j^0 + kT\ln\left(c_j\left(x_2\right)\right) + z_j e\phi\left(x_2\right) \qquad (2.14)$$

results and from this

$$\left(\frac{c_j\left(x\right)}{c_{j\infty}}\right)^{1/z_j} = exp\left(-\frac{e}{kT}\Delta\phi\left(x\right)\right), \qquad (2.15)$$

from which one can recognize that the concentration profiles of the mobile charged defects are determined by the space charge potential $\Delta\phi(x)$, defined as the difference between the space charge potential $\phi(x)$ at the position x and in the bulk $\phi\left(\infty\right)$. For $x = 0$, $\phi(0) - \phi(\infty) = \Delta\phi_0$ and Eq.(2.15) becomes:

$$\left(\frac{c_j\left(0\right)}{c_{j\infty}}\right)^{1/z_j} = exp\left(-\frac{e}{kT}\Delta\phi_0\right) \qquad (2.16)$$

The determination of the charge carriers' concentration profiles requires the knowledge of the relationship between concentration and electrical potential, which is described by the Poisson equation

$$\frac{\partial^2\phi(x)}{\partial x^2} = -\frac{\rho(x)}{\varepsilon_0\varepsilon_r}, \qquad (2.17)$$

where $\rho(x)$ is the charge density.

The combination of Eq. (2.15) and Eq. (2.16) results in the Poisson-Boltzmann differential equation [3]:

$$\frac{\partial^2\phi\left(x\right)}{\partial x^2} = -\frac{\sum_j z_j e c_{j\infty}}{\varepsilon_0\varepsilon_r}\exp\left(-\frac{z_j e}{kT}\Delta\phi\left(x\right)\right) \qquad (2.18)$$

For the integration, it is helpful to distinguish two specific cases, the Gouy-Chapmann and the Mott-Schottky case, which are described in the following.

2.2.3.1 Gouy-Chapmann case

In this situation, all the charged defects are mobile (note that his holds for example in solids exposed at very high temperatures) and follow the space charge potential. Here, Eq (2.18) can be analytically solved only in the case of two charge carriers with opposite charge ($z_1 = -z_2 \equiv z$) and ($c_{1,\infty} = -c_{2,\infty}$). From this:

$$\phi(x) = \frac{2kT}{ze} \ln\left(\frac{1+\Theta \exp(-x/\lambda)}{1-\Theta \exp(-x/\lambda)} \right) \tag{2.19}$$

results, where

$$\Theta = \tanh\left(\frac{ze\Delta\phi}{4kT} \right) \tag{2.20}$$

and

$$\lambda = \sqrt{\frac{\varepsilon_r \varepsilon_0 kT}{2z^2 e^2 c_{j,\infty}}} \tag{2.21}$$

the Debye length.

The spatial variation of the potential defined in Eq. (2.18) is given by:

$$\frac{d^2\phi}{dx^2} = -\frac{zec_{j,\infty}}{\varepsilon_r \varepsilon_0} \exp\left(-\frac{ze}{kT}\phi \right). \tag{2.22}$$

The concentration profile is given by

$$\frac{c_j(x)}{c_{j\infty}} = \left(\frac{1+\Theta \exp(-x/\lambda)}{1-\Theta \exp(-x/\lambda)} \right)^{2z}. \tag{2.23}$$

The charge density Σ can be calculated as:

$$\Sigma = \sqrt{8kT\varepsilon_0 \varepsilon_r c_{maj,\infty}} \sinh\left(\frac{z_{maj} e\phi(0)}{2kT} \right), \tag{2.24}$$

where the subscript *maj* indicate the majority defect. In this case, the extent of the space charge layer is approximately equal to 2λ.

2.2.3.2 Mott-Schottky case

At lower temperatures the Gouy Chapmann case is no longer valid, since not all the charge carriers are mobile enough to redistribute within the SCL. This is also the situation of an oxide doped with an immobile aliovalent cation. In this case, the Mott-Schottky approximation describes the system better. For the solution of Eq. (2.18), the depleted charge carriers can be neglected and the charge density is fully defined by the dopant concentration (as long as dopant concentration exceeds the concentration of intrinsic defects). Therefore the Poisson-equation becomes:

$$\frac{\partial^2 \phi}{\partial x^2} = -\frac{z_{dop} e c_{dop,\infty}}{\varepsilon_0 \varepsilon_r}. \tag{2.25}$$

Considering a horizontal doping profile integrating Eq. (2.25) with the appropriate boundary conditions:

$$\begin{gathered} \phi'\left(\lambda^*\right) = 0 \\ \phi\left(\lambda^*\right) = \phi_\infty = 0 \end{gathered} \tag{2.26}$$

one obtaines:

$$\Delta\phi\left(x\right) = -\frac{z_{dop} e c_{dop,\infty}}{\varepsilon_0 \varepsilon_r}\left(x - \lambda^*\right)^2, \tag{2.27}$$

where

$$\lambda^* = \sqrt{\frac{2\varepsilon_0 \varepsilon_r \Delta\phi(0)}{z_{dop} e c_{dop,\infty}}} = \lambda\sqrt{\frac{4 z_{dop} e}{kT}\Delta\phi(0)}\,. \tag{2.28}$$

Since in a Mott-Schottky situation the majority of the defects cannot redistribute, the space charge width is dependent on the space charge potential and the charge screening ability is reduced. As a consequence λ^* is usually more extended than λ.

The concentration profiles in this case are given by

$$\frac{c_j\left(x\right)}{c_{j\infty}} = \exp\left(-z_j\left(\frac{x - \lambda^*}{2\lambda}\right)^2\right) \tag{2.29}$$

And the charge density given by

$$\Sigma = \sqrt{8\varepsilon_0 \varepsilon_r z_{dop} c_{dop,\infty} e \Delta\phi(0)} = 2\lambda^* e z_{dop} c_{dop,\infty} . \tag{2.30}$$

2.2.4 Conductivity of a single interface (trivial size effect)

Transport properties at the interfaces are generally different from the properties in the bulk, because they can be affected by distortions in the structure or by changes of the mobile charge carrier concentrations. Here we consider in brief the variation of ionic conductivity due to accumulation of oxygen vacancies, a detailed treatment is given elsewhere [59, 61].

The contribution to the ionic conductivity of a single interface can be simplified to pure parallel and series contributions.

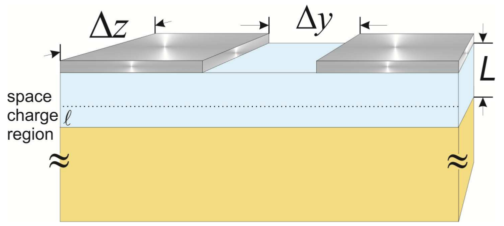

Figure 4: Schematic drawing of a bicrystal with its corresponding interfacial region.

Let us consider Figure 4 representing a single layer of size L, in which the extent of the space charge region is ℓ (note that $\ell = 2\lambda$ in the Gouy-Chapman case) so that $L >> \ell$ holds.

At the interface the conductivity can be highly anisotropic, and the conduction parallel and perpendicular to the interface can be measured separately. The sheet conductance [34] of the sample, $Y^{\parallel}$, free of unimportant geometric parameters parallel to the interface can be defined as

$$Y^{\parallel} = G^{\parallel} \frac{\Delta y}{\Delta z} = \sigma^{\parallel} L , \tag{2.31}$$

where Δz is the length of rectangular electrodes parallel to the interface and Δy the distance between them. $\sigma^{\parallel}$ is the conductivity measured parallely to the interface. This sheet conductance results from the integration of the conductivity on the thickness of the whole layer (*L*).

$$Y^{\parallel} = \int_0^L \sigma^{\parallel}(x)\,dx = Y^{\parallel}_{\infty} + \Delta Y^{\parallel}\,, \tag{2.32}$$

$\Delta Y^{\parallel}$ being the contribution of the space charge region and $Y^{\parallel}_{\infty}$ the bulk of the single crystal. If the the conductivityin the bulk and in the space charge layer, is governed by the same carrier j then

$$\sigma_j(x) = |z_j| e u_j c_j(x)\,. \tag{2.33}$$

From Eq. 2.32 and Eq. 2.33 it is possible to obtain the correlation between the sheet conductance and the concentration of charge carriers at the interface [61]. In a Gouy-Chapman case this results to be (under the assumption of a strong enrichment effect):

$$\Delta Y^{\parallel} = 2eu_j(2\lambda)\left(c_{j,\infty}c_{j,0}\right)^{1/2} \tag{2.34}$$

Experimentally, $\Delta Y^{\parallel}$ can be determined in the plot of the normalized conductance ($Y^{\parallel}$) versus the crystal thickness for $L = 0$. This is positive for an accumulation of positively charged mobile carriers and negative in the case of depletion. It is represented by the intercept on the *y* axis, corresponding to *L=0* [35, 62]. The slope resulting from the plot gives the bulk conductivity σ_{∞}.

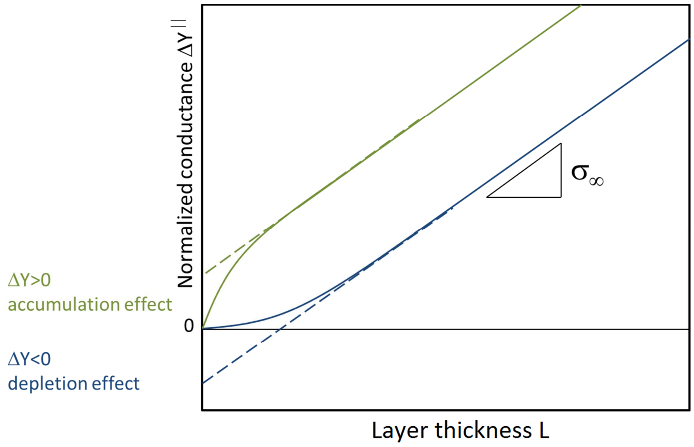

Figure 5: Normalized conductance as function of the layer thickness *L*.

2.3 Lattice mismatch and strain

Structural factors can also have significant effect on the ionic conductivity at the interface. At phase boundaries two lattices with different symmetry and different lattice constants are connected, leading to possible interfacial transition regions or local structures different from the bulk. This, together with line defects can affect the mobility and the concentration of the ionic charge carriers [17].

The main factors that determine the local structure at the interface is the lattice mismatch [63] and the thickness of the film:

$$f = \frac{a_{film} - a_{substrate}}{a_{substrate}} . \tag{2.35}$$

For a small mismatch the strain deriving from the difference of the lattice constants is completely compensated by local elastic strain. Only in this case the strain is equal to the misfit f [64].

For larger differences between the lattice parameter of the film and the one of the substrate the mismatch is generally too big to be accommodated only by elastic strain and it is instead partially (or in some cases fully) released by the formation of dislocations [18].

However one should note that in this context the thickness plays a crucial role: below a thickness of the film, defined *critical thickness*, t_{cr}, the mismatch is accommodated by elastic lattice strain, while when the thickness exceeds the critical thickness, the formation of misfit dislocations is energetically more favorable [63, 65].

Notably strain can alter the ionic transport through the variation of the charge carriers' migration energy. For thermodynamics reasons tensile strain is connected with a beneficial effect on the ionic conductivity and compressive strain with detrimental effect [17, 22, 64].

3 EXPERIMENTAL

3.1 Sample preparation

3.1.1 Powder preparation

The $Y_2Zr_2O_7$ powder was prepared starting from $ZrO(NO_3)_2$ hydrate (Sigma Aldrich 99.99 %) and $Y(NO_3)_3$ hydrate (Alpha Aesar 99.99 %). The reactants were dissolved in bi-distilled water and heated up to combustion after the addition of 5% v/v of glycerol. The resulting powder was then calcined in air at 800 °C for 5 hours.

3.1.1.1 Thermogravimetrical analysis (TGA)

Thermogravimetrical analysis was employed to calculate the amount of water in the reactants used for the powder synthesis. For this purpose, the reactants were heated in synthetic air (20 % O_2 + 80 % N_2) up to 800 °C with a heating rate of 5 °C/min. The technique was also used to determinate the suitable temperature of calcination in order to remove the organic part (glycerol used as fuel).

3.1.1.2 Inductive coupled plasma – optical emission spectroscopy (ICP-OES)

The chemical composition (to estimate the A-to-B cation ratio and determine the presence of impurities) was analyzed by inductively coupled plasma optical emission spectrometry (ICP-OES,Ciros Spectro Analytical Instruments GmbH) at the chemistry laboratory of the Max Planck Institute for Intelligent Systems, Stuttgart.

3.1.1.3 Sintering

The target for the pulsed laser deposition (18 mm diameter, 9 mm thickness) was pressed uniaxially (156 MPa) and sintered at 1700 °C for 10 hours in air. The targets were eventually polished in order to be installed into the PLD target holder of diameter 13.5 mm.

Pellets (10 mm diameter and thickness ranging from 4 up to 7 mm) were obtained by uniaxially pressing the powders at 450 MPa and sintered in air with different heating treatments. The density after sintering was estimated with the geometrical method. The porosity of the ceramic samples was measured by helium pycnometry (AccuPyc 1330, Micromeritics GmbH).

3.1.2 Thin film preparation: Pulsed laser deposition

Pulsed laser deposition is a physical evaporation technique which is used in particular for the fabrication of ceramic thin films.

As shown in Figure 6, a high power laser beam is focused on the target surface (consisting of a ceramic pellet of the same composition of the film that is going to be fabricated), which is positioned in a deposition chamber kept at low pressure (up to 0.5 mbar). The incident laser radiation is converted into thermal, chemical and kinetic energy, causing the consequent ablation of atoms and ions from the surface and the formation of the plasma (plum). The substrate, on top of which the film is grown, is situated (in setup used in this study) few centimeters below the target. The substrate can be heated (up to 800 °C) from the backside, in order to allow for a sufficient diffusion of the ions, which is required for the growth of crystalline films. Gases as N_2 or O_2 are introduced in the chamber during deposition of ceramic thin films in order to maintain the target and film stoichiometry.

During the growth many processes happen simultaneously on the substrate. Species ablated can bond to the substrate, associate in cluster, dissociate from the cluster or re-evaporate. The balance between growth and dissolution processes is governed by the free energy of the cluster and it defines the growth mechanism: (i) through three dimensional islands, (ii) formation of a full monolayer or (iii) growth of a full monolayer followed by nucleation of three dimensional islands.

The microstructure and the properties of the films can be affected by many factors. The power density of the laser can affect the retention of the target stoichiometry, while the laser frequency can strongly influence the microstructure and the roughness of the film. The substrate temperature instead affects the mobility of the species ablated and therefore the microstructure of the growing oxide. The oxygen partial pressure has an important effect on the control of oxygen stoichiometry in the film and also on the crystal structure, if this is strongly dependent on the oxygen content [66].

The most important parameters for the deposition of the films used in this study are summarized in Table 2. The deposition of the samples was always followed by an annealing at 1 bar at deposition temperature in order to compensate the oxygen content in the film.

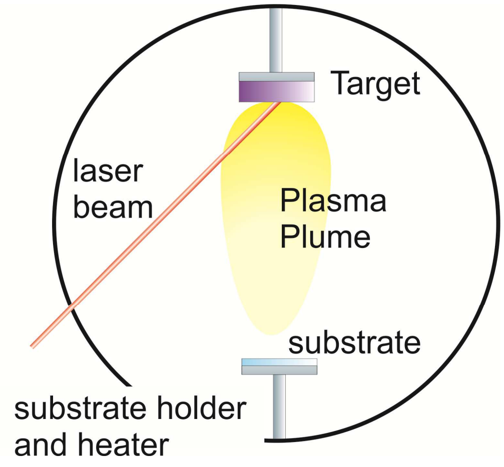

Figure 6: Schematic representation of the Pulsed laser deposition.

Table 2: Physical parameter used for the growing of the samples in the present work.

Parameter	**Value**
Substrate	MgO (1 1 0) MgO (1 0 0) Al_2O_3 (1 -1 0 2) Al_2O_3 (0 0 0 1)
Process gas	O_2
Evacuation pressure	$< 1x10^{-5}$
Heating rate	80 °C/min from room temperature to 110 °C less than the deposition temperature. 40 °C/min to the deposition temperature
Cooling rate	80 °C/min
Deposition	
Deposition pressure	0.001 mbar ÷ 0.5 mbar
Deposition temperature	660 °C ÷800 °C
Laser frequency	2 Hz ÷ 5 Hz
Energy density on the target	1.5 J/cm^2 ÷ 3 J/cm^2
Annealing	
Annealing pressure	1 bar
Annealing temperature	deposition temperature

An excimer laser with wavelength of 248 nm (Coherent GmbH, Germany) was employed. The temperature on the substrate was monitored using a pyrometer (Heimann optoelectronics model KT19.99).

The growing rate of different oxides has been determined on very thin test samples (5 nm - 20 nm) upon deposition by x-ray reflectivity (XRR) (see Figure 10).

3.2 Sample characterization

3.2.1 Characterization of electrical properties: Impedance spectroscopy

Impedance spectroscopy is a powerful technique that allows for the characterization of the complex impedance Z^* of a specimen as a function of frequency. As shown below, one of the great advantages of this method is the possibility of identifying the impedance contributions stemming from different loci of the sample (bulk, grain boundaries, interfaces etc.).

In practice, an alternating voltage, e.g. $U(t) = U_0 \cos(\omega t + \theta)$,where ω is the angular frequency and θ the phase shift, is applied to the sample over a broad frequency range, while the phase shift and amplitude of the resulting current $I(t) = I_0 \cos(\omega t)$ are measured [67]. From these, the impedance Z at each frequency can be determined. By taking into account the Euler's formula, the impedance Z^* can be also written as:

$$Z^* = \frac{U(t)}{I(t)} = \frac{U_0}{I_0} \exp(i\theta) = Z\left(\cos\theta + i\sin\theta\right) \tag{3.1}$$

Where $Z = \frac{U_0}{I_0}$. The resulting impedance in the frequency range considered is usually plotted as $-\mathrm{Z}'' = -\mathrm{Z}\sin\theta$ versus $\mathrm{Z}' = \mathrm{Z}\cos\theta$ (Nyquist plot).

The electrical behavior of a boundary free materials (single crystal) is properly described by an equivalent circuit consisting of a resistance in parallel with a capacitor (RC element). The impedance of this simple circuit corresponds to[51]:

$$Z = \frac{R}{1 + i\omega RC}\,. \tag{3.2}$$

For a purely capacitive behavior $Z^* = (i\omega C)^{-1}$, while for a pure resistive behavior $Z^* = R$ results.

Notably for all the frequencies the following relation:

$$\sqrt{(Z' - \frac{R}{2})^2 + (Z'')^2} = \frac{R}{2} \tag{3.3}$$

is fulfilled and thus the impedance spectra in a $iZ^{//}$ vs. $Z^{/}$ Nyquist plot is described by a semicircle with radius R/2 and displaced by R/2 from the origin.. At the maximum the relation $\tau = \omega^{-1} = RC$ holds, where τ is the relaxation time constant of the physicochemical process modeled by the RC element.

In the case of polycrystalline materials multiple contributions to the spectra (e.g. stemming from grain interior, bulk ,and from the grain boundaries) are expected, if the respective relaxation times are sufficiently different. In such situations, the equivalent circuit used to model the electrical behavior of the material consists of two (or more) RC elements in series. Note that for grain boundaries this applies for series contribution, while parallel contribution are included in the bulk semicircle. In practice, the recorded spectra consist of depressed semicircles owing to inhomogeneities in the samples. For this reason impedance spectra are fitted using a constant phase element (Q) in place of the ideal capacitor (C). The real capacitance can be calculated from the fitting parameters Q and α (which is related to the degree of depression of the semicircle and ranges typically between 0.7 and 1) as

$$C = (R^{1-\alpha}Q)^{1/\alpha} . \tag{3.4}$$

In addition to the impedance Nyquist plot ($Z^{/}$ vs. $jZ^{//}$) the data can be represented according to other complex functions as for example the dielectric modulus, ($\mathrm{M}^* = i\omega \mathrm{Z}^*$) which is extremely useful to separate different contribution (bulk, grain boundaries, electrodes) when they have very similar capacitances but different resistances [68, 69].

3.2.1.1 Grain boundaries and electrical conduction in polycrystalline materials: Brick layer model

The total resistivity of a polycrystalline material results from the contributions of the grains and the grain boundaries. These two contributions can be quantified by a.c. impedance spectroscopy, which allows for the determination not only of the corresponding resistance values but also of the associated capacitances. In order to extract from the experimental data the conductivity and dielectric constant values, one needs to take into consideration the geometry of the grains and the grain boundaries. This obviously challenging task is usually facilitated by the employment of the brick layer model [61, 70-72], according to which, the grains are assumed to be cube-shaped and homogeneous in size, with continuous connection of grain boundaries. This simplified description allows for the determination of the grain and grain boundaries conductivity of polycrystalline materials [73] and of the pathways followed by the mobile charge carriers [74]. For example, in the case of highly conductive grain boundaries, the electrical transport occurs along the grain boundaries, which are parallel to the direction of the current, while in the case of blocking grain boundaries the mobile charge carriers migrate in the grain and across the grain boundaries perpendicular to the direction of the current.

In the second case (which holds for the vast majority of ionically conducting oxides) the system can be described by two RC circuits in series, representing bulk and perpendicular grain boundaries, which in principle correspond in the impedance spectra to two distinct semicircles.

Resistance and capacitance obtained from the fit of the data allow for the calculation of bulk and grain boundaries conductivities (σ_{bulk}, σ_{gb}) and dielectrical constant (ε_{bulk}) by considering the sample's geometry as:

$$\sigma_{bulk} = \left(\frac{1}{R_{bulk}}\right)\left(\frac{L}{A}\right) \tag{3.5}$$

and

$$\sigma_{gb} = \left(\frac{1}{R_{gb}}\right)\left(\frac{L}{A}\right), \tag{3.6}$$

$$\varepsilon_{bulk} = \frac{C_{bulk}}{\varepsilon_0}\frac{L}{A} \tag{3.7}$$

Where A is the cross section area of the sample, L the distance between the electrodes, R_{bulk}, R_{gb}, C_{bulk} and C_{gb} the bulk and grain boundaries resistance and capacitance respectively.

It is important to note that σ_{gb} as it is defined in Eq. 3.6 represents a measured conductivity that does not take into account the grain boundary geometry. For this reason, it is more appropriate to consider the local specific grain boundary conductivity $\sigma_{gb,spec}$, which under the assumption that $\varepsilon_{bulk} \approx \varepsilon_{GB}$, can be written as [75]:

$$\sigma_{gb,spec} = \sigma_{bulk} \frac{C_{bulk} R_{bulk}}{C_{gb} R_{gb}} . \tag{3.8}$$

From the dependence of the conductivity on the temperature, it is possible to determine its activation energy (E_a): since from the Nernst – Einstein equation the conductivity can be written as

$$\sigma = \frac{A}{T} \exp\left(-\frac{E_a}{kT} \right), \tag{3.9}$$

where A is a temperature independent factor, writing the equation as

$$\ln(\sigma T) = \ln(A) - \frac{E_a}{kT} \tag{3.10}$$

it is clear that if $\ln(\sigma T)$ is plotted as a function of $1/T$ (Arrehnius plot), the resulting slope corresponds to $-\frac{E_a}{k}$.

3.2.1.2 Equivalent circuits and separation of the impedance contributions

A typical impedance spectrum recorded during this work is shown in Figure 7. Usually, all the measured samples showed only one semicircle in the Niquyst plot and the contribution of the electrodes at low frequency.

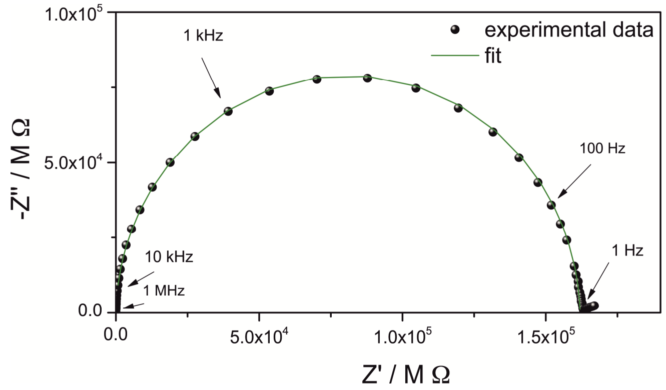

Figure 7 Impedance spectrum and corresponding fitting line of an epitaxial thin film of $Y_2Zr_2O_7$ with a thickness of 100 nm. At frequencies below 1 Hz is clearly visible the contribution of the electrode.

As stated above, for a polycrystalline material an equivalent circuit consisting of three contributions should be taken into account (Figure 8), which correspond to bulk

($R_{bulk}C_{bulk}$), grain boundaries ($R_{gb}^{\perp}C_{gb}^{\perp}$) and the electrode ($R_{el}C_{el}$). In addition to these, for a thin film, we also have to consider the contribution of the substrate ($R_{substrate}C_{substrate}$) and the one deriving from the measurement cell such as wires and sample holder connected in parallel with the sample ($R_{wiring}C_{wiring}$), both can be described by a RC circuit in parallel with the film.

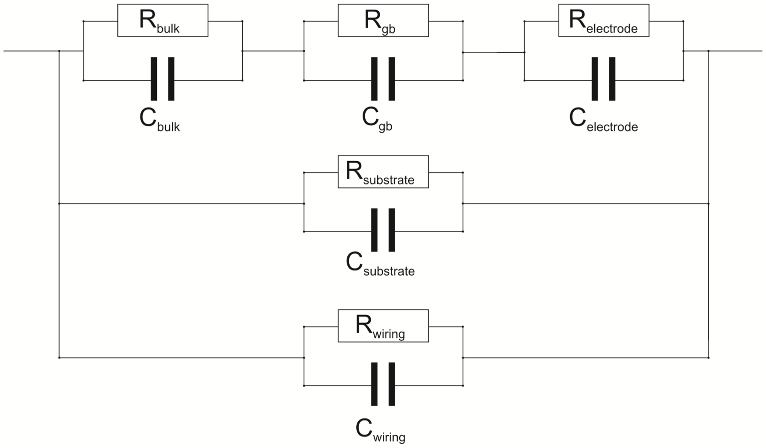

Figure 8: General equivalent circuit for thin films

The resistance contribution of substrate and measurement cell are carefully avoided by choosing a poorly conducting substrate and calculating the optimal film thickness in order to obtain a film conductance, which is at least one order of magnitude higher than the conductance of the substrate.

The electrode contribution thanks to its high capacitance (10^{-9} F) is visible at low frequency, and can be separated from the others contributions.

The capacitive displacement current through the substrate and the capacitance between the contacting wires ($C_{substrate}$, C_{wiring}) instead cannot be easily minimized. This results in the stray capacitance [76]:

$$C_{stray} = C_{substrate} + C_{wiring} \, . \tag{3.11}$$

It is strongly dependent on the electrode geometry and the distance between electrodes. While the capacitance of the substrate can be estimated by knowing the substrate material and electrode geometry, the capacitance deriving from the contacting wires is more difficult to estimate. For our measurement cell the total stray capacitance has been measured to be about 10^{-12} F.

Due to the extremely small thickness of the samples its capacitance is orders of magnitude lower than the stray capacitance and therefore the contribution of the bulk (calculated to be on the order of 10^{-16} F for a 100 nm thick film of $Y_2Zr_2O_7$) and the grain boundaries (10^{-14} F if the average grain size is 60 nm), that otherwise would be distinguishable are convoluted in only one semicircle with resistance equal to the total resistance and capacitance corresponding to C_{stray} . This means that the resistance of the grain boundaries cannot be extracted from the experimental data. Rather, it can be estimated by comparing the electrical behavior of epitaxial and polycrystalline films.

Taking into account the considerations made above, a simplified equivalent circuit can be used to fit the impedance spectra, including only the total resistance and a constant phase element (Q) in place of a capacitance, to better fit the real behavior of the sample.

3.2.1.3 Experimental set up and measurement cell

For the impedance measurements a Novocontrol Alpha-A High Performance Frequency Analyzer (Novocontrol GmbH) was used. The samples were measured between 0.2 Hz and 2 MHz, with 2 s of integration time, output voltage of 0.1 V and 0.5 s of delay time, recording 20 data point per decade. The impedance spectra were fitted with the software *ZView 2* (Scribner Associated Inc) software.

For the measurements, two in-plane electrodes , (4.5 mm x 10 mm and thickness 400 nm, each), with distance 1 mm from each otherwere sputtered onto the film surface using a Edwards Auto 306 Turbo sputtering system.

For multilayer systems samples after deposition were etched on the lateral side down to the substrate, and then Pt electrodes were sputtered on the etched part. Sample were etched by Ar ion milling with a Roth and Rau Unilab etching machine and Pt electrode (4.5 x 4.5 mm^2) were sputtered with an in-house developed sputtering machine

A cell holding 4 samples simultaneously has been used for the conductivity measurements, in order to expose the samples to the exact same conditions of temperature and pO_2, and have therefore a better comparability of the results.

The resistance of the measurement cell was increased thanks to the employment of sapphire, a very resistive oxide and the special shape of the sample holder (Figure 9) which was designed to maximize the conduction pathway [77].

Figure 9: Sapphire sample holder specifically designed to reduce the spurious contribution to the impedance spectroscopy measurement.

Typically, the samples were equilibrated in oxygen for hours (up to 40 hours) until the impedance spectra became stable (the spectra overlapped), which indicated the specimens to have reached the equilibrium with temperature and surrounding gas. The activation energy was measured by cooling the sample with steps of 30 degrees (with 3 hours for equilibration at each step) or 10 degrees with 1 hour equilibration.

The dependence on the oxygen partial pressure was determined between 1 bar and 10^{-5} bar using different mixtures of O_2 and N_2. The actual value of the oxygen partial pressure was monitored with a Cambridge Sensotech Rapidox 2100 oxygen sensor. During the pO_2 - dependence measurements at high temperature, the changes of oxygen partial pressure have been alternated between lower and higher pressure, in order to minimize the contribution of a possible dewetting of the platinum electrodes to the resistance changes [78, 79].

3.2.2 Microstructure characterization

3.2.2.1 Atomic Force Microscopy

Atomic force microscopy (AFM) scans have been acquired with a Digital Instrument Multimode scanning probe microscope, for determining the roughness of substrates and films. In general, the technique relies on the force experienced by a probe (a sharp tip sticking out from the bottom side of a cantilever) while it approaches a surface. During the topography acquisition the interaction between the tip and the surface let deflect the cantilever. Such deflections are measured optically by using a laser beam, which is reflected into a detector by the back side of the cantilever. An AFM can be operated in three modes: contact, non-contact and tapping mode [80]. The contact mode is based on the van der Walls attractive forces between tip and surface and provides the highest resolution. In the non-contacting mode, the tip scans the surface at constant distance. In addition to this the tapping mode create an intermittent contact with the surface, improving the resolution with respect to the non-contact mode, but avoiding to damage the surface as it happens in the contact mode [81]. The images presented in this thesis have been acquired in tapping mode.

The roughness of the samples investigated by AFM is expressed here in terms of root mean square i.e. the mean squared absolute values of the surface roughness profile and is expressed as [80]:

$$RMS = \sqrt{\frac{1}{l}\int_0^l \left|z^2(x)\right| dx} \tag{3.12}$$

Where $z(x)$ is the function that describes the surface profile analyzed in terms of height (z) as a function of the position x of a sample evaluated over the length l. The quantity RMS is more sensitive to peaks and valleys than the average roughness due to the squaring of the amplitude [82].

3.2.2.2 X ray diffraction

X-ray diffraction (XRD) was employed on powders, pellets and thin films, in order to check the presence of secondary phases and the orientation and texture of the thin films.

For the diffraction on pellets and powders a X'pert, Philips, 3710, HTKK, Cu K_α=1.5405 Å) was used, θ/2θ were recorded between 10°-90° with steps of 0.001° or 0.002°. For the thin films a Bruker D8 Diffractometer (Cu-K_α 1.5418 Å) was employed, θ/2θ were recorded between 15° - 85° with steps between of 0.01 ° or 0.02 ° and acquisition time between 1 and 6 sec for each step.

3.2.2.3 Pole figures

The texture of the thin films was investigated using XRD pole figures analysis performed with a Philips X'Pert XRD – Co-K_α = 1.78897 Å. The φ and ψ scans were recorded for 2 defined 2θ angles, namely at 40.50° and 69.0°. Pole figures were acquired in the χ angle range 0 – 90 ° and the φ angle range 0 – 360 ° with χ and φ steps of 2 °.

The software Carine 3.1 was employed to predict the position (φ and ψ degree) of the peaks of the selected plane and to compare the outcome of the simulation with the experimental results.

3.2.2.4 X-ray reflectivity (XRR)

X-ray reflectivity (Bruker D8 Diffractometer, Cu-K_α 1.5418 Å) was used to measure the thickness of selected thin films. Measurements were performed at values of 2θ between 0.5° and 4° with steps of 0.001° or 0.005° and acquisition time of 5÷10 sec for each step.

X-ray reflectivity is a grazing incidence x-ray diffraction technique using a small incident angle. The small path covered by the X-rays in the sample gives important structural information deriving almost entirely from the film, thus ruling out the influence of the substrate. Reflectivity measurements are possible owing to the different electronic density of two layers lying on the top of each other, which result in different refractive indexes. Therefore, the radiation is scattered with different angles, which leads to constructive or destructive interference. These correspond to the points of maxima and minima of the fringes in the diffraction pattern (Kiessing fringes), whose positions are inversely proportional to the layer thickness d ($d=\lambda_{Cu\text{-}K\alpha}/2\cdot\Delta\alpha$, where $\Delta\alpha$ is the angular position difference of two consecutive maxima or minima – see Figure 10). More sophisticated approaches, based on the crystal structure and density, can provide more accurate estimations of the thickness and even the inter-layer roughness. In the present work layers thickness have been calculated from the angular position of the peaks' minima.

XRR has been also used to estimate the film growing rates. Since the technique is not very accurate for thicknesses above 50 nm, very thin films (5 nm – 20 nm) were employed for this purpose.

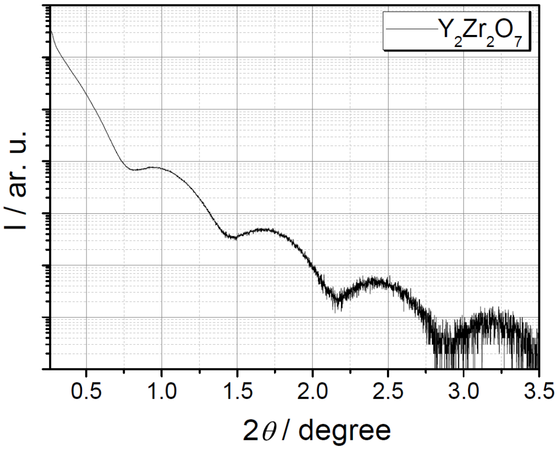

Figure 10: X - Reflectivity diffraction pattern of a $Y_2Zr_2O_7$ thin film deposited on MgO (1 1 0), 10 nm thick. The thickness has been calculated from the distance between the fringe minimum.

3.2.2.5 Transmission Electron Microscopy

Transmission electron microscopy (TEM) analysis was performed in order to investigate the microstructure of cross-sections of the films. Analyses were performed at the Stuttgart Center for Electron Microscopy.

The TEM specimens were prepared by focused ion beam technique using Zeiss Merlin crossbeam 1540 ESB scanning electron microscope (SEM). The transmission electron micrographs were acquired using a JEOL ARM 200CF Microscope equipped with a cold field emission electron source, a probe corrector, and a Gatan GIF quantum ERS spectrometer. The microscope was operated at 200 kV, with a semi-convergence angle of 28 mrad, which gives rise to a probe size of 0.8 Å. Collection angles of 90 – 370 mrad were used to obtain the high angle dark field (HAADF) images. In the EDS measurements, Y - K and Zr - K lines were used for the quantification.

4 RESULTS AND DISCUSSION

4.1 Grain boundary contribution in textured thin films and pellets

4.1.1 Pellets and targets characterization

$Y_2Zr_2O_7$ oxide powders were prepared starting from $ZrO(NO_3)_2$ hydrate (Sigma Aldrich 99.99 %) and $Y(NO_3)_3$ hydrate (Alpha Aesar 99.99 %), from which pellets and targets were obtained, as it was previously described in section 3.1.1.

ICP - OES analysis was employed to detect the concentration of the impurities in the samples. From the negligible amount of cationic impurity detected in the powders (the results are reported in Table 3), it is possible to conclude that the only significant doping effects derives from the yttrium content.

ICP - OES analysis was also employed to determine the deviation from the nominal Y^{3+}/Zr^{4+} ratio in the samples investigated. The actual stoichiometry has been calculated as: $Y_{1.94}Zr_2O_{7-x}$ for the target used for the deposition of thin films and $Y_{2.20}Zr_2O_{7+x}$ for the pellet.

Table 3: Chemical analysis by ICP - OES of the most abundant cations in the $Y_2Zr_2O_7$ powders

Element	**wt %**		
	Target	**Microcrystalline pellet**	**Theoretical**
Y	35.5 ± 0.4	39.00 ± 0.05	37.65
Zr	37.7 ± 0.5	36.18 ± 0.05	38.63
Fe	<0.005		
Ba	<0.005		
Al	<0.005		
Ca	<0.01		
Cr	<0.005		
Mg	<0.001		
Mn	<0.001		

Both powders upon calcination and pellet upon sintering have been characterized by X-ray diffraction (Figure 11) confirming the formation of $Y_2Zr_2O_7$ defective fluorite phase, and no formation of second crystalline phases. The resulting X-ray diffraction patterns were compared with pattern reported in Ref [83] and [84].

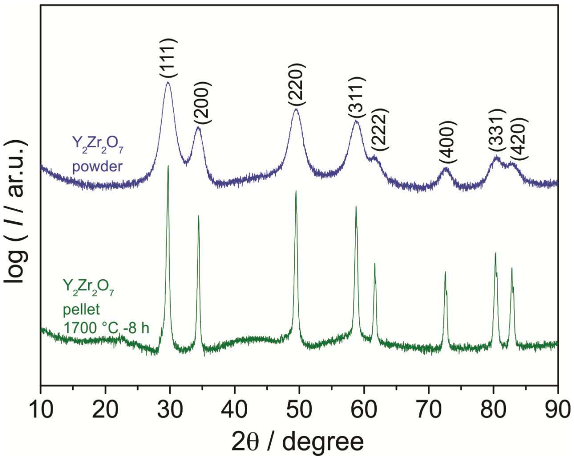

Figure 11: XRD pattern of the $Y_2Zr_2O_7$ powder calcined at 800 °C for 8 hours (blue) and of the pellet sintered at 1700 °C for 8 hours (green).

The density of the pellets after sintering estimated by the geometrical method was 4.00 g cm^{-3}, corresponding to a relative density of 73.2 %. The average grain size, estimated from SEM analysis was approximately 1 μm.

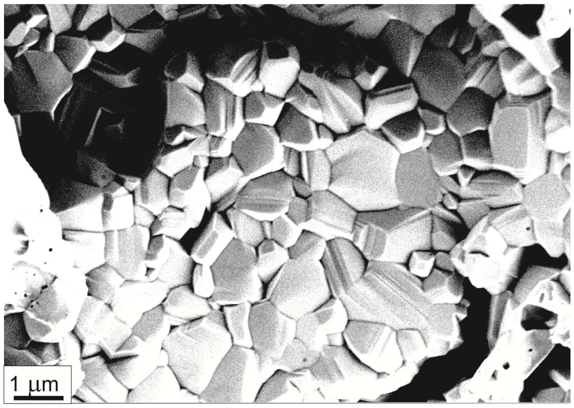

Figure 12: SEM micrograph of the cross-section of a microcrystalline sample upon sintering at 1700 °C for 8 hours.

4.1.2 Thin films microstructure characterization

Thin films with a thickness of 100 nm have been deposited on various substrates, namely Al_2O_3 (0 0 0 1), Al_2O_3 (1 -1 0 2), and MgO (1 1 0).

The XRD patterns of the films grown on Al_2O_3 (0 0 0 1) and Al_2O_3 (1 -1 0 2) show strong peaks corresponding to the (1 1 1) and (2 2 2) reflections. Some of these samples present also a second weak peak corresponding to the (2 0 0) direction (Figure 13a-b). These features clearly indicate the films deposited on the alumina substrates to be strongly textured. A further characterization was carried out by analyzing the {0 0 1} pole figures acquired at $2\theta_{Co-K_\alpha} = 40.5°$ of a 100 nm thick film grown on Al_2O_3 (0 0 0 1) (Figure 14a). The three broad peaks at $\psi = 54$ ° indicate a certain misalignment from epitaxial growth in the in-plane direction. The peaks are repeated every 120 ° along φ according to the threefold symmetry of the (1 1 1) plane. The intensity at $\psi = 38$ ° instead does not originate from the $Y_2Zr_2O_7$ phase but from to the (1 0 4) plane of the substrate ($2\theta_{Co-K_\alpha} = 41.09°$).

On the contrary, $Y_2Zr_2O_7$ thin films on MgO (1 1 0) show sharp XRD peaks corresponding to reflections of the (2 2 0) direction (Figure 13c), i.e. the {1 1 0} orientation prevails. In the {0 0 1} pole figure, the two peaks at $\psi = 45$ ° confirm the epitaxial growth of $Y_2Zr_2O_7$ (Figure 14b). The out of plane lattice constants calculated from the XRD data indicate a lattice expansion from the epitaxial to the textured thin films: 5.23 Å on MgO (1 1 0), 5.25 Å on Al_2O_3 (0 0 0 1), 5.26 Å on Al_2O_3 (1 -1 0 2), and can be considered to be in agreement with theoretical values reported in literature that vary from 5.20 Å [85] to 5.23 Å [41].

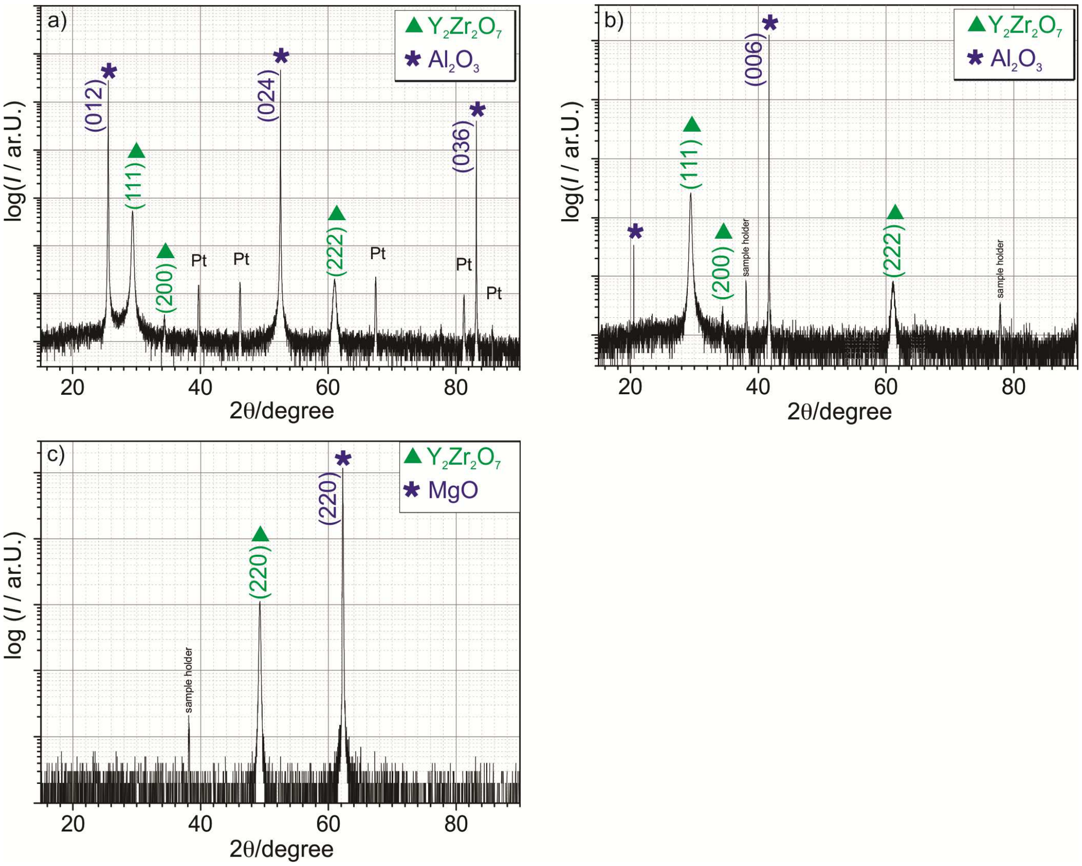

Figure 13: XRD patterns of $Y_2Zr_2O_7$ thin films. a) on Al_2O_3 (1 -1 0 2), b) on Al_2O_3 (0 0 0 1), in which two orientations are visible. c) on MgO (1 1 0) oriented on (2 2 0) direction only one orientation can be observed.

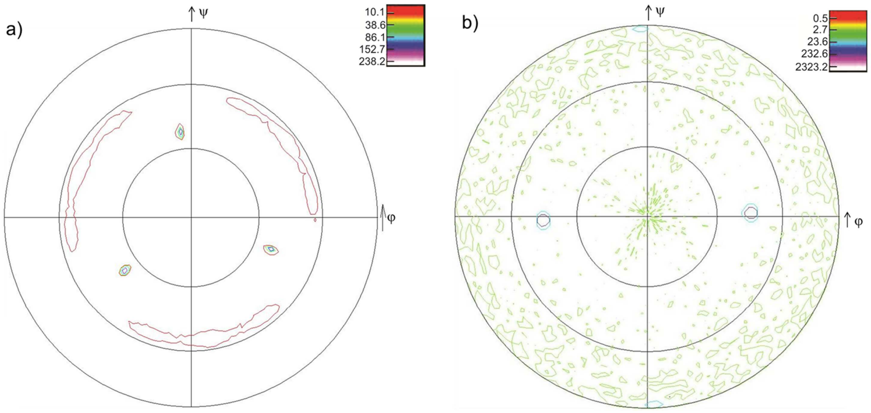

Figure 14: {001} Pole figure ($2\theta_{Co-K_\alpha} = 40.5°$) of a) a textured thin film grown on Al_2O_3 (0 0 0 1): the distributed intensity along φ indicates the partially textured microstructure of the sample. b) Epitaxial thin film on MgO (1 1 0).

AFM analysis of the film surfaces allowed for the determination a very low surface roughness (comparable to the size of a unit cell) for both the textured and the epitaxial samples (see also Figure 15): the root mean square (RMS) values obtained from films grown on different samples are summarized in Table 4.

Table 4: Root mean square (RMS) values of $Y_2Zr_2O_7$ thin films grown on different substrates.

Substrate	**RMS / Å**
Al_2O_3 (1 -1 0 2)	4.65
Al_2O_3 (0 0 0 1)	5.21
MgO (1 1 0)	5.15

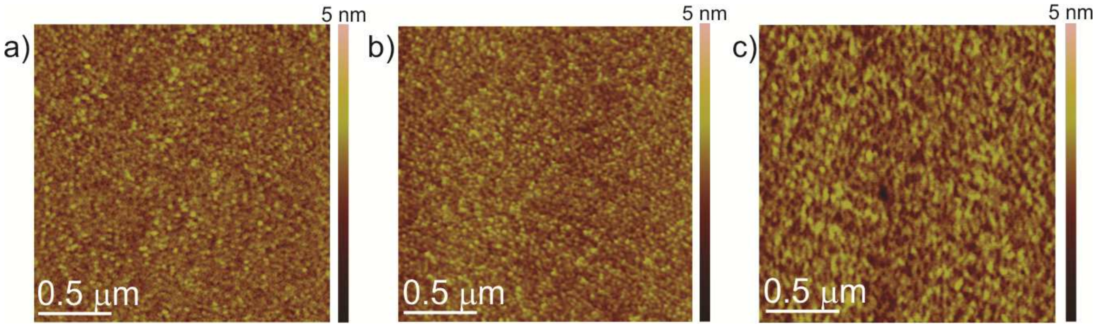

Figure 15: AFM images of $Y_2Zr_2O_7$ 100 nm thin films a) on Al_2O_3 (1 -1 0 2), RMS 0.465 nm; b) on Al_2O_3 (0 0 0 1), RMS 0.521 nm; c) on MgO (1 1 0), RMS 0.515 nm.

4.1.3 Conductivity data

In order to characterize the electrical properties of bulk and grain boundaries, textured single layers as well as a microcrystalline pellet have been analyzed via electrochemical impedance spectroscopy.

Figure 16a shows a characteristic impedance spectrum of the microcrystalline pellet acquired at 700 °C in pure oxygen. To the high frequency arc, which was fitted using the equivalent circuit shown in the inset, corresponds a capacitance of 8.4 10^{-12} F and a resulting relative permittivity of 30. This allows one to assign the contribution to the bulk properties of the material. The low frequency contribution having a capacitance of 5.5 10^{-5} F can be safely assigned to the electrode contribution. Notably, no contribution stemming from the grain boundaries could be detected neither at lower temperature (Figure 16b).

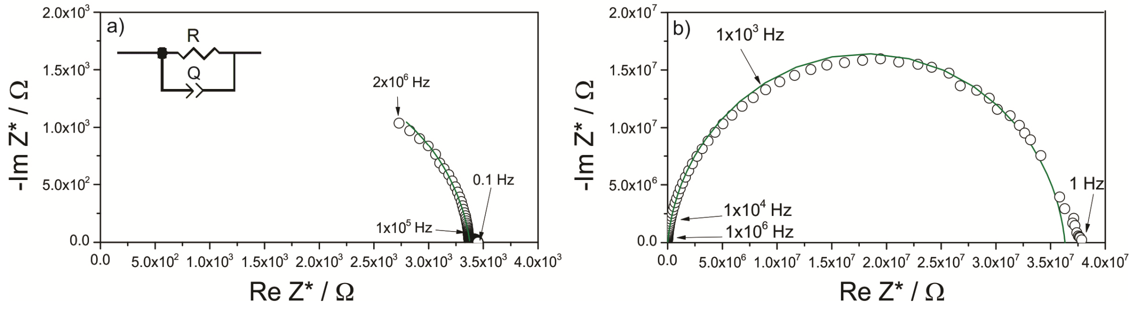

Figure 16: Impedance Nyquist plot of a microcrystalline pellet acquired in oxygen. a) at 700 °C b) at 350 °C. In the inset of fig. a the equivalent circuit used to fit the spectra is shown.

Before analyzing in detail the electrical properties of pellet and thin films it is important to notice that both do not show any perceptible dependence of the conductivity on the oxygen partial pressure, indicating an ionic type of conductivity (Figure 17 a,b), dominated by oxygen vacancies $V_O^{\bullet\bullet}$, as expected from the defect model described in Paragraph 2.2.1, and as experimentally observed on similar zirconates with pyrochlore structures [86].

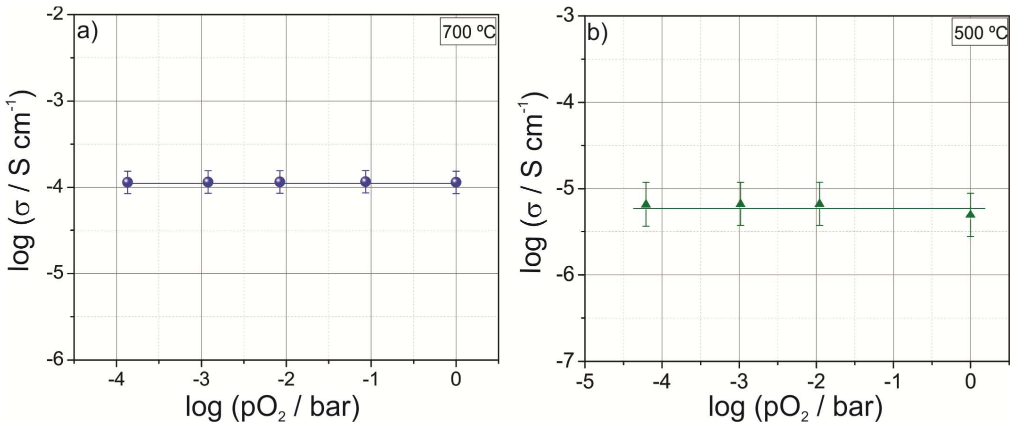

Figure 17: Oxygen partial pressure dependence of a) microcrystalline pellet at 700 °C and b) epitaxial thin film at 500 °C. The lines are a guide to the eye.

Figure 18a shows the conductivity as a function of the temperature of a microcrystalline pellet and an epitaxial thin film. These data have been extracted from the impedance spectra as explained in Chapter 3.2.1.1.

As expected, for structural reasons, in these samples the activation energy is higher than in the pyrochlore structures. In contrast to what happens in pyrochlores, in defective fluorites vacant oxygen sites are randomly distributed, and there are no preferential pathways for the oxygen migration that would lower the total energy required for the ionic transport [47].

It is noteworthy that the conductivity values of these two samples differ only by half an order of magnitude and the activation energies vary from 1.44 eV for the epitaxial thin film to 1.52 eV for the pellet. This suggests the grain boundaries to hinder only very marginally the oxygen ion migration.

It is interesting to compare these results with those reported in Figure 18b, where the temperature dependence of the conductivity of textured and epitaxial films is shown. Also in this case, the difference in conductivity (which is expected owing to the different microstructure epitaxial vs. textured films) is very small (at 700 °C 4.0 10^{-4} S cm^{-1} for the epitaxial film, 2.4 10^{-4} S cm^{-1} and 2.6 10^{-4} S cm^{-1} for the textured thin films grown on Al_2O_3 (0 0 0 1) and on Al_2O_3 (1 -1 0 2), respectively), particularly if compared to similar systems, e.g. YSZ thin films, available in the literature. For example, Peters et al. [12] observed variation of one order of magnitude in the conductivity of $Y_{0.17}Zr_{0.83}O_{1.91}$ thin films (from 10^{-5} S/cm to 10^{-4} S/cm at 400 °C) by varying the grain size from about 20 nm to 150 nm in layers deposited by sol-gel method having a thickness of 400 nm. Similarly, Schlupp et al. [87] measured a conductivity decrease of more than 1 order of magnitude (from 6.6 10^{-4} S cm^{-1} to 3 10^{-5} S cm^{-1} at 500 °C), together with an increase of activation energy of 0.3 eV when going from columnar grown (with a lateral size of about 10 - 20 nm) to nanocrystalline thin films (average grain size <8 nm) of 8YSZ deposited via chemical vapor deposition. These results allow one to conclude that compared to related systems (YSZ), the grain boundaries in $Y_2Zr_2O_7$ have a really minor blocking effect on the ionic conductivity.

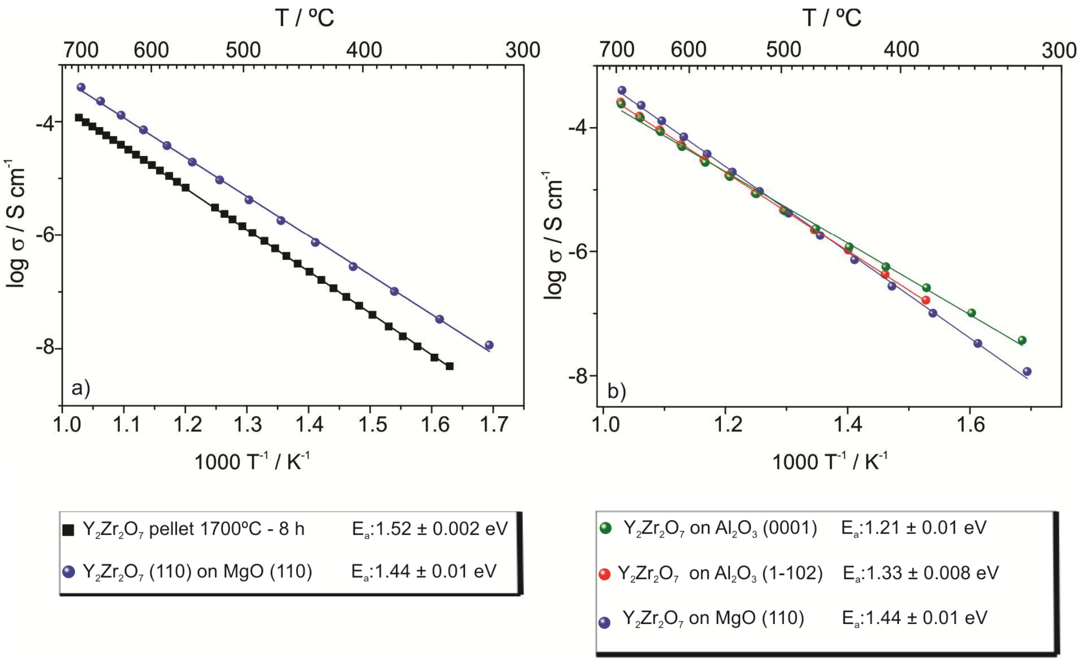

Figure 18: Arrhenius plots of a) a microcrystalline pellet and an epitaxial thin film deposited on MgO (1 1 0), b) An epitaxial thin film deposited on MgO (1 1 0) and textured thin films grown on Al_2O_3 (0 0 0 1) and (1 -1 0 2). All the films had a thickness of 100 nm.

Table 5: Conductivities and activation energies of $Y_2Zr_2O_7$ thin films deposited on different substrates as well as of a microcrystalline pellet.

Sample	Activation Energy / eV	σ at 700 °C / S cm^{-1}
Epitaxial film on MgO (1 1 0)	1.44 ± 0.01	4.0 10^{-4}
Textured film on Al_2O_3 (1 -1 0 2)	1.33 ± 0.008	2.6 10^{-4}
Textured film on Al_2O_3 (0 0 0 1)	1.21 ± 0.01	2.4 10^{-4}
Microcrystalline pellet	1.52 ± 0.002	1.2 10^{-4}

Interestingly, the activation energy of the textured films (on Al_2O_3 substrates) is lower than the one of the epitaxial sample, although the conductivities are rather similar and certainly lie within the experimental uncertainty. Further research is needed to investigate this aspect more in detail, since for blocking behavior of the grain boundaries in textured films (even if not significant as in this case) the opposite trend would be expected. Strain effects, which are known to alter the ionic conduction, can be ruled out due to the relatively high thickness of the sample, which allows for a full relaxation of the strain. Moreover, lattice values calculated from XRD (Paragraph 4.1.2) do not indicate a variation of the lattice parameters consistent with the trend of activation energies; thin film on Al_2O_3 (0 0 0 1) have an intermediate lattice value (5.25 Å) compared to the films grown on Al_2O_3 (1 -1 0 2) and MgO (1 1 0) but the lowest activation energy.

4.1.4 Section conclusions

In this section, the characterization of microstructure as well as the electrical properties of microcrystalline pellets and thin films of $Y_2Zr_2O_7$ have been described.

The microstructure of the thin films (deposited via pulsed laser deposition) was investigated with different techniques (XRD, pole figures, TEM, AFM) and confirmed the epitaxial growth of the films grown on MgO (1 1 0) and the textured character of the layers on Al_2O_3 (0 0 0 1) and (1 -1 0 2).

The comparison between the conductivities of pellets, and epitaxial thin films pointed towards a minor effect of the grain boundaries on the electrical properties of $Y_2Zr_2O_7$, which seem to affect the conductivity in the investigated samples only very marginally. All specimens show no dependence on the pO_2 and hence a predominantly ionic conductivity at the temperature and oxygen partial pressure range considered here.

4.2 Interface effect in epitaxial thin films

As pointed out from the X-ray diffraction patterns and pole figures shown in Paragraph 4.1.2, thin films of $Y_2Zr_2O_7$ grow epitaxially oriented on MgO on the (1 1 0) direction. These films have been characterized in details, since they allow for a study of the electrical behavior of the material free from grain boundaries contribution. In this case, these samples revealed substantial interface effects (in terms of electrical transport), which – as shown below – are closely related to the local microstructure.

4.2.1 TEM characterization

High-resolution-TEM micrographs show a homogeneous sample without grain boundaries and a rather sharp interface (see Figure 19a). The selected area electron diffraction (SAED) pattern in Figure 19b fully confirms the epitaxial relation between substrate and film, despite the very large lattice mismatch (a_{MgO}=4.12 Å, a_{YZO}=5.20 Å, theoretical mismatch: 26.21 %). As the peak positions of the SAED patterns correspond to the reciprocal lattice of the sample, the actual lattice mismatch can be evaluated by considering the reciprocal of the distance between two neighboring reflections (along one crystallographic direction, see Figure 19c) of both the thin film and the substrate. The ratio of these two distances yields the actual mismatch (23.56 %) at the interface.

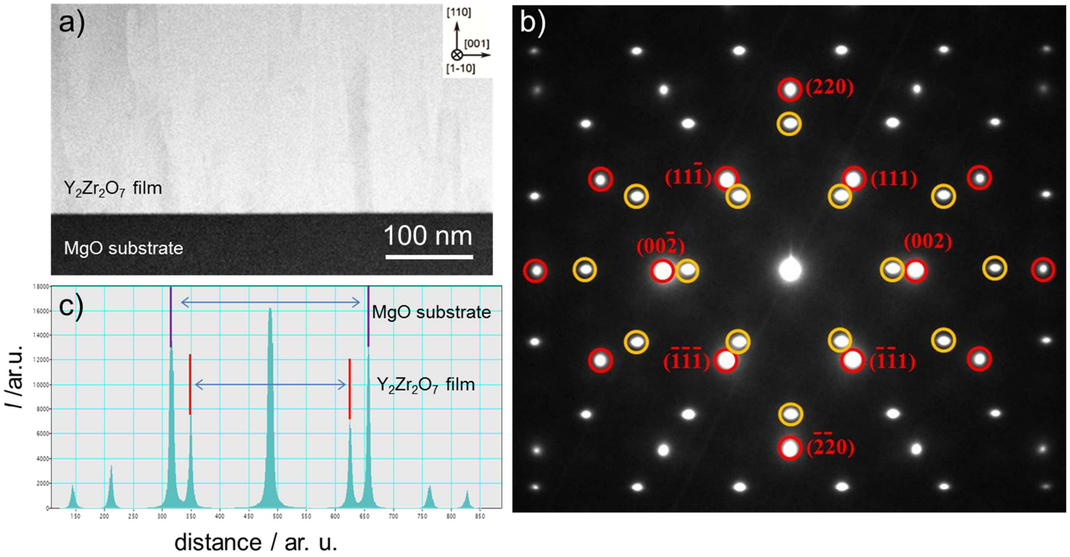

Figure 19: a) TEM micrograph of $Y_2Zr_2O_7$ thin film on MgO (1 1 0) showing the flat and sharp interface between film and substrate. b) Selected area electron diffraction of an interface between $Y_2Zr_2O_7$ thin film and MgO (1 1 0) substrate: Red and yellow circles highlight the reflections from MgO substrate and $Y_2Zr_2O_7$ layer, respectively. c) Relative distance obtained from the SAED {002} reflections, used for the calculation of the actual mismatch. The violet peaks refer to the substrate, while the red peaks refer to the thin film.

The resulting large strain is partially relaxed by the formation of misfit dislocations at the interface, where an half plane of MgO is interrupted and not connected to any plane in $Y_2Zr_2O_7$. This is clearly visible in the Fourier-transform filtered image shown in the inset of Figure 20a: the average distance between to neighboring misfit dislocations is 4.5 atomic planes.

Figure 20b instead depicts an image of the cross-section of a sample, which was exposed to oxygen at 700 °C for 8 hours during the impedance spectroscopy measurements. Interestingly, the micrograph indicates that the interface underwent a substantial structural modification during the heat-treatment. As shown by the Fourier-transform-filtered image, misfit dislocations are still present at the interface but their density is reduced: the average distance between misfit dislocations is here 5.4 atomic planes while in the pristine samples it was 4.5 atomic planes. Furthermore, the interface is no longer planar but exhibits a saw-shape-like configuration. This is most probably related to the fact that for the (1 1 0) surface of MgO the multifaceted configuration is the most stable, as it has been calculated from atomistic simulations in ref. [88]. It is therefore reasonable to assume that during the equilibration at 700°C, the thermal energy allowed the surface to acquire the most stable configuration.

It is worth noting that the configuration acquired by the interface allows for a partial relaxation of the strain [89, 90], therefore the thin film is locally subjected to a lower stress after annealing despite the lower density of misfit dislocations. This makes it difficult to estimate the effective strain, since the role of the multifaceted interface has to be taken into account.

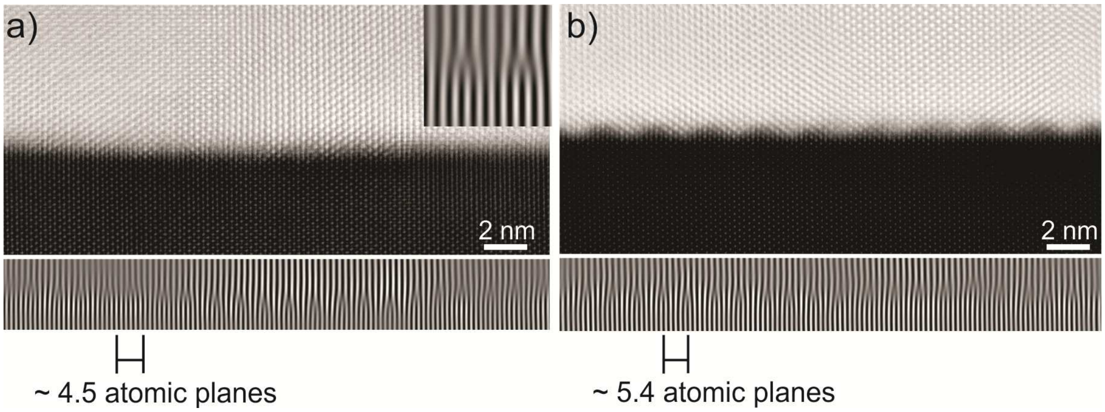

Figure 20: a) Fourier-transform-filtered image of a pristine sample, pointing out the high density of misfit dislocations. The average distance between them is 4.5 atomic planes. In the inset: magnification of a misfit dislocation formed between substrate and film. b) Fourier-transform-filtered image of a sample after the heating treatment. The average distance between misfit dislocations increases to 5.4 atomic planes.

EDX analysis has been performed on both pristine and annealed samples in order to determine whether the Y/Zr ratio is uniform through the layers. As shown in Figure 21, the cationic ratio remains constant along directions parallel to the interface in both samples (Figure 21 a,c), while perpendicularly to the film the Y/Zr ratio profile seems to indicate local intermixing at the interface between Mg, Y and Zr within a region of approximately half a nanometer (Figure 21c,d). However, as the average roughness of the substrates is about one unit cell (see Section 2.1), these profiles are most likely due to the roughness of the substrates rather than from a substantial cationic intermixing.

Nevertheless EDX analysis confirms the homogeneity of the samples, ruling out possible variations in the ratio between the two major cations. Therefore accumulation or depletion of charge carriers due to a local variation of the cationic stoichiometry can be excluded.

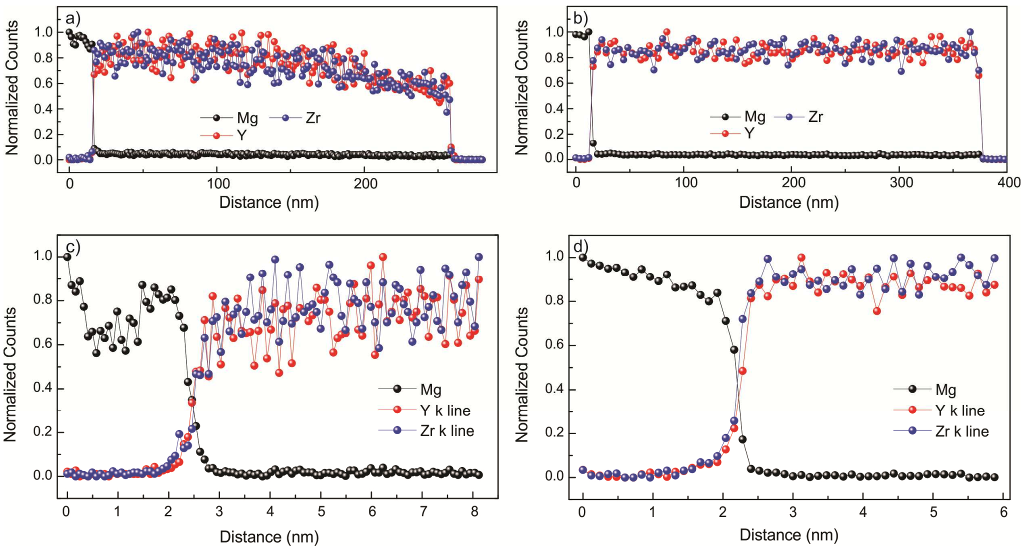

Figure 21: EDX analysis scans of a) and c) the pristine sample, b) and d) the sample after equilibration at 700°C. Panels a) and b) refer to scans parallel to the interface, while panels c) and d) correspond to scan perpendicular to the interface.

A more detailed analysis on the interface has been performed through electron energy-loss spectroscopy (EELS) by considering the oxygen *K*-edge (energy-loss range between 490 eV and 580 eV), which stems from the $1s \rightarrow 2p$ electronic transition and can provide important information on the local chemistry.

It is worthy of note here that EELS line-scans were acquired at the $Y_2Zr_2O_7$ / MgO interface simultaneously to EDX spectra (Figure 22a). The vertical green line in Figure 22b schematically indicates the line-scan direction along *x*. As shown in Figure 22c, three types of O-*K*-edge spectra can be readily distinguished due to different local chemical environment: in MgO (spectra 1 and 2), at the interface (spectra 3), and in $Y_2Zr_2O_7$ (spectra 4 and 5). Upon removal of the background contribution, the spectra across the interface (O-*K*-edge(*x*)) can be analyzed according to the multiple linear least squares (MLLS) fitting, which relies on the linear combination of the characteristic O-*K*-edge spectra of MgO and $Y_2Zr_2O_7$ (spectra 1 and 5, respectively) in terms of intensities *I*:

$$\text{O-}K\text{-edge}(x) = a(x)\cdot \text{O-}K\text{-edge}_{\mathrm{MgO}} + b(x)\cdot \text{O-}K\text{-edge}_{\mathrm{Y_2Zr_2O_7}}\,, \tag{4.1}$$

where a and b are numerical coefficients depending on the position x and ranging between 0 and 1. Obviously for spectrum 5, $a = 0$ and $b = 1$, while the opposite holds for spectrum 1.

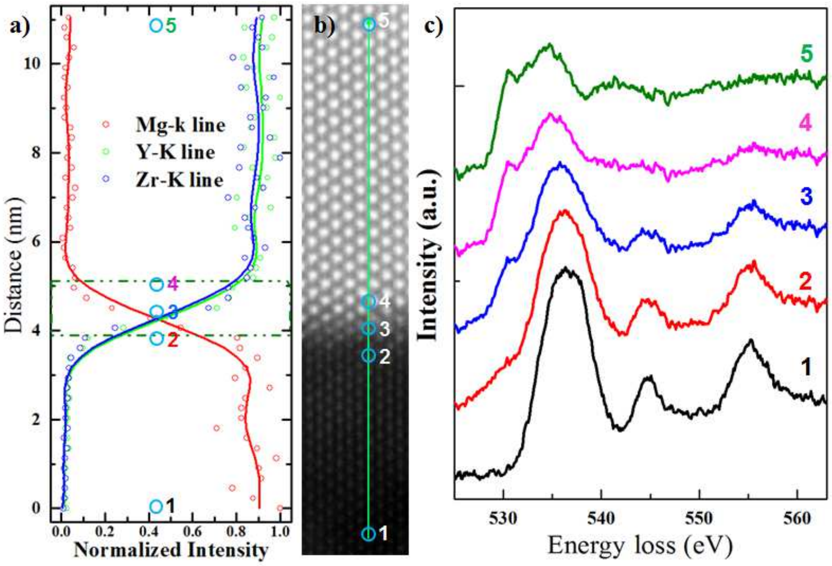

Figure 22: a) EDX spectra across the interface between $Y_2Zr_2O_7$ thin film on MgO (1 1 0) as deposited. b) Cross-sectional STEM-HAADF micrograph of the sample investigated also with EELS. The line-scan path is indicated in green. The numbered open circles indicate the position where the EELS spectra were acquired. c) The corresponding O-*K*-edge spectra acquired at the different positions. The numbers correspond to those in b): in the bulk of MgO (1), close to interface at MgO side (2), at center of interface (3), close to interface at $Y_2Zr_2O_7$ side (4), and in bulk of $Y_2Zr_2O_7$ (5).

The results of the MLLS analysis indicate that for the annealed sample the spectra collected over the film/substrate interface can be perfectly fitted by a linear combination of the O-*K* edge spectra collected from the MgO and $Y_2Zr_2O_7$ environment, respectively. On the contrary, the fitting of the as-deposited samples leads to a remarkable residual signal (the difference between the experimental spectra and MLLS fitting) at the interface indicating that oxygen ions perceive a local environment, which is different from the bulk situation. The comparison of the residual signal for the as-deposited and annealed sample is presented in Figure 23.

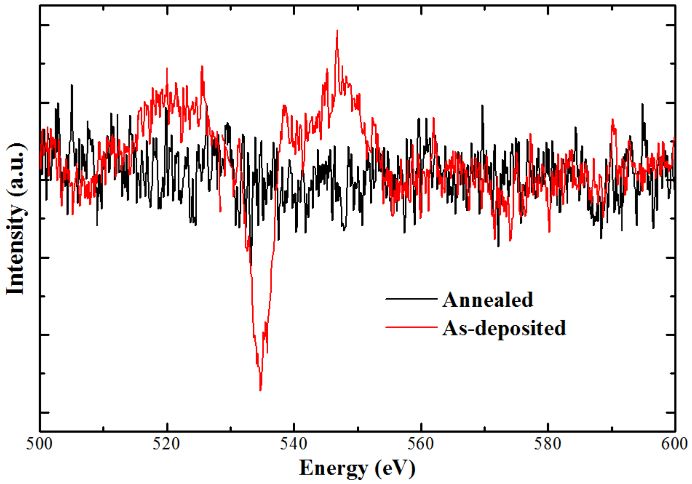

Figure 23: Comparison of the MLLS fitting residual signals obtained for the as-deposited (red) and the annealed (black) samples.

Now, it is worth considering that the largest difference in the residual signal is localized around 530 eV, which is the energy loss corresponding to the first peak (p_1) in the O-*K*-edge (at 531 eV). This originates from electronic transitions to the unoccupied Zr-*d* states hybridized with the oxygen 2*p* states [91-93].

Its intensity is determined using the non-linear least squares fitting (NLLS) method: The O-*K*-edge of $Y_2Zr_2O_7$ in the range of 528 and 548 eV is deconvoluted into three Gaussian contributions centered at approximately 531, 537 and 545 eV respectively and the intensity of the first Gaussian at 531 eV (corresponding to p_1) is considered. In order to investigate how p_1 varies with respect to the $Y_2Zr_2O_7$ situation, its intensity determined from the spectrum collected far from the interface (spectrum 5 in Fig. 22) is taken as the reference and set equal to 1.

In order to evaluate the intensity change of p_1 over the interface, we compare the intensity profile of p_1 with the intensity profile of the O-*K*-edge in the bulk of $Y_2Zr_2O_7$ (i.e. the profile of the coefficient *b* of equation 4.1). Figure 24a shows this comparison for the case of the as-deposited sample while Figure 24b refers to the annealed sample. Notably in the sample before annealing, the two profiles differ substantially within the first nanometer near the interface because of a large increase of the intensity of p_1 with respect to the rest of the spectrum. This indicates that at the interface the local environment surrounding the oxygen ions is different compared to the bulk case. After annealing instead, the intensity profiles match perfectly indicating the same chemical environment in the bulk and at the interface.

It is known from literature that the distance between the first two peaks at the O-*K*-edge of yttria stabilized zirconia (p_1 and p_2) is directly proportional to the yttrium fraction present in the compound [93].

In this case it is not possible to precisely estimate the relative position of both peaks because of the overlapping of MgO first peak with p_1 and p_2 of $Y_2Zr_2O_7$ (see Figure 22c).

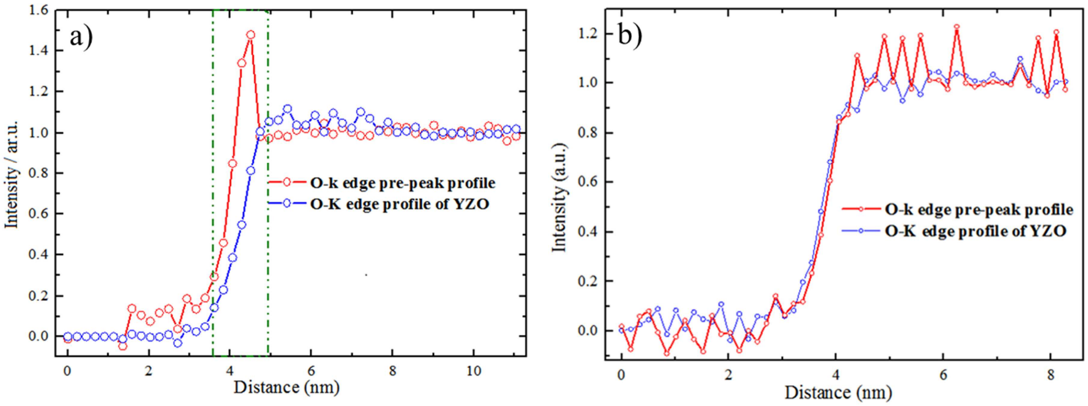

Figure 24: a) Intensity profile of the p_1 signal before annealing (red line) compared to the intensity profile of the whole spectra (blue line). The two profiles differ substantially. b) Fitting of the p_1 signal after annealing (red line) compared to the fit of the whole spectra (blue line).

4.2.2 Thickness dependence of the conductance

From the study of the thickness dependence of the conductivities, it is possible to obtain important information about the electrical properties of the interface between film and substrate.

Here, the conductance of four samples with thicknesses ranging from 70 nm up to 300 nm were measured between 450 °C and 700 °C in oxygen atmosphere. Note that thinner films were not considered because their conductance could become comparable to the conductance of the bare substrate. The corresponding impedance spectra are shown in Figure 25a. As expected from the consideration made in section 3.2.1, they consist of a single semicircle, whose finite intercept on the abscissa represents their total resistance.

As explained in paragraph 2.2.4 it is possible to free the conductance from the geometrical dimension perpendicular to the growth direction *x* by considering the following expression:

$$Y^{\parallel} = G^{\parallel} \frac{\Delta y}{\Delta z} = L\sigma^{\parallel}. \tag{4.2}$$

In our case *Δy* and *Δz* represent the distance between electrodes and the length of the electrode, respectively.

The sheet conductance $Y^{\parallel}$ consists of two terms: the bulk contribution $Y^{\parallel}{}_{\infty}$ and the interface contribution $\Delta Y^{\parallel}$ and it can be thus written as

$$Y^{\parallel} = Y^{\parallel}{}_{\infty} + \Delta Y^{\parallel}. \tag{4.3}$$

As shown in Figure 25 b, c and summarized in Table 6, the epitaxial films on MgO show a positive intercept in the range of temperature studied and in particular at intermediate temperatures (500 °C). This, also considering the standard deviation ($7\ 10^{-12}$ S cm^{-1}) is clearly larger than the substrate contribution, which is depicted in Figure 25 in gray.

It is noteworthy that after exposure to the maximum temperature (700 °C for 8 hours) this positive interface effect decreases (at 500 °C: from $1.6\ 10^{-11} \pm 7\ 10^{-12}$ S before heating to $8.1\ 10^{-12} \pm 6\ 10^{-12}$ S after exposure to 700 °C). The bulk conductivity also varies (from $4.6\ 10^{-6}$ S cm^{-1} to $3.6\ 10^{-6}$ S cm^{-1}) but its change is clearly less pronounced than the variation of the interface contribution. This points towards a possible dewetting of the Pt electrodes during the equilibration at 700 °C to vary the electrodes geometry and thus affect the measurement (a lower effective electrode surface results in a larger sample resistance) [78, 79, 94, 95]. This obviously affects also the value of $\Delta Y^{\parallel}$. If the Pt-dewetting would be the only cause of the changes of $Y^{\parallel}{}_{\infty}$ and $\Delta Y^{\parallel}$, then the relative variation of the interface conductance and the bulk conductivity would be identical. However, as in our measurement the variation of the bulk conductivity is less pronounced than the variation of the interface conductance (-20 % and -50 %, respectively), one can conclude that the detected change of the interface contribution is not only due to the electrode morphology modification but rather stems from a local modification of the interfacial transport mechanism.

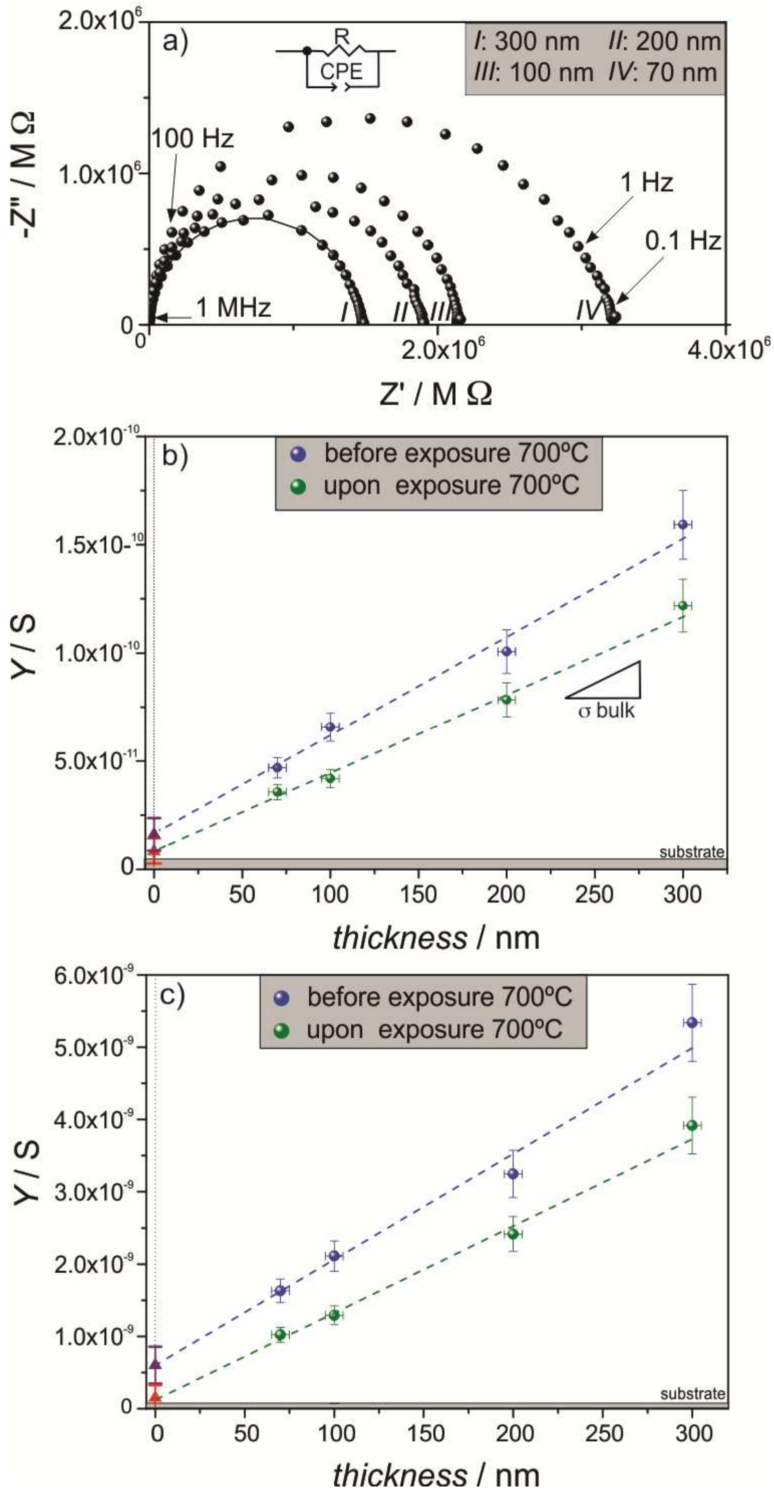

Figure 25: a) Impedance Nyquist plot of the epitaxial films of different thickness deposited on MgO (1 1 0) substrate acquired at 500 °C. b) and c) Sheet conductance as a function of the film thickness measured before and after exposure to 700 °C at 500 °C and 650 °C, respectively. Note that the contribution of the substrate to the overall conductance is marked in gray.

Table 6: Conductivities and activation energies of the different contributions obtained from the plot of sheet conductance as a function of the film thickness. The total activation energies of the films have been calculated within the same range of temperature.

	Interface	**Bulk**	**Film**			
			70 nm	**100 nm**	**200 nm**	**300 nm**
	Activation energy / eV					
Before annealing	1.5 ± 0.2	1.51 ± 0.06	1.48 ± 0.08	1.46 ± 0.09	1.5 ± 0.1	1.5 ± 0.1
After annealing	1.4 ± 0.3	1.53 ± 0.04	1.5 ± 0.1	1.5 ± 0.1	1.5 ± 0.1	1.50 ± 0.1
	Conductance at 500 °C / S		**Conductivity at 500 °C / S cm^{-1}**			
Before annealing	$1.6\ 10^{-11}$ $\pm\ 7\ 10^{-12}$	$4.6\ 10^{-6}$ $\pm\ 4\ 10^{-7}$	$6.7\ 10^{-6}$	$6.6\ 10^{-6}$	$5.0\ 10^{-6}$	$5.3\ 10^{-6}$
After annealing	$8.1\ 10^{-12}$ $\pm 610^{-12}$	$3.6\ 10^{-6}$ $\pm\ 6\ 10^{-7}$	$5.1\ 10^{-6}$	$4.2\ 10^{-6}$	$3.9\ 10^{-6}$	$4.1\ 10^{-6}$

4.2.3 Interpretation of the film – substrate interface effect

Firstly, it is worth mentioning that positive intercepts on the reduced conductance $Y^{\parallel}$ axis (see the graphs in Figure 25b-c) can indicate an accumulation of mobile charge carriers near the interface, which, according the defect chemistry of the present material, should be oxygen vacancies in this case (See Paragraph 2.2.1).

Let us now compare Figure 20 a, b with Figure 25 b and c. Before annealing a flat interface and a high density of misfit dislocations are correlated with a significant enhancement of the interface conductance. While after annealing, a saw–like shape interface with lower dislocation density is related to a moderate interface conductance. The comparison suggests a correlation between the enhanced ionic conductivity near the interface and the structure of the interface itself (e.g. presence of misfit dislocations and residual strain on the film), as already reported in literature for ionic conductors as single crystals of AgCl and multilayers of CaF_2/BaF_2 [96, 97].

Furthermore, let us consider the EELS analysis depicted in Figure 22c: the first two peaks (p_1 and p_2) are characteristic features of different compositions of yttria stabilized zirconia, since these originate from the interaction of the oxygen *2p* and zirconium *4d* wavefunctions [98].

The EELS analysis depicted in Figure 24a points out a substantial enhancement of the p_1 intensity in the fine structure of the O-*K*-edge compared to the rest of the spectra. Although it is unfortunately not possible to unambiguously assign the EELS observations to a specific situation at the interface (e.g. presence of oxygen vacancies, strain, misfit dislocations), it is yet possible to conclude that at the interface the oxygen ions are affected by a local environment which is different compared to the rest of the film. The EIS measurement suggests that such an environment affects substantially the local ionic conductivity.

Starting from these considerations, we can now analyze in more detail the role of the misfit dislocations on the increased interface conductance.

A first possible scenario is the segregation of oxygen vacancies in the core of the dislocations. However, it has been recently demonstrated by theoretical studies as well as by oxygen diffusion experiments on related oxygen vacancy conducting materials (namely CeO_2 and $SrTiO_3$) that conduction along the dislocation cores is very unlikely [32, 99]. It is also important to note, that the segregation of oxygen vacancies in the dislocation cores would result in an excess positive charge (and thus $\Delta\phi_0 > 0$) that would lead to a depletion of oxygen vacancies in proximity of the dislocations according to (see also section 2.2.3)

$$[V_O^{\bullet\bullet}]_0 = [V_O^{\bullet\bullet}]_\infty \exp\left(-\frac{2e\Delta\phi_0}{k_B T}\right), \tag{4.4}$$

where $[V_O^{\bullet\bullet}]_0$ is the concentration of the vacancies at the interface (just outside the core), $[V_O^{\bullet\bullet}]_\infty$ their bulk concentration, e the electron charge, $\Delta\phi_0$ the space charge potential and $k_B T$ the Boltzmann term. This means that also outside the dislocation core an enhancement of the ionic transport could not be possible. Therefore, the situation corresponding to having excess oxygen vacancies in the dislocation cores leading to a locally enhanced ionic conduction can be discarded.

As interfaces which such a high density of misfit dislocations are unlikely to be electrically neutral, the alternative scenario that needs to be considered is that dislocation cores are negatively charged. This could result from the segregation of negatively charged defects, such as $V_{Mg}^{//}$ (note that the misfit dislocations arise from the interruption of MgO planes). In this context, it is worth noting that theoretical calculations on Schottky defects in MgO estimated the excess energies of magnesium vacancies and oxygen vacancies at the edge dislocations. These are respectively -1.7 eV and -1.5 eV suggesting preferential segregation of $V_{Mg}^{//}$ to the dislocation cores in MgO. The lowest energy positions for the magnesium and oxygen vacancies at the dislocation are found at the tip of the extra half plane of atoms [100]. The preferential segregation of $V_{Mg}^{//}$ in the misfit dislocations at the interface can result in a negative potential that can in turn enhance the concentration of positively charged defects in the adjacent $Y_2Zr_2O_7$ and result in a locally improved ionic transport as it is observed experimentally.

4.2.4 Oxygen vacancy accumulation at the interface: further considerations

The accumulation of oxygen vacancies due to a negative potential at the interface might resemble a Gouy – Chapmann case (See Paragraph 2.2.3.1), in which the excess charge at the interface is compensated by a steep accumulation of the majority charge carrier of opposite charge in the film. In this particular case however, further considerations have to be made.

Firstly, we note that $Y_2Zr_2O_7$, contains a large dopant concentration, and hence a large concentration of oxygen vacancies ($2[V_O^{\bullet\bullet}]_\infty = [Y_{Zr}^{/}]_\infty$), namely one vacancy per unit cell. Therefore, the crystal structure cannot accommodate a significant number of additional vacancies in the case of an accumulation. Rather, the $[V_O^{\bullet\bullet}]_0 / [V_O^{\bullet\bullet}]_\infty$ ratio cannot exceed eight. (We note that at 500°C this corresponds to $\Delta\phi_0$ = -70 mV). Such an upper limit might lead to a situation, in which the concentration of enriched vacancies is constant (flat concentration profile) in proximity of the interface ($0 < x < \ell$) as schematically illustrated in Figure 26.

For the further discussion on space-charge and/or mobility effects we consider this simplified situation. In this case, one can write:

$$Y^{\parallel} = \sigma_\infty L + \Delta Y^{\parallel} \simeq 2e\left\{u_\infty \left[V_O^{\bullet\bullet}\right]_\infty L + u_0 \left\{\left[\left[V_O^{\bullet\bullet}\right]_0 - \left[V_O^{\bullet\bullet}\right]_\infty\right]\right\}\ell\right\}, \tag{4.5}$$

where u_0 and u_∞ are the oxygen vacancies' mobility at the interface and in the bulk, respectively.

By referring to the plot of $Y^{\parallel}$ vs film thickness (L) (See Figure 25 b,c), the intercept on the x axis ($\bar{L}$) in this case corresponds to:

$$\bar{L} = -\frac{u_0\left\{\left[V_O^{\bullet\bullet}\right]_0 - \left[V_O^{\bullet\bullet}\right]_\infty\right\}}{u_\infty \left[V_O^{\bullet\bullet}\right]_\infty}\ell. \tag{4.6}$$

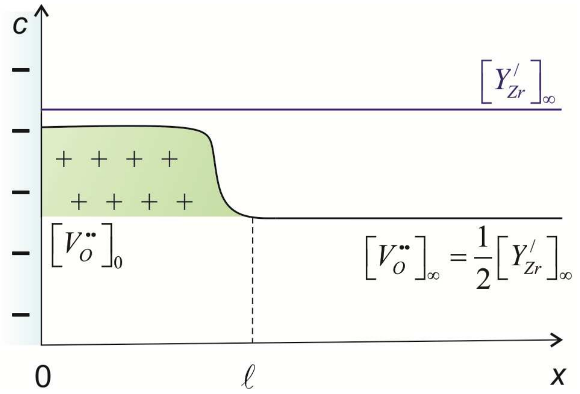

Figure 26: Schematic representation of the majority charged defect profile in thin films of $Y_2Zr_2O_7$ near the interface with MgO (1 1 0).

From the experimental data of Figure 25, $\bar{L}$ results to be equal to -26.2 nm. Starting from this value and by taking ℓ = 1 nm (see Figure 24) and $[V_O^{\bullet\bullet}]_0 / [V_O^{\bullet\bullet}]_\infty$ = 8 (the upper limit), it is evident that the mobility at the interface needs to be larger than in the bulk in order to fulfill eq. 4.6. (Note that if a lower value of the vacancy concentration ratio is taken, then the increase of u_0 is obviously larger). Referring to the upper limit $[V_O^{\bullet\bullet}]_0 / [V_O^{\bullet\bullet}]_\infty$=8, an increase of u_0 of 4 times follows, while a reasonable increase of the oxygen vacancies concentration by 4, corresponds approximately to $u_0 = 9\,\mathrm{u}_\infty$. This means that together with an enhancement of the oxygen vacancy concentration due to weak space-charge effects resulting from the segregation of magnesium vacancies at the misfit dislocations, a perceptible improvement of the mobility at interface occurs, which is most likely related to the local distortion of the crystal lattice.

Taking into account the mobility of the charge carriers, the association of defects and the potential at the interface, the resulting activation energy can be written as [74]:

$$E_a = \left(\Delta H_m + \frac{1}{T} \frac{\partial \Delta H_m}{\partial \frac{1}{T}} \right) + \left(\Delta H_{ass} + \frac{1}{T} \frac{\partial \Delta H_{ass}}{\partial \frac{1}{T}} \right) + \left(2e\Delta\phi_0 + \frac{1}{T} \frac{\partial \Delta\phi_0}{\partial \frac{1}{T}} \right) \tag{4.7}$$

where ΔH_m is the migration enthalpy, ΔH_{ass} the association enthalpy and $\Delta\phi_0$ the electric potential term.

Migration enthalpy and association enthalpy are independent of the temperature, while the term of association can be neglected only at high temperature [101]. For example for 8 YSZ, the total activation energy corresponds to the sole migration energy above 650 °C [102]. For a highly doped system the contribution of defect interaction to the activation energy is significant in the range of the temperatures studied [103].

The space charge potential value is anyway rather small and cannot sensibly influence the activation energy. Moreover, due to the large dopant concentration in $Y_2Zr_2O_7$ and the fixed concentration of misfit dislocations in the considered temperature range (300 – 500°C), its temperature dependence is assumed here to be negligible.

Therefore the main contribution to the activation energy is due to ΔH_m. A variation of the mobility of 9 times before and after annealing would mean to a variation of 0.1 eV in the total activation energy. Since the calculation of the activation energy for the conduction at the interface is affected by an uncertainty of 0.3 eV, this effect is too small to be detected.

4.2.5 Section conclusions

In this section the interface effect between $Y_2Zr_2O_7$ thin films and MgO substrates was studied in detail.

Samples of different thicknesses were measured under the same conditions and in the same range of temperatures; the sheet conductance of these layers, plotted as function of the thickness, pointed out an enhanced conductance near the interface that decreases after exposure at 700 °C for 8 hours. At the same time TEM characterization revealed a high density of misfit dislocations at the interface together with structural modifications upon annealing.

These results are here correlated to the EELS analysis of the O-*K*-edge, which in the pristine samples points out an enhanced p_1 peak intensity at the interface compared with the bulk.

An interpretation of the enhanced conductance in the framework of the space charge zone and increased mobility is proposed. A negative potential at the interface, probably due to the segregation of charged defects ($V_{Mg}^{//}$) in the dislocations core, would cause to accumulation of oxygen vacancies and consequent enhanced interface conductance The analysis of the EIS data suggests also an increased mobility of the carriers near the interface.

The experimental data suggests that the lower density of misfit dislocations and the structural modifications at the interface upon annealing, lead to a variation of the negatively charged interface and a decreased mobility of the carriers.

4.3 Characterization of the strain effect on $Y_2Zr_2O_7$ – 8 % Yttria stabilized zirconia multilayers

As explained in chapters 1.1 and 2.3 strain can generally have a substantial effect on the ionic conductivity of the materials; however the results reported in literature are very scattered and they vary from negligible effects to significant improvements (by even several orders of magnitude) of the conductivity. Such a disperse collection of data and the lack of explanations for such large variety of experimental findings make it necessary to further investigate strain effects on suited thin films and multilayers systems.

Moreover, such studies need to be carried out taking into account (and minimizing) spurious contributions such as the possible effect of extended defects (dislocations and grain boundaries), which can release the strain and affect the ionic conduction [24, 104]. Possible contributions from the substrate have also to be considered, as well as the geometry of the electrodes, in order to ensure a reliable measurement of the conductivity along the interfaces [11].

In this chapter, the characterization of the electrical properties of multilayers consisting of alternated films of 8YSZ and $Y_2Zr_2O_7$ for the investigation of strain effects is described. This system has been chosen for the many advantages that it presents as described in the following.

Firstly the presence of the same cations in both materials removes the principal driving force for an intermixing between $Y_2Zr_2O_7$ and 8YSZ.

Quite importantly, the lattice mismatch between these two materials is moderate (1.6 % since a_{YSZ} = 5.12 nm and a_{YZO} = 5.20 nm). This allows for high quality epitaxy resulting in a tensile strain on the YSZ layer (which is expected to enhance its ionic transport properties) but hindering the formation of extended defects (dislocations and grain boundaries), which would alter the local effective strain field.

Furthermore, the conductivity of 8YSZ is orders of magnitude higher than that of $Y_2Zr_2O_7$ and hence the total conductivity of the heterolayers is expected to stem from yttria-stabilized zirconia. In this was, it is possible to monitor the possible effect strain on YSZ while variations in the ionic conduction of $Y_2Zr_2O_7$ on the total conductivity can be neglected.

Heterolayers with a total overall thickness of about 70 nm and different number of interfaces were deposited on MgO (1 1 0) substrates by varying the thickness of the single layers down to a minimum theoretical thickness of 5 nm. Since as it was shown in the previous chapter, thin films of $Y_2Zr_2O_7$ grow epitaxial without grain boundaries (See paragraph 4.1.2), in all the samples, the first layer in contact with the substrate (MgO) was a layer of $Y_2Zr_2O_7$. A schematic representation of the samples is shown in Figure 27.

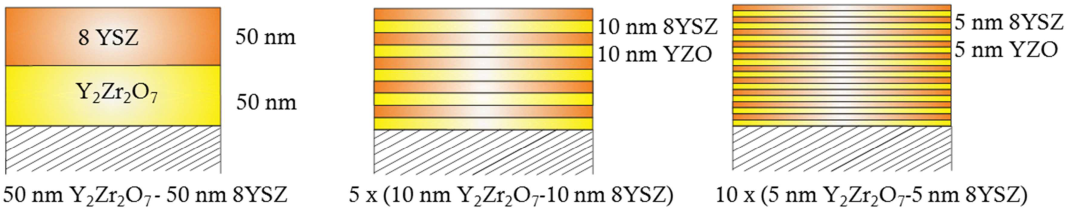

Figure 27: Schematic representation of the multilayers investigated here. The total thickness of the samples is kept constant while the number of interfaces is increased.

Characterization by XRD analysis (Figure 28) shows two peaks for the bilayer, while for the other heterostructures, the peaks are split in first order satellites peaks (SL_1 and SL_{-1}). Generally, the presence of the satellites peaks indicates the high quality of the interface, since they generate from the periodicity of the multilayers. The angular spacing of the satellites peaks depends on the thickness of the layers that can be calculated as [105]:

$$\Lambda = \frac{\lambda_{Cu}}{(\sin\theta_1 - \sin\theta_2)} \tag{4.8}$$

Where Λ is the thickness of the constituting the ($Y_2Zr_2O_7$/8YSZ) unit, λ_{Cu} the radiation wavelength (here the Cu Kα radiation), θ_1 and θ_2 denote the angular spacing of the satellite peaks obtained from the XRD patterns.

The position of the satellite peaks have been calculated by fitting the experimental data with a Pearson type VII distribution function [106]. The effective real thickness of the layers calculated from the XRD patterns are: 11.8 nm for the 5 interfaces sample (indicated as 5 (10 nm - 10 nm)) and 6.8 nm for the 10 interfaces sample (10 (5 nm - 5 nm)).

Therefore, the total thickness is estimated to be about 60 nm for the first multilayer and 70 nm for the second one. The total thickness of the single interface sample could not be calculated from the XRD. However from the number of deposition pulses and the growth rate of the two oxides it is estimated to be about 60 nm.

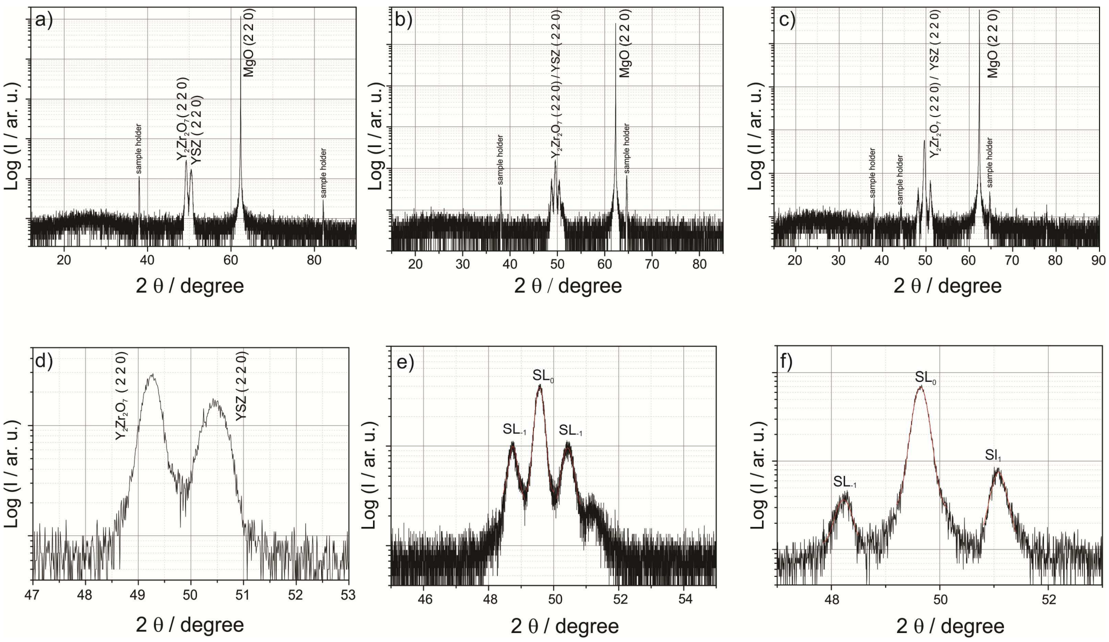

Figure 28: XRD patterns of YSZ/$Y_2Zr_2O_7$ heterostructures on MgO (1 1 0) having roughly the same overall thickness but different number of interfaces: 1 for a), 5 for b) and 10 for c). In panels d), e) and f) the magnification of the corresponding reflections showing the additional peaks due to the interfaces are displayed. The satellites peaks SL_1 and SL_{-1} allow for the calculation of the constituting unit (a single pair of YSZ and $Y_2Zr_2O_7$ layers) thickness: 11.8 nm from Figure 28e (5 (10 nm - 10 nm) and 6.8 nm from Figure 28f (10 (5 nm - 5 nm).

In order to measure the electrical properties uniformly through the overall thickness of the multilayers, samples have been etched along the sides and Pt has been deposited into the resulting trenches. For comparison a single layer of YSZ has been deposited on MgO (1 1 0) in the same conditions and the same Pt electrodes have been applied.

The temperature dependence of the conductivity of single layers and multilayers are compared in Figure 29. The substrate-interface between $Y_2Zr_2O_7$ and MgO (1 1 0) measured on single layers (Paragraph 4.2) is negligible in these system since the enhancement of the conductance at the interface is 4 order of magnitude lower than the total conductance of the multilayers.

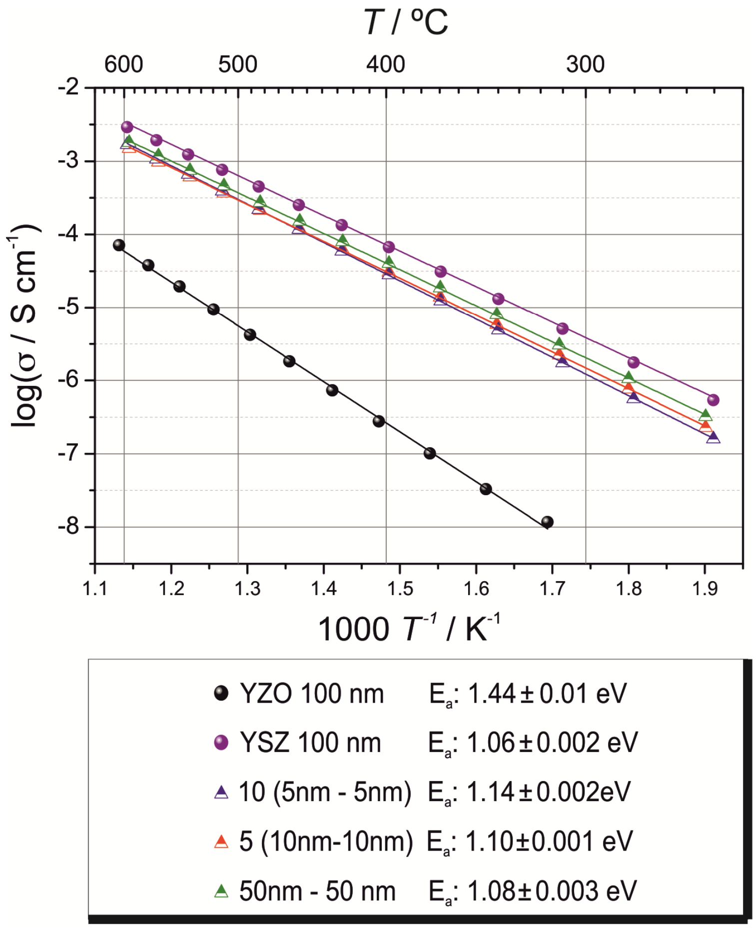

Figure 29: Temperature dependence of the conductivity of 8YSZ – $Y_2Zr_2O_7$ multilayers with different number of interfaces. For comparison also the data of single layers of 8YSZ and $Y_2Zr_2O_7$ are displayed.

Values of conductivity and activation energy for the single layer of YSZ are in agreement with values reported in literature; Joo *et al.* [107] reported values of conductivity at 600 °C of 3 10^{-3} S cm^{-1} (here the measured conductivity is 2.9 10^{-3} S cm^{-1}) and activation energy of 1.01 eV on YSZ film of thickness 0.6 μm deposited via PLD.

The multilayers system can be considered as a system of conductances in parallel, therefore the expected total conductivities can be calculated according to Kirchoff's law. Starting from the conductivities of the constituting oxides, the calculated conductivity of the multilayers is 1.5 10^{-3} S / cm^{-1} at 600 °C.

The actual values measured at 600 °C are: 1.7 10^{-3} S/cm^{-1} for the 10 (5 nm - 5 nm) multilayer, 1.5 10^{-3} S/cm^{-1} for the 5 (10 nm - 10 nm) multilayer and 1.8 10^{-3} S/cm^{-1} for the bilayer. Such a small difference between calculated and measured values indicates that the conductivity of the heterolayers is neither varied by the number of interfaces nor by the different thicknesses. The small variation in the activation energy instead (from 1.08 eV for the bilayer to 1.10 eV for the 5 (10 nm - 10 nm) and 1.14 eV for the (10 (5 nm - 5 nm) samples) seems to suggest a light hindering effect on the ionic transport, which increases with decreasing layer thickness. However, we note that such an effect is very small as it does not really affect the conductivity values of the different samples (bilayer vs 10 (5 nm - 5 nm) vs 5 (10 nm - 10 nm)).

As shown previously, the actual mismatch measured between $Y_2Zr_2O_7$ (1 1 0) and MgO (1 1 0) is 23 %, yet thin films of $Y_2Zr_2O_7$ grow epitaxially on MgO substrate (See paragraph 4.1.2) thanks to the formation of numerous misfit dislocations.

It has been calculated from thermodynamic consideration that the strain alters the ionic transport and its effect is proportional to the mismatch between layers (this is strictly valid only for epitaxial systems) [64]. Here, however we recognize that even in perfectly epitaxial systems with high quality of the interfaces (confirmed by XRD analysis) below the critical thickness, where the strain is not released through one-dimensional or two-dimensional defects, the mismatch of 1.6 % does not lead to perceptible improvements of the ionic transport properties.

In this framework, our results agree with the observations reported by Pergolesi *et al.* in Ref. [24] on multilayers of CeO_2/YSZ (which however contained a moderate number of misfit dislocations at the interfaces), in which it was shown that a mismatch up to 5 % does not produce any significant effect on the oxygen diffusion or ionic conductivity, in their case neither on the activation energy.

In contrast to these conclusions are however the results of Li *et al.* [21], who observed a different behavior of their multilayered $Gd_2Zr_2O_7$ and YSZ heterostructures with a variable number of interfaces. They detected a substantial variation of the ionic conductivity (an increase of 2 orders of magnitude when moving from 10 to 20 interfaces) for a lattice mismatch of about 3%, while no information were given on the effects on the activation energy.

4.3.1 Section conclusion

Multilayers of YSZ/$Y_2Zr_2O_7$ of total thickness of about 70 nm with different number of interfaces have been successfully grown on MgO (1 1 0) substrate. The characterization via XRD confirmed the high quality of the interfaces and allowed a precise calculation of the layer thicknesses. In our case the choice of materials with moderate mismatch successfully avoided the formation of extended defects, while the ad-hoc designed electrodes ensured a reliable characterization of the electrical transport properties along layers and interfaces. The resulting conductivity data pointed out negligible effects of the strain on the ionic conductivity of YSZ.

5 CONCLUSIONS

The present thesis deals with the characterization of thin films of $Y_2Zr_2O_7$ and addresses various aspects of grain boundaries contribution, film-substrate interface effect as well as strain effect on the overall ionic transport properties of this material.

$Y_2Zr_2O_7$ has been chosen as a model system within the broad family of pyrochlores and defective fluorites, because of its high chemical stability and large ionic transference number over a broad range of temperatures and oxygen partial pressures.

This work underlines the importance of thin films' characterization for the study of grain boundaries, film-substrate interface effect and space-charge effect, as well as for the investigation of aspects, which are up to now subject of controversial interpretations, such as the role of dislocations and strain effects on the ionic migration.

Powders have been synthetized via nitrate aqueous solutions and from these targets for the thin films deposition and a microcrystalline pellet and have been pressed and sintered. Thin films have been grown on different substrates via pulsed laser deposition technique and characterized with various analysis methods (XRD, pole figures, TEM, EELS); the electrical properties have been studied via impedance spectroscopy. Textured thin films have been obtained on Al_2O_3 (0 0 0 1) and Al_2O_3 (1 -1 0 2), while epitaxial thin films have been grown on MgO (1 1 0).

While it was not possible to detect the grain boundaries specific resistance directly from the microcrystalline pellet, the comparison of thin films with different microstructure allowed for the investigation of the contribution of the grain boundaries on the ionic migration. From this the poorly blocking behavior of the grain boundaries resulted, which decreases the conductivity of textured thin films compared to the epitaxial films by less than half an order of magnitude. In the case of a microcrystalline ceramic the decrease amounts one order of magnitude. Such limited blocking effects are particularly small if compared with closely related system, e.g. 8YSZ, which are reported in the literature.

The most relevant result is the perceptible positive interface effect between epitaxial layers of $Y_2Zr_2O_7$ and the MgO substrate. Indeed, the extrapolation of the conductance values obtained from epitaxial films with different thicknesses indicates an ‘excess ionic conductance’ *via* oxygen vacancies at the interface.

The local microstructure and chemical composition has been therefore characterized in details by HR-TEM, EELS and EDX. These analyses showed perfectly epitaxial thin films, free from grain boundaries, with homogeneous composition throughout the thickness in both directions parallel and perpendicular to the interface. The large compressive strain on the thin film due to the mismatch with the substrate naturally brings to the formation of a high density of misfit dislocations, which decreases after annealing at 700 °C. Similarly, the enhancement of the ionic conductivity near the interface also decreased upon annealing.

In the pristine samples, EELS analysis of the oxygen-*K*-edge showed an increased intensity of the oxygen p_1-peak (which is related to the transition to *d*-states of Zr hybridized with oxygen 2*p* states) near the interface with MgO substrate when compared to the bulk. This indicates a different chemical environment of the oxygen at the interface before annealing. In contrast, no particular p_1-peak intensity variation at the interface was detected in the annealed sample.

Accumulation of oxygen vacancies at the $Y_2Z_2O_7$ side of the interface compensate the segregation of negatively charged defects (according to the literature magnesium vacancies) in the dislocations core (MgO side of the interface). Moreover the analysis of the EIS data suggests also an enhancement of the mobility of the charge carriers near the interface.

Furthermore the characterization of heterolayers of $Y_2Zr_2O_7$ / YSZ with respect to strain effects on the ionic transport mechanism in YSZ is presented. Multilayers with different numbers of interfaces and similar total thickness, as well as single layers have been deposited via pulsed laser deposition. The EIS characterization pointed out the minor role of the strain on the ionic conductivity of YSZ: the measured effective conductivities obtained from the multilayers were virtually identical to those calculated from the resistance of the single layers.

In summary, this study highlights two important aspects regarding interface effects in ionically conducting oxides that can be crucial for the further improvement of the ionic transport of such materials. Firstly, the enhanced interfacial conductance between film and substrate results from two concomitant beneficial effects: the increase of the mobile charge carrier concentration (owing to space charge effects) and their improved mobility. This important finding is particularly relevant if we consider that most of the contributions in the literature usually invoke only one of the two effects to explain the occurrence of interface effects. Therefore we believe that the present contribution will be helpful for a more comprehensive approach in the study of such phenomena in the future.

Secondly, the careful fabrication of high quality, fully epitaxial multilayers together with the detailed investigation of their electrical transport properties allow for gaining insights on the effect of the lattice mismatch (here 1.6 % tensile) on the ionic transport of the highly conducting YSZ. Remarkably, the absence of any conductivity improvement (even in the heterostructures consisting of very thin layers) reveals that strain effects alone do not have a perceptible role for enhancing the ionic transport properties of YSZ. We believe that this outcome can represent a useful contribution for shading light onto the highly debated role of strain effects on the ionic transport.

6 APPENDIX

6.1 Deposition and electrical characterization of thin films of Lanthanum Apatite

6.1.1 Motivation

Lanthanum silicates with the apatite structure (with general formula $La_{9.33+x}(SiO_4)_6O_{2+3x/2}$) exhibit oxygen ion conductivity, which can be comparable to the one of some of the most conductive materials for SOFCs electrolytes, e.g. yttrium stabilized zirconia (YSZ) and gadolinium doped ceria (GDC) [108-118]. As discussed more in detail below, it is the ionic transport resulting from the migration of oxygen interstitials rather than oxygen vacancies which is rather uncommon for an oxide electrolyte makes these apatites particularly interesting [119, 120].

Although, the ionic transport of YSZ and GDC thin films have been extensively studied over the last years , very little has been done on thin films of $La_{9.33}(SiO_4)_6O_2$. Only two contributions in the literature report on the growth of lanthanum silicates (mostly polycrystalline) thin films. Briois *et al.* [121] described the characterization of two lanthanum silicates apatites ($La_{9.33}(SiO_4)_6O_2$ and $La_{10}(SiO_4)_6O_3$), which were obtained *via* co-sputtering deposition of metallic La and Si followed by annealing at high temperature in air. Karthikeyan *et al.* [122] obtained heterostructures of $Gd_xCe_{9.33-x}SiO_{26+x}$ by reducing (at low oxygen partial pressures) multilayers of GDC and SiO_2 deposited *via* radio-frequency sputtering.

The aim of the thesis project is deposition and electrical characterization of $La_{9.33}(SiO_4)_6O_2$. thin films via pulsed laser deposition (PLD). We decided to employ this deposition method since (i) it is a very well-established technique for the fabrication of oxide thin films and multilayers [123] and (ii) it offers a better control of the cationic composition. As it has been mentioned above, to the best of our knowledge this is the first attempt of fabricating such films by using the PLD technique and not by sputtering.

Interestingly, this study represents the first step towards the possibility of realizing in the future heterostructures of alternated oxygen vacancy and oxygen interstitial conducting oxides (e.g. YSZ and $La_{9.33}(SiO_4)_6O_2$). Boundary effects may be expected analogues to p-n junctions in semiconductors or to BaF_2/CaF_2 heterostrucures [37] and even. Here are presented the results obtained so far on the deposition and characterization of single layers.

6.1.2 Structure and defect chemistry of $La_{9.33}Si_6O_{26}$

$La_{9.33}Si_6O_{26}$ (space group: P-3, hexagonal structure, a = 9.7248 Å, c = 7.1895 Å [124]) belongs to the family of lanthanum silicate apatites, with the general formula $A_{9.33+x}(SiO_4)_6O_{2+3x/2}$, where A is a rare or alkaline-earth cation. In these compounds, the ionic conduction increases with increasing ionic radius of A^{3+} [108] or by enhancing the oxygen content [114, 125, 126] through a higher content of lanthanum. However, compositions with excess oxygen can result in the formation of as La_2SiO_5 second phase. The upper limit for a stable apatite in terms of oxygen content is not precisely defined: for the composition $A_{9.33+x}(SiO_4)_6O_{2+3x/2}$ values between x<0.34 and x<0.27 are reported in literature [110, 117].

In the stoichiometric compound, the defect chemistry can be treated as resulting from the Schottky and Frenkel disorders [127, 128]. In Kröger-Vink notation these are described by the following reactions:

$$V_i^x + O_O^x \rightleftarrows O_i^{//} + V_O^{\bullet\bullet} \qquad K_F = [O_i^{//}][V_O^{\bullet\bullet}] = \exp\left(-\frac{\Delta G_F^0}{RT}\right) \tag{6.1}$$

$$2La_{La}^x + 3O_O^x \rightleftarrows 2V_{La}^{///} + 3V_O^{\bullet\bullet} + La_2O_3 \qquad K_S = [V_{La}^{///}]^2[V_O^{\bullet\bullet}]^3 = \exp\left(\frac{-\Delta G_S^0}{RT}\right) \tag{6.2}$$

Calculated reaction energies suggest that anti-Frenkel disorder is more favorable. Cationic Frenkel disorder is instead highly unfavorable [124].

Also the electron-electron transfer reaction has to be taken into account:

$$nil \rightleftarrows e^{/} + h^{\bullet} \qquad K_e = n\,p\,. \tag{6.3}$$

At low oxygen partial pressure, the oxygen excorporation reaction can be described as:

$$O_i^{//} \rightleftarrows \frac{1}{2}O_{2(g)} + 2e^{/} \qquad K_{red} = \frac{n^2\,pO_2^{1/2}}{\left[O_i^{//}\right]}, \tag{6.4}$$

while under oxidizing conditions the oxygen incorporation can be expressed as follows:

$$\frac{1}{2}O_{2(g)} \rightleftarrows O_i^{//} + 2h^{\bullet} \qquad K_{ox} = \frac{\left[O_i^{//}\right]p^2}{pO_2^{1/2}}. \tag{6.5}$$

Where $K_{ox} = K_e^2 / K_{red}$.

In the intrinsic regime, the neutrality condition requires

$$2\left[O_i^{//}\right] + n + 3\left[V_{La}^{///}\right] = 2\left[V_O^{\bullet\bullet}\right] + p, \tag{6.6}$$

in which, due to the large formation energy of lanthanum vacancies, $\left[V_{La}^{///}\right]$ can be considered as negligible [124].

The crystal structure is formed by a network of SiO$_4$ tetrahedra, which create voides occupied by the A^{3+} cation. Additional oxygens surrounded by the A^{3+} cations constitute channels parallel to the *c*-axis through which the interstitial oxygens can migrate leading to the high ionic conductivity. The migration energy for this pathway has been calculated to range between 0.32 eV and 0.87 eV [110, 124].

The stoichiometric composition $La_{10}Si_6O_{27}$ and the La deficient compound $La_{9.33}SiO_6O_{26}$ show higher conductivity and lower activation energy of the compound with lower oxygen content $La_8Sr_2Si_6O_{26}$ [124, 129]. In the first case the oxygen proceeds via interstitial oxygen [124, 129], while in $La_8Sr_2Si_6O_{26}$, where according to theoretical calculations electrical transport occurs via oxygen vacancies, the conductivity is orders of magnitude lower [119, 125].

Interestingly, the ionic conductivity can dominate the electrical transport properties over a broad range of oxygen partial pressure (e.g. down to 10^{-18} bar at 900 °C) [116].

Consequence of this structure is a strong anisotropy of the oxygen transport, which is higher in the direction parallel to *c*-axis and hindered in the perpendicular directions [110]. According to the literature, the migration along the oxygen channels is theoretically possible in two different ways, linear and sinusoidal around the La^{3+} cations. It has been calculated that the most favorable path is the sinusoidal one, corresponding to a the lower migration energy [124, 128, 130].

Previous studies succeeded in separating the contributions to the conductivity perpendicular and parallel to the *c*-axis for different stoichiometries and for various content ofrare-earth cations [118, 131, 132]. The ionic conductivity variations range from one order of magnitude for $A_{9.33}(SiO_4)_6O_2$ ($A=Pr^{3+}$, Nd^{3+}, Sm^{3+}), up to three order of magnitude for $La_{9.33}(SiO_4)_6O_2$.

6.1.3 Single layers growth optimization

In order to obtain single phase thin films of $La_{9.33}(SiO_4)_6O_2$ (LSO) with defined stoichiometry and high crystallinity, deposition on different substrates and with different growth parameters (which are summarized in Table 7) was attempted.

Table 7: Summary of the growth parameters and substrates used for the deposition of LSO thin films.

Parameter	**Values**
Substrate	$SrTiO_3$ (1 0 0), MgO (1 0 0), Al_2O_3 (0 0 0 1)
Pulse Frequency	1, 2 and 5 Hz
Temperature on the substrate	From 620 °C up to 800 °C
Background oxygen pressure	From 0.01 mbar up to 0.5 mbar

Firstly the role of the substrate on the growth of LSO single layers was investigated: Since the evaluation of the mismatch between film and substrate is not trivial due to the complicated structure of the apatite compound, LSO was depositedon insulating substrates with different lattice parameter, namely $SrTiO_3$ (1 0 0) $(a_{STO} = 3.91\,Å)$, MgO (1 0 0) $(a_{MgO} = 4.21\,Å)$, Al_2O_3 (0 0 0 1) $(a_{Al_2O_3} = 4.76\,Å)$. Thin films were deposited with identical numbers of laser pulses on the various $5 \times 5 \times 0.5$ mm^3 substrates at 660 °C.

The as deposited films resulted to be amorphous on all substrates, as pointed out by the absence of peaks in the corresponding XRD patterns (Figure 30 a,d,g). Post-deposition annealing treatments at 900 °C for 1 hour in air, led to the formation of polycrystalline layers (Figure 30 b,e), while after a prolonged heat-treatment (10 hours), more peaks corresponding to the second phase $La_2Si_2O_7$ (Figure 30 c,f,h) were observed. Particularly important is also the role of the laser pulse frequency: a decrease from 5 Hz down to

2 Hz enabled the direct fabrication of polycristalline thin films on Al_2O_3 (0 0 0 1) without the need of a subsequent heat-treatment (Figure 31 a,b). Interestingly, a further decrease down to 1 Hz was not beneficial since it resulted in the formation of amorphous films (Figure 31 c).

Also the background pressure during the ablation of the films plays a perceptible role on their final microstrucure. For example, an increase from 0.01 mbar to 0.1 mbar allowed for obtaining thin films predominantly oriented along the (1 0 2) direction on Al_2O_3 (0 0 0 1), while a better crystallinity could be achieved by adjusting the deposition temperature from 660 °C down to 640 °C, as indicated by the intensity of the (1 0 2) reflection in the XRD pattern of Figure 32a. The AFM micrograph in Figure 32b illustrates the presence of grains in the sample, indicating the correspondingly textured microstructure.

Higher deposition temperature could be reached by glueing with silver paste the back side of the substrate to a metallic holder (consisting of a Cr-Co-Ni alloy, 0.5 cm thickness) in contact with the heater. After application, the silver paste was dryedin air at room temperature for one hour and subsequently for one hour at 200 °C. This allowed for the growth of a polycrystalline layer on MgO (1 0 0), at 680 °C and 0.01 mbar of oxygen pressure as shown in Figure 33, and also the growth of thin film with good cristallinity at 750 °C, 0.1 mbar oxygen pressure (Figure 34a). Interestingly, a further increase of the pressure up to 0.5 mbar led to the appearance of peaks corresponding to the {0 0 2} reflections (Figure 34b).

TEM analysis of a thin film with a thickness of 8.5 nm grown on Al_2O_3 (0 0 0 1) (1.5 J/cm^2, 2 Hz, 800 °C, 0.5 mbar) revealed the presence of an amourphous phase both near the interface and near the surface: The central crystalline region is estimated to be around 7 nm thick (Figure 35).

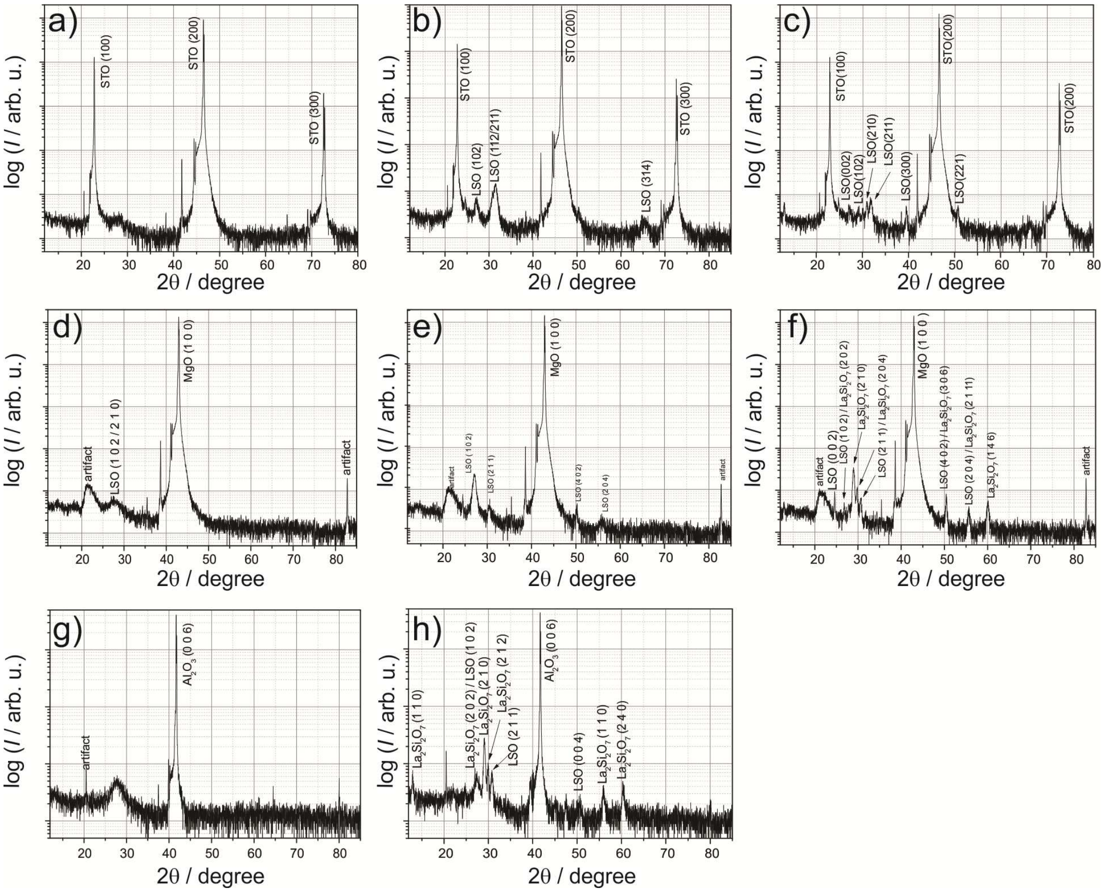

Figure 30: XRD patterns of LSO thin films deposited on different substrates. Growth parameters: laser fluence 1.5 J/cm^2, temperature on the substrate 660 °C, 10000 pulses, 5 Hz, 0.01 mbar O_2, annealing in 1 bar O_2, 660 °, 30 min.

On STO (1 1 0): a) as deposited, b) after heating treatment in air 900 °C – 1 h, c) after heating treatment in air 900 °C – 10h

On MgO (1 0 0): d) as deposited, e) after heating treatment in air 900 °C – 1 h, f) after heating treatment in air 900 °C – 10h

On Al_2O_3 (0 0 0 1): g) as deposited, h) after heating treatment in air 900 °C – 10 h

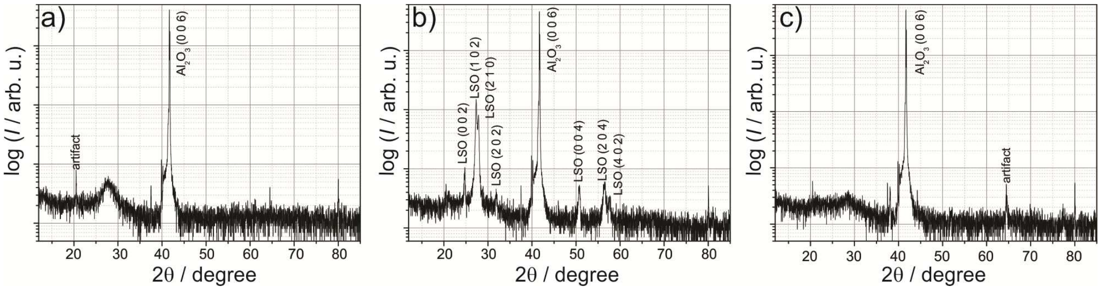

Figure 31: XRD pattern of LSO thin films grown on Al_2O_3 with different pulse frequency. a) 5 Hz, b) 2 Hz, c) 1 Hz
Growth parameter: laser fluence 1.5 J/cm^2, temperature on the substrate 660 °C, 10000 pulses, 0.01 mbar O_2, annealing in 1 bar O_2, 660 °, 30 min.

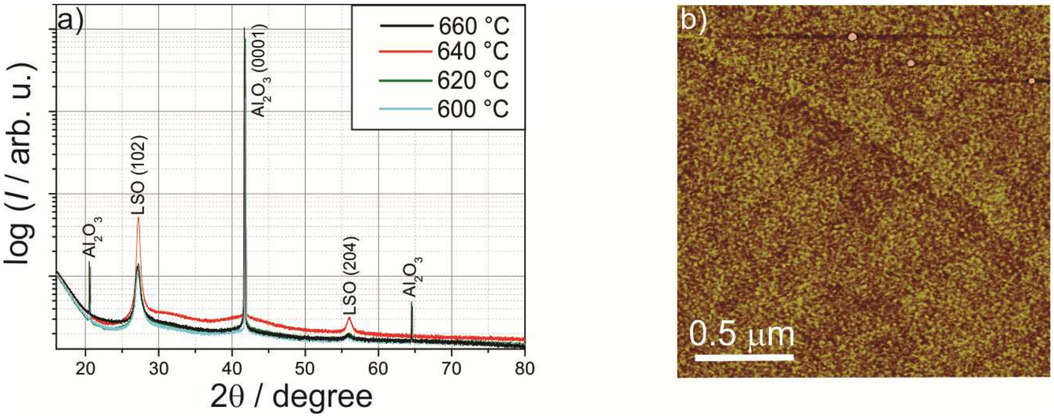

Figure 32: a) XRD pattern of LSO thin films deposited at different temperatures. b) AFM micrograph of a thin film deposited at 640 °C, RMS: 0.270 nm. Growth parameter: laser fluence 1.5 J/cm^2, 2Hz, 2500 pulses, 0.1 mbar O_2, annealing in 1 bar O_2 at deposition temperature, 30 min.

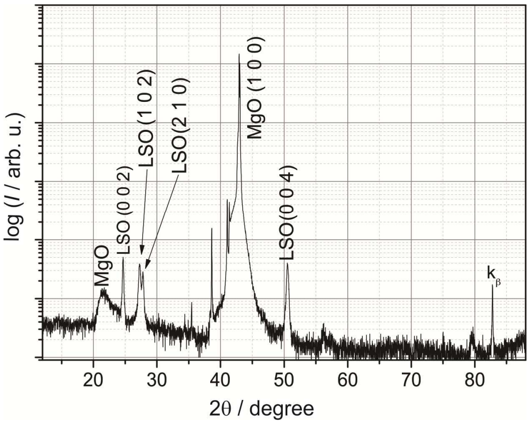

Figure 33: XRD pattern of LSO thin films grown on MgO (1 0 0).
Growth parameter: laser fluence 1.5 J/cm^2, 2 Hz, temperature on the substrate 680 ºC, 10000 pulses, 0.01 mbar, annealing in 1 bar O_2 at deposition temperature, 30 min.

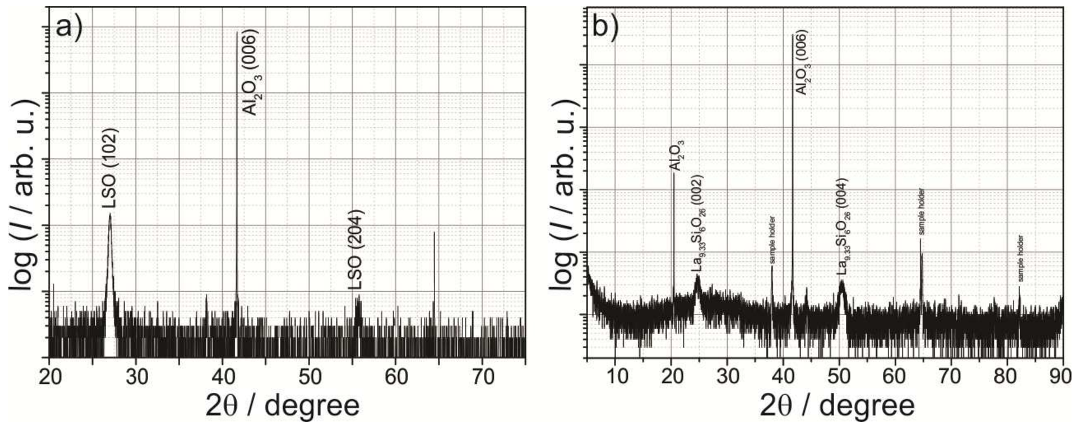

Figure 34: XRD pattern of LSO thin films grown on Al_2O_3 at different deposition pressure a) 0.1 mbar b) 0.5 mbar. Growth parameter: laser fluence 1.5 J/cm^2, temperature on the substrate a) 750 °C, b) 800 °C, 10000 pulses, annealing in 1 bar O_2 at deposition temperature, 30 min.

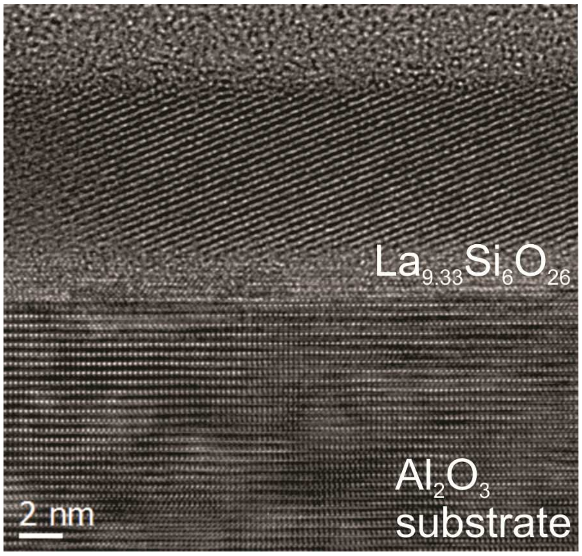

Figure 35: TEM micrograph of a thin film of LSO on Al_2O_3 (0 0 0 1). Crystalline phase is 7 nm thick, while the rest of the sample grows amorphous. Growth parameter: laser fluence 1.5 J/cm^2, 2 Hz, 2500 pulses, 800 °C, 0.5 mbar O_2, annealing in 1 bar O_2, at deposition temperature, 30 min.

6.1.1 Single layers: characterization of the electrical properties

Among the thin films deposited under the different growth conditions described above, only selected thin films have been employed for the characterization of the electrical properties. In particular, the following samples have been analyzed: a polycrystalline thin film with a thickness of 100 nm grown on MgO (1 0 0) (growth conditions: 1.5 J/cm^2, 680 °C, 2 Hz, 0.01 mbar), a textured thin film (8 nm thick) on Al_2O_3 (0 0 0 1) (growth conditions: 1.5 J/cm^2, 640 °C, 2 Hz, 0.1 mbar) and a textured thin film (100 nm thick) on Al_2O_3 (0 0 0 1) (growth conditions: 1.5 J/cm^2, 750 °C, 2 Hz, 0.1 mbar).

The XRD characterization of the layers is reported in Figure 33 and Figure 32a (red line) and Figure 34a. All the samples have been annealed in pure O_2 (1 bar) at deposition temperature.

It is worth noting that the samples grown at high temperature with silver back coating show more than one single contribution in the EIS spectra (beside the electrode contribution), in contrast to what expected from EIS characterization of thin films using this electrode geometry (compare paragraph 3.2.1.2). Presumably silver at high temperature diffuses into the substrate.

Textured thin film grown on Al_2O_3 at 750 °C showed three contributions in the Nyquist plot of the impedance and two in the complex modulus plot (Figure 36 a,b,). While the third contribution can be easily assigned to the electrode (note that owing to its corresponding high capacitance value, 2 10^{-8} F, this contribution disappears in the complex modulus plot), the other two semicircles could be fitted using two RQ circuits in series (Q being the constant phase element), from which for the high frequency contribution a resistance of 6.9 10^8 Ω and capacitance 6.8 10^{-12} F were obtained while for the intermediate frequency contribution a resistance of 1.1 10^7 Ω, and a capacitance of 4.4 10^{-12} F were determined. It is worth noting that due to the very similar capacitance values, these two semicircles are not likely to stem from the bulk and the grain boundary contributions, respectively. Moreover one should note that the samples obtained without using silver paste on the back side of the substrate do not exhibit the appearance of an extra semicircle in the impedance spectra. In order to determine the origin of such impedance behavior, a bare substrate of Al_2O_3 (0 0 0 1) with silver paste back coating was exposed to the same temperature and oxygen pressure for 1 hour and then measured. Also in this case the impedance spectra show two distinct semicircles (Figure 36 c, d).

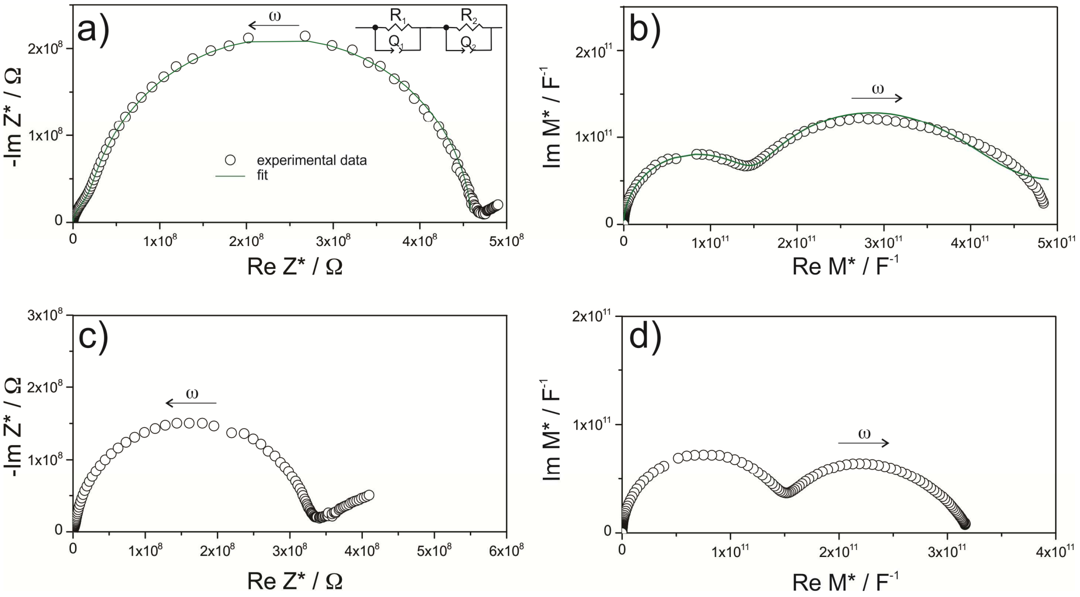

Figure 36: Nyquist plot of a) the impedance and b) the complex modulus of a thin film of $La_{9.33}Si_6O_{26}$ on Al_2O_3 (0 0 0 1) deposited at high temperature and by using silver paste on the back side of the substrate to improve the thermal contact (acquired at 550°C). Experimental data and fit are indicated. For the fitting 2 R - Q elements in series have been used (shown in the inset). c) Nyquist plot of the impedance of a Al_2O_3 (0 0 0 1) substrate with silver paste back coating annealed in oxygen at 750 °C. d) Nyquist plot of the modulus of the same substrate.

Similarly, the spectra of single layer deposited at 680 ºC on MgO (1 1 0) also show a second contribution in the complex modulus plot (see Figure 37 a, b), while in the impedance plot only one distorted semicircle is visible. The distortion of the semicircle is probably due to the overlapped contribution of the electrodes with the one of the film at low frequencies since this contribution disappear in the modulus plot. The two semicircles visible in the modulus plot have similar capacitances ($5\ 10^{12}$ F) and different resistances: at 700 ºC $3\ 10^{7}$ Ω for the semicircle at lower frequency, and $7\ 10^{6}$ Ω for the contribution at high frequency.

Only two contributions appear instead for the single layer on Al_2O_3 deposited at 660 ºC without silver paste back coating. Also in this case the semicircle is distorted because of an overlapped contribution of the electrode at low frequencies with the film contribution (as for the previous samples it disappears on the complex modulus plot). The first part of the impedance arcs at high frequency, up to the maximum values of the imaginary part of Z* has been used for the fitting by using a single RQ circuit.

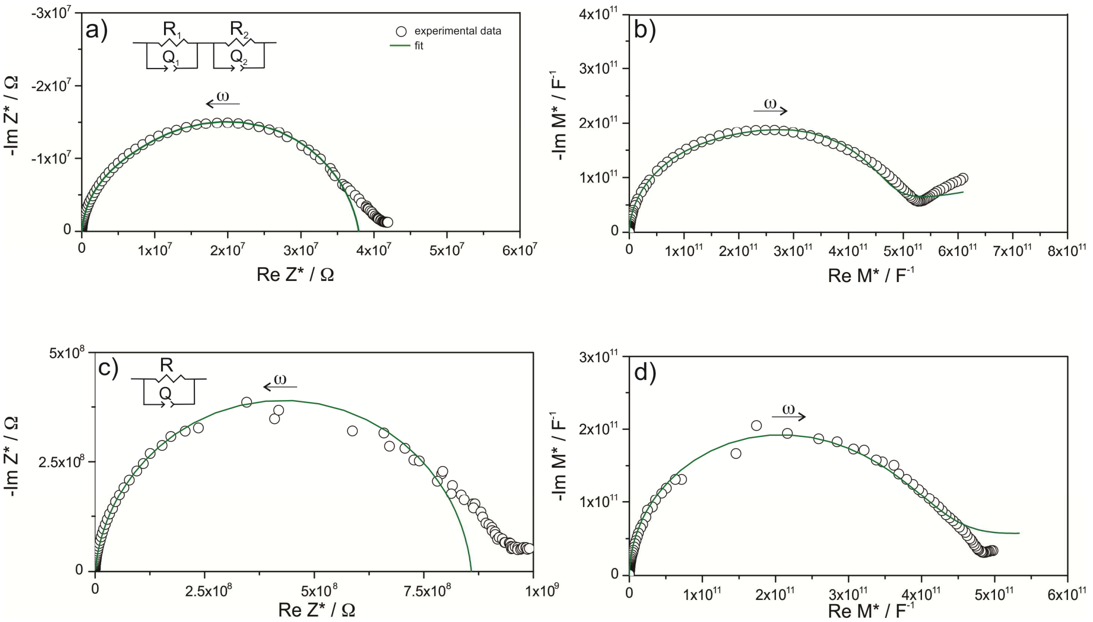

Figure 37: a) Nyquist plot of the impedance of a single layer of $La_{9.33}Si_6O_{26}$ on MgO (1 0 0) (acquired at 700 °C), b) Nyquist plot of the modulus. For the fitting 2 R - Q elements has been used. Nyquist plot of a) the impedance and b) the complex modulus of a thin film of $La_{9.33}Si_6O_{26}$ on Al_2O_3 (0 0 0 1) deposited at 660 °C (acquired at 700°C). Experimental data and simulated spectra are indicated. For the fitting 1 R - Q elements has been used.

The unexpected additional semicircle in the EIS spectra resulting from the silver paste treatment made the estimation of the conductivity not trivial because of the unknown pathway of the current in the various samples. In principle, one can expect to have four different contributions stemming from i) the electrode, ii) the film, iii) the bare substrate and iv) the part of the substrate where the conduction is possibly affected by the silver paste treatment. In this situation, it is not easy to attribute either the conductivity or the resistance or capacitance to the different contributions. Therefore the activation energy is here the only reliable quantity that can be used to compare the ionic transport properties among the different samples. The values of activation energies are summarized in Table 8.

Firstly let us compare the activation energy of the bare substrate of Al_2O_3 (1.07 ± 0.01 eV) with the two different contributions of a substrate annealed with silver back coating: both activation energies are lower than that of the bare substrate, indicating the effect of the silver diffusion on the conduction of the whole substrate. It is however recognizable that the activation energy for the semicircle at high frequencies is substantially lower (E_a2: 0.47 ± 0.03 eV). The second contribution at low frequencies (E_a1: 0.68 ± 0.02 eV) is probably stemming from the upper part of the film where the effect of the silver is minimized.

The thin film deposited on Al_2O_3 (0 0 0 1) (8 nm thick) without silver back coating shows an activation energy of 1.03 ± 0.009 eV. The value is comparable, though, with the slightly higher values reported in literature: for example Brios *et al.* [121] reported an activation energy of 0.75 eV for polycrystalline thin film of $La_{9.33}Si_6O_{26}$, while Tao *et al.* [112] measured a value of 0.90 eV on pellet sintered at 1400 °C for 20 hours. For this sample it is also possible to compare the conductivity with the literature, since it has not been treated with silver paste. In this case, at 600 °C the measured conductivity ($1.24\ 10^{-4}$ S cm^{-1}) is one order of magnitude lower than the one measured by Brios *et al.* ($1\ 10^{-3}$ S cm^{-1}), and 3 times lower compared to the one reported by Tao *et al.* ($3\ 10^{-4}$ S cm^{-1}).

Here we use the values of activation energies obtained on Al_2O_3 substrate with silver back coating and the 8 nm thick $La_{9.33}Si_6O_{26}$ single layer as reference for comparison with the other samples.

For $La_{9.33}Si_6O_{26}$ on Al_2O_3 with silver back coating, two different contributions can be observed; the one at high frequencies has an activation energy of 0.71 ± 0.01 eV and is comparable with the substrate contribution; while for the one at low frequencies the measured value is 0.98 ± 0.004 eV, which suggests that the relative semicircle stems from the thin films. Moreover, as shown in Figure 38a, the first contribution shows a dependence of the conductance on the oxygen partial pressure (slope 0.24 ± 0.02, 1/4), while for the second one no dependence in the same range of oxygen partial pressure has been measured (slope: 0.00 ± 0.01), suggesting an ionic conduction according Eq. 6.1. This also point towards the second semicircle to be attributed to the $La_{9.33}Si_6O_{26}$ film.

Also from the measurement of the single layers (100 nm thick) on MgO two contributions can be observed, one at high frequencies with activation energy of 1.20 ± 0.02 eV and one at low frequencies (R_1-Q_1) with Ea = 1.07 ± 0.008 eV. Up to now we do not have values for the activation energy of the MgO substrate annealed with silver paste. However, the activation energy of a bare substrate of MgO (1 0 0) is comparable with the high frequency contribution (R_1-Q_1) of the single layer. In this case, it is reasonable to interpret the low frequency semicircle as stemming from the $La_{9.33}Si_6O_{26}$ film (1.07 ± 0.008 eV). Also in this case the conductance dependence on the oxygen partial pressure is helpful to assign the two contributions (See Figure 38b). In particular, the conductance corresponding to the low frequency semicircle exhibit practically no dependence on the oxygen partial pressure (the slope in the log(G) vs log(pO_2) plot is +1/16), while for the semicircle at high frequency the slope (+1/6) is substantial. Thus, the oxygen partial pressure dependence measurement allows for the assignment of the high frequency semicircle to the ionic transport in the $La_{9.33}Si_6O_{26}$ film.

Table 8: Activation energies of the different contributions in thin films and substrates of $La_{9.33}Si_6O_{26}$, with and without silver back coating

	E_a / eV
LSO 100 nm on Al_2O_3 (with silver paste) R1-Q1	0.98 ± 0.004
LSO 100 nm on Al_2O_3 (with silver paste) R2-Q2	0.71 ± 0.01
LSO 100 nm on MgO (with silver paste) R1-Q1	1.07 ± 0.008
LSO 100 nm on MgO (with silver paste) R2-Q2	1.20 ± 0.02
LSO 8 nm on Al_2O_3	1.03 ± 0.009
Al_2O_3 substrate	1.07 ± 0.01
MgO substrate	1.16 ± 0.01
Al_2O_3 substrate (with silver paste) R1-Q1	0.68 ± 0.02
Al_2O_3 substrate (with silver paste) R2-Q2	0.47 ± 0.03

Notably, the activation energies stemming from the contribution attributed to the $La_{9.33}Si_6O_{26}$ thin films are generally in agreement with the values reported in the literature (0.75 eV on polycrystalline thin films and 0.90 eV on ceramic pellets). A slight increment can be seen from the thicker films to the thinner (0.1 eV) but it is unfortunately too small to indicate a possible role of the grain boundaries or a possible film – substrate interface effect.

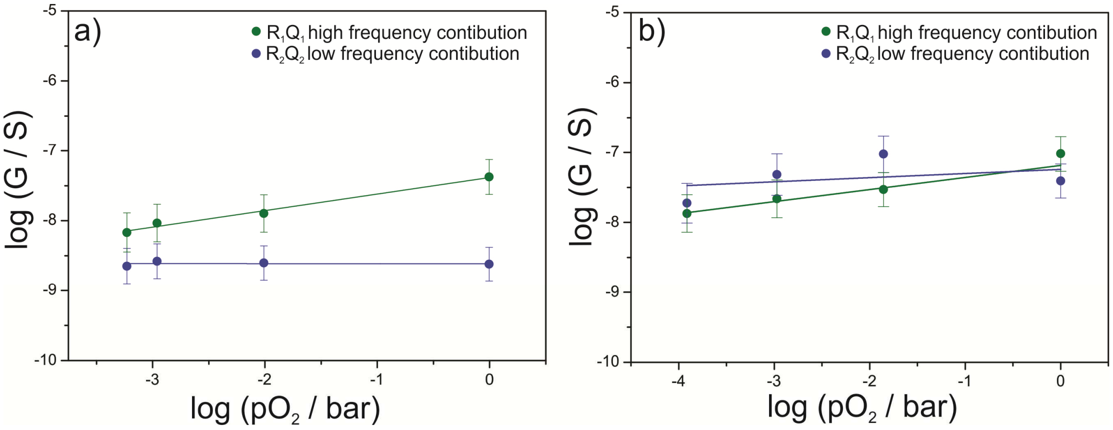

Figure 38: Conductance dependence on the oxygen partial pressure of two contributions in thin films of LSO with silver back coating. a) $La_{9.33}Si_6O_{26}$ 100 nm on Al_2O_3 (0 0 0 1), b) $La_{9.33}Si_6O_{26}$ 100 nm on MgO (1 0 0).

6.1.2 Conclusions

Thin films of $La_{9.33}Si_6O_{26}$ have been successfully deposited *via* PLD method on different substrates. The role of the various deposition parameters has been investigated in the attempt of optimizing the growth of single layers of lanthanum apatite. From this study it has emerged that both the role of the deposition temperature and the laser pulse frequency are the most critical parameters for obtaining high quality films.

In particular textured thin films have been grown on Al_2O_3 (0 0 0 1) with highly oriented grains.

The electrical characterization of textured and polycrystalline single layers was unexpectedly affected by the silver paste back coating, which was used to reach the necessary high deposition temperatures. The presence of residual silver on the back side of the substrates causes the appearance of a second contribution in the EIS spectra. An interpretation of the EIS spectra based on the comparison of the activation energies and oxygen partial pressure dependence of the conductance is proposed.

REFERENCES

[1] C. G. Granqvist, *Transparent conductors as solar energy materials: A panoramic review*, Solar Energy Materials and Solar Cells*,* **91** (17), *1529-1598*, 2007.

[2] F. Q. Huang, C. Y. Yang and D. Y. Wan, *Advanced solar materials for thin-film photovoltaic cells*, Frontiers of Physics*,* **6** (2), *177-196*, 2011.

[3] H. L. Tuller, S. J. Litzelman and W. Jung, *Micro-ionics: next generation power sources*, Physical Chemistry Chemical Physics*,* **11** (17), *3023-3034*, 2009.

[4] J. Santiso and M. Burriel, *Deposition and characterisation of epitaxial oxide thin films for SOFCs*, Journal of Solid State Electrochemistry*,* **15** (5), *985-1006*, 2011.

[5] H. W. van Zeijl, *Thin Film Technologies for Micro/Nano Systems; A Review*, Silicon Compatible Materials, Processes, and Technologies for Advanced Integrated Circuits and Emerging Applications 4*,* **61** (3), *191-206*, 2014.

[6] G. F. Fine, L. M. Cavanagh, A. Afonja and R. Binions, *Metal Oxide Semi-Conductor Gas Sensors in Environmental Monitoring*, Sensors*,* **10** (6), *5469-5502*, 2010.

[7] Y. N. Zhou, M. Z. Xue and Z. W. Fu, *Nanostructured thin film electrodes for lithium storage and all-solid-state thin-film lithium batteries*, Journal of Power Sources*,* **234** *310-332*, 2013.

[8] R. Waser, *Redox-based resistive switching memories*, Journal of Nanoscience and Nanotechnology*,* **12** (10), *7628-7640*, 2012.

[9] D. B. Strukov and H. Kohlstedt, *Resistive switching phenomena in thin films: Materials, devices, and applications*, MRS Bulletin*,* **37** (2), *108-117*, 2012.

[10] M. Kubicek*, et al.*, *Tensile lattice strain accelerates oxygen surface exchange and diffusion in* $La_{1-x}Sr_xCoO_{3-delta}$ *thin films*, Acs Nano*,* **7** (4), *3276-3286*, 2013.

[11] E. Fabbri, D. Pergolesi and E. Traversa, *Ionic conductivity in oxide heterostructures: the role of interfaces*, Science and Technology of Advanced Materials*,* **11** (5), 2010.

[12] C. Peters*, et al.*, *Grain-size effects in YSZ thin-film electrolytes*, Journal of the American Ceramic Society*,* **92** (9), *2017-2024*, 2009.

[13] M. C. Gobel, G. Gregori and J. Maier, *Electronically blocking grain boundaries in donor doped cerium dioxide*, Solid State Ionics*,* **215** *45-51*, 2012.

[14] S. Heiroth*, et al.*, *Yttria-stabilized zirconia thin films by pulsed laser deposition: Microstructural and compositional control*, Journal of the European Ceramic Society*,* **30** (2), *489-495*, 2010.

[15] M. C. Gobel, G. Gregori and J. Maier, *Mixed conductivity in nanocrystalline highly acceptor doped cerium oxide thin films under oxidizing conditions*, Physical Chemistry Chemical Physics*,* **13** (23), *10940-10945*, 2011.

[16] C. Korte, N. Schichtel, D. Hesse and J. Janek, *Influence of interface structure on mass transport in phase boundaries between different ionic materials Experimental studies and formal considerations*, Monatshefte Fur Chemie*,* **140** (9), *1069-1080*, 2009.

[17] J. Hinterberg, T. Zacherle and R. A. De Souza, *Activation volume tensor for oxygen-vacancy migration in strained* CeO_2 *electrolytes*, Physical Review Letters*,* **110** (20), 2013.

[18] N. Schichtel*, et al.*, *On the influence of strain on ion transport: microstructure and ionic conductivity of nanoscale YSZ vertical bar* Sc_2O_3 *multilayers*, Physical Chemistry Chemical Physics*,* **12** (43), *14596-14608*, 2010.

[19] A. P. C. Korte, J. Janek, D. Hesse and N. Zakharovb, *Ionic conductivity and activation energy for oxygen ion transport in superlattices—the semicoherent multilayer system YSZ (*ZrO_2 *+ 9.5 mol%* Y_2O_3*)/*Y_2O_3, Physical Chemistry Chemical Physics*,* **10** (31), *4623-4635*, 2008.

[20] A. Kushima and B. Yildiz, *Oxygen ion diffusivity in strained yttria stabilized zirconia: where is the fastest strain?*, Journal of Materials Chemistry*,* **20** (23), *4809-4819*, 2010.

[21] B. Li*, et al.*, *Multilayered YSZ/GZO films with greatly enhanced ionic conduction for low temperature solid oxide fuel cells*, Physical Chemistry Chemical Physics*,* **15** (4), *1296-1301*, 2013.

[22] J. Keppner*, et al.*, *XRD analysis of strain states in epitaxial YSZ/RE$_2$O$_3$ (RE = Y, Er) multilayers as a function of layer thickness*, Solid State Ionics*,* **273** *2-7*, 2015.

[23] B. Yildiz, *"Stretching" the energy landscape of oxides—Effects on electrocatalysis and diffusion*, MRS Bulletin*,* **39** (2), *147-156*, 2014.

[24] D. Pergolesi*, et al.*, *Tensile Lattice Distortion Does Not Affect Oxygen Transport in Yttria-Stabilized Zirconia-CeO$_2$ Heterointerfaces*, Acs Nano*,* **6** (12), *10524-10534*, 2012.

[25] W. D. Shen and J. L. Hertz, *Ionic conductivity of YSZ/CZO multilayers with variable lattice mismatch*, Journal of Materials Chemistry A*,* **3** (5), *2378-2386*, 2015.

[26] D. Marrocchelli, L. X. Sun and B. Yildiz, *Dislocations in SrTiO$_3$: Easy To Reduce but Not so Fast for Oxygen Transport*, Journal of the American Chemical Society*,* **137** (14), *4735-4748*, 2015.

[27] V. Metlenko*, et al.*, *Do dislocations act as atomic autobahns for oxygen in the perovskite oxide SrTiO$_3$?*, Nanoscale*,* **6** (21), *12864-12876*, 2014.

[28] K. Otsuka*, et al.*, *Dislocation-enhanced ionic conductivity of yttria-stabilized zirconia*, Applied Physics Letters*,* **82** (6), *877-879*, 2003.

[29] M. Sillassen*, et al.*, *Low-temperature superionic conductivity in strained yttria-stabilized zirconia*, Advanced Functional Materials*,* **20** (13), *2071-2076*, 2010.

[30] K. Otsuka*, et al.*, *Effects of dislocations on the oxygen ionic conduction in yttria stabilized zirconia*, Materials Transactions*,* **45** (7), *2042-2047*, 2004.

[31] L. Chen*, et al.*, *Electrical properties of a highly oriented, textured thin film of the ionic conductor Gd : CeO$_{2-\delta}$ on (001) MgO*, Applied Physics Letters*,* **83** (23), *4737-4739*, 2003.

[32] L. X. Sun, D. Marrocchelli and B. Yildiz, *Edge dislocation slows down oxide ion diffusion in doped CeO$_2$ by segregation of charged defects*, Nature Communications*,* **6** *6294 6291-6210*, 2015.

[33] S. Azad*, et al.*, *Nanoscale effects on ion conductance of layer-by-layer structures of gadolinia-doped ceria and zirconia*, Applied Physics Letters*,* **86** (13, 131906), *1-3*, 2005.

[34] K. Sangtae, J. Fleig and J. Maier, *Space charge conduction: simple analytical solutions for ionic and mixed conductors and application to nanocrystalline ceria*, Physical Chemistry Chemical Physics*,* **5** (11), *2268-2273*, 2003.

[35] J. Maier, *Nanoionics: ionic charge carriers in small systems*, Physical Chemistry Chemical Physics*,* **11** (17), *3011-3022*, 2009.

[36] J. Maier, *Nanoionics: ion transport and electrochemical storage in confined systems*, Nature Materials*,* **4** (11), *805-815*, 2005.

[37] N. Sata, K. Eberman, K. Eberl and J. Maier, *Mesoscopic fast ion conduction in nanometre-scale planar heterostructures*, Nature*,* **408** (6815), *946-949*, 2000.

[38] X. Guo and J. Maier, *Ionically conducting two-dimensional heterostructures*, Adv. Mater.*,***- 21** (25-26), *2631*, 2009.

[39] K. K. Adepalli, M. Kelsch, R. Merkle and J. Maier, *Influence of line defects on the electrical properties of single crystal* TiO_2, Advanced Functional Materials*,* **23** (14), *1798-1806*, 2013.

[40] S. Kepeng*, et al.*, *Cerium reduction at the interface between ceria and yttria-stabilised zirconia and implications for interfacial oxygen non-stoichiometry*, APL Materials*,* **2** (3, 032104), 2014.

[41] W. R. Panero, L. Stixrude and R. C. Ewing, *First-principles calculation of defect-formation energies in the* $Y_2(Ti,Sn,Zr)_2O_7$ *pyrochlore*, Physical Review B*,* **70** (5), 2004.

[42] C. R. Stanek, L. Minervini and R. W. Grimes, *Nonstoichiometry in* $A_2B_2O_7$ *pyrochlores*, Journal of the American Ceramic Society*,* **85** (11), *2792-2798*, 2002.

[43] L. Minervini, R. W. Grimes and K. E. Sickafus, *Disorder in Pyrochlore Oxides*, J. Am. Ceram. Soc.*,* **83** (8), *1873 - 1878*, 2000.

[44] M. Pirzada*, et al.*, *Oxygen migration in* $A_2B_2O_7$ *pyrochlores*, Solid State Ionics*,* **140** (3-4), *201-208*, 2001.

[45] T. Hagiwara, H. Yamamura and H. Nishino, *Relationship Between Oxide-Ion Conductivity and Ordering of Oxygen Vacancy in the* $Ln_2Zr_2O_7$ *(Ln = La, Nd, Eu) System Using High Temperature XRD*, Journal of Fuel Cell Science and Technology*,* **8** (5, 051020), *1-5*, 2011.

[46] H. Yamamura, H. Nishino, K. Kakinuma and K. Nomura, *Electrical conductivity anomaly around fluorite-pyrochlore phase boundary*, Solid State Ionics*,* **158** (3), *359-365*, 2003.

[47] A. J. Burggraaf, T. van Dijk and M. J. Verkerk, *Structure and conductivity of pyrochlore and fluorite type solid solutions*, Solid State Ionics*,* **5** *519-522*, 1981.

[48] P. J. Wilde and C. R. A. Catlow, *Defects and diffusion in pyrochlore structured oxides*, Solid State Ionics*,* **112** (3-4), *173-183*, 1998.

[49] B. J. Wuensch*, et al.*, *Connection between oxygen-ion conductivity of pyrochlore fuel-cell materials and structural change with composition and temperature*, Solid State Ionics*,* **129** (1), *111- 133*, 2000.

[50] C. Kittel, *Introduction to solid state physics, 8th Edition*, John Wiley & Sons, Inc.*,* 2004.

[51] M. J., *Physical chemistry of ionic materials - John Wiley & Sons, Inc.*, 2004.

[52] C. T. Chen, S. Sen and S. Kim, *Effective concentration of mobile oxygen-vacancies inheavily doped cubic zirconia: results from combined electrochemical impedance and NMR spectroscopies*, Chemistry of Materials*,* **24** (18), *3604-3609*, 2012.

[53] F. A. Kroger and H. J. Vink, *Relations between the concentrations of imperfections in crystalline solids*, Solid State Physics-Advances in Research and Applications*,* **3** *307-435*, 1956.

[54] K. Sasaki and J. Maier, *Re-analysis of defect equilibria and transport parameters in* Y_2O_3*-stabilized* ZrO_2 *using EPR and optical relaxation*, Solid State Ionics*,* **134** (3), *303-321*, 2000.

[55] N. G. Carter B., *Ceramic materials: science and engineering - Springer Science and Buisness Editor*, 2007.

[56] S. Ikeda*, et al.*, *Electrical conductivity of yttria-stabilized zirconia single crystals*, Journal of Materials Science*,* **20** (12), *4593-4600*, 1985.

[57] F. Hanic, M. Hartmanova, F. Kundracik and E. E. Lomonova, *Stabilization and properties of high temperature forms of zirconia*, Diffusion and Defect Data Part B (Solid State Phenomena)*,* **90-91** *303-308*, 2003.

[58] H. L. Tuller, *Mixed conduction in nonstoichiometric oxides - Ed. O. Toft Søresen - Academic Press*, 1981.

[59] J. Maier, *Ionic-conduction in space charge regions*, Progress in Solid State Chemistry*,* **23** (3), *171-263*, 1995.

[60] J. Maier, *Space -charge regions in solid 2 phase system and their conduction contribution 2.contact equilibrium at the interface of 2 ionic conductors and the related conductivity effect*, Berichte Der Bunsen-Gesellschaft-Physical Chemistry Chemical Physics*,* **89** (4), *355-362*, 1985.

[61] J. Maier, *On the conductivity of polycrystalline materials*, Berichte Der Bunsen-Gesellschaft-Physical Chemistry Chemical Physics*,* **90** (1), *26-33*, 1986.

[62] X. Guo and J. Maier, *Ionically conducting two-dimensional heterostructures*, Adv. Mater.*,* **21** (25-26), *2619-2631*, 2009.

[63] M. F. Doerner and W. D. Nix, *Stresses and deformation processes in thin-films on substrates*, Crc Critical Reviews in Solid State and Materials Sciences, **14** (3), *225-268*, 1988.

[64] C. Korte, *et al.*, *Coherency strain and its effect on ionic conductivity and diffusion in solid electrolytes - an improved model for nanocrystalline thin films and a review of experimental data*, Physical Chemistry Chemical Physics, **16** (44), *24575-24591*, 2014.

[65] J. Q. He, *et al.*, *Microstructure and possible strain relaxation mechanisms of* $La_2CuO_{4+\delta}$ *thin films grown on* $LaSrAlO_4$ *and* $SrTiO_3$ *substrates* Journal of Applied Physics, **101** (7), 2007.

[66] H. K. G. Chrisey B. D., *Pulsed Laser Deposition of Thin Film - John Wiley and Sons Ed.*, 1994.

[67] J. B. W. Macdonald R. J., *Impedance spectroscopy, Second Edition - Edited by John Wiley and Sons, Inc.*, 2005.

[68] I. M. Hodge, M. D. Ingram and A. R. West, *Impedance and modulus spectroscopy of polycrystalline solid electrolytes*, Journal of Electroanalytical Chemistry, **74** (2), *125-143*, 1976.

[69] I. M. Hodge, M. D. Ingram and A. R. West, *New method for analyzing AC behavior of polycrystalline solid electrolytes*, Journal of Electroanalytical Chemistry, **58** (2), *429-432*, 1975.

[70] T. Vandijk and A. J. Burggraaf, *Grain-boundary effects on ionic-conductivity in ceramic* $GdXZr_{1-X}O_{2-(X-2)}$ *solid-solutions*, Physica Status Solidi a-Applied Research, **63** (1), *229-240*, 1981.

[71] M. J. Verkerk, B. J. Middelhuis and A. J. Burggraaf, *Effect of grain-boundaries on the conductivity of high-purity* ZrO_2-Y_2O_3 *ceramics*, Solid State Ionics, **6** (2), *159-170*, 1982.

[72] J. Fleig and J. Maier, *The impedance of ceramics with highly resistive grain boundaries: Validity and limits of the brick layer model*, Journal of the European Ceramic Society, **19** (6), *693-696*, 1999.

[73] X. Guo and J. Maier, *Grain boundary blocking effect in zirconia: A Schottky barrier analysis*, Journal of the Electrochemical Society, **148** (3), *E121-E126*, 2001.

[74] S. Kim and J. Maier, *On the conductivity mechanism of nanocrystalline ceria*, Journal of the Electrochemical Society, **149** (10), *J73-J83*, 2002.

[75] X. Guo and R. Waser, *Electrical properties of the grain boundaries of oxygen ion conductors: Acceptor-doped zirconia and ceria*, Progress In Materials Science, **51** (2), *151-210*, 2006.

[76] M. Gerstl, *et al.*, *The grain and grain boundary impedance of sol-gel prepared thin layers of yttria stabilized zirconia (YSZ)*, Solid State Ionics, **225** *732-736*, 2012.

[77] M. C. Gobel, G. Gregori, X. X. Guo and J. Maier, *Boundary effects on the electrical conductivity of pure and doped cerium oxide thin films*, Physical Chemistry Chemical Physics, **12** (42), *14351-14361*, 2010.

[78] H. Galinski, *et al.*, *Agglomeration of Pt thin films on dielectric substrates*, Physical Review B, **82** (23), 2010.

[79] H. Galinski, *et al.*, *Hillock formation of Pt thin films on single-crystal yttria-stabilized zirconia*, Physical Review B, **85** (12, 125408), 2012.

[80] Q. F. a. P. A. R. M. Raposo, *Modern Research and Educational Topics in Microscopy - Eds. A. Méndez-Vilas and J. Díaz - Editors*, 2007.

[81] D. M. Mattox, *Hanbook of physical vapor deposition PVD processing - Noyes Publication*, 1998.

[82] D. A. C. A. R.R.L. De Oliveira, T.G.S. Cruz, F.M. Yamaji, F.L. Leite, *Measurement of the nanoscale roughness by atomic force microscopy: basic principles and applications - Intech Ed.*, 2010.

[83] ICPDS - International comittee for diffraction data,

[84] K. Shimamura, T. Arima, K. Idemitsu and Y. Inagaki, *Thermophysical properties of rare-earth-stabilized zirconia and zirconate pyrochlores as surrogates for actinide-doped zirconia*, International Journal of Thermophysics, **28** (3), *1074-1084*, 2007.

[85] C. Heremans, B. J. Wuensch, J. K. Stalick and E. Prince, *Fast-ion conducting* $Y_2(ZrYTi_{1-y})_2O_7$ *pyrochlores - neutron Rietvield analysis of disordered-induced by Zr substitution*, Journal of Solid State Chemistry, **117** (1), *108-121*, 1995.

[86] Z. G. Liu, J. H. Ouyang, K. N. Sun and Y. Zhou, *Electrical properties of the* $GdSmZr_2O_7$ *ceramic under different sintering conditions*, Journal Of Power Sources, **210** *96-100*, 2012.

[87] M. V. F. Schlupp, *et al.*, *Influence of microstructure on the cross-plane oxygen ion conductivity of yttria stabilized zirconia thin films*, Physica Status Solidi a-Applications and Materials Science, **209** (8), *1414-1422*, 2012.

[88] E. T. K. Graeme W. Watson, Nora H. de Leeuw, Duncan J. Harris and and S. C. Parker, *Atomistic simulation of dislocations, surfaces and interfaces in MgO*, Faraday Transactions, **92** (3), *433- 438*, 1996.

[89] G. F., *Mechanical stress on the nanoscale: Simulation, material System and characterization techniques. Chapter 1: Fundamental of stress and strain on the nanoscale*, M. Hanbücken, P. Müller and R. B. Wehrspohn, 2011.

[90] D. J. Srolovitz, *On the stability of surfaces of stressed solids*, Acta Metallurgica, **37** (2), *621-625*, 1989.

[91] S. Ostanin, *et al.*, *Effect of relaxation on the oxygen K-edge electron energy-loss near-edge structure in yttria-stabilized zirconia*, Physical Review B, **62** (22), *14728-14735*, 2000.

[92] I. M. Ross, *et al.*, *Electron energy-loss spectroscopy (EELS) studies of an yttria stabilized TZP ceramic*, Journal of the European Ceramic Society, **24** (7), *2023-2029*, 2004.

[93] D. Vlachos, A. J. Craven and D. W. McComb, *The influence of dopant concentration on the oxygen K-edge ELNES and XANES in yttria-stabilized zirconia*, Journal of Physics-Condensed Matter, **13** (48), *10799-10809*, 2001.

[94] T. Ryll, *et al.*, *Microscopic and nanoscopic three-phase-boundaries of platinum thin-film electrodes on YSZ electrolyte*, Advanced Functional Materials, **21** (3), *565-572*, 2011.

[95] D. J. Srolovitz and M. G. Goldiner, *The thermodynamics and kinetics of film agglomeration*, **47** (3), 1995.

[96] J. Fleig, F. Noll and J. Maier, *Surface conductivity measurements on AgCl single crystals using microelectrodes*, Berichte Der Bunsen-Gesellschaft-Physical Chemistry Chemical Physics, **100** (5), *607-615*, 1996.

[97] X. X. Guo, *et al.*, *Annealing effect on ion conduction of nanosized CaF_2/BaF_2 multilayers*, Journal of Applied Physics, **105** (11), 2009.

[98] D. W. McComb, *Bonding and electronic structure in zirconia pseudopolymorphs investigated by electron energy-loss spectroscopy*, Physical Review B, **54** (10), *7094-7102*, 1996.

[99] R. A. De Souza, V. Metlenko, D. Park and T. E. Weirich, *Behavior of oxygen vacancies in single-crystal $SrTiO_3$: Equilibrium distribution and diffusion kinetics*, Physical Review B, **85** (17, 174109), 2012.

[100] F. W. Zhang, A. M. Walker, K. Wright and J. D. Gale, *Defects and dislocations in MgO: atomic scale models of impurity segregation and fast pipe diffusion*, Journal of Materials Chemistry, **20** (46), *10445-10451*, 2010.

[101] J. A.Kilner and B. C.Steel, *Non stoichiometric oxides*, 1981.

[102] J. T. S. Irvine, I. R. Gibson and D. P. Fagg, *Oxide ion transport in highly defective cubic stabilized zirconias*, Ionics, **1** (4), *279-285*, 1995.

[103] C. T. Chen, S. Sen and S. Kim, *Effective concentration of mobile oxygen-vacancies in heavily doped cubic zirconia: results from combined electrochemical impedance and NMR spectroscopies*, Chemistry of Materials, **24** (18), *3604-3609*, 2012.

[104] N. Schichtel, C. Korte, D. Hesse and J. Janek, *Elastic strain at interfaces and its influence on ionic conductivity in nanoscaled solid electrolyte thin films-theoretical considerations and experimental studies*, Physical Chemistry Chemical Physics, **11** (17), *3043-3048*, 2009.

[105] S. Sanna*, et al.*, *Enhancement of ionic conductivity in Sm-doped ceria/yttria-stabilized zirconia heteroepitaxial structures*, Small, **6** (17), *1863-1867*, 2010.

[106] M. M. Hall, V. G. Veeraraghavan, H. Rubin and P. G. Winchell, *Approximation of symmetric X-ray peaks by Pearson type-7 distribution*, Journal of Applied Crystallography, **10** (1), *66-68*, 1977.

[107] J. H. Joo and G. M. Choi, *Electrical conductivity of YSZ film grown by pulsed laser deposition*, **177** (11), *1053-1057*, 2006.

[108] E. Bechade*, et al.*, *Synthesis of lanthanum silicate oxyapatite materials as a solid oxide fuel cell electrolyte*, Journal Of The European Ceramic Society, **28** (14), *2717-2724*, 2008.

[109] H. Yoshioka and S. Tanase, *Magnesium doped lanthanum silicate with apatite-type structure as an electrolyte for intermediate temperature solid oxide fuel cells*, **176** (31), *2395-2398*, 2005.

[110] L. Malavasi, C. A. J. Fisher and M. S. Islam, *Oxide-ion and proton conducting electrolyte materials for clean energy applications: structural and mechanistic features*, Chemical Society Reviews, **39** (11), *4370-4387*, 2010.

[111] H. Yoshioka, *Enhancement of ionic conductivity of apatite-type lanthanum silicates doped with cations*, Journal of the American Ceramic Society, **90** (10), *3099-3105*, 2007.

[112] S. Tao and J. T. S. Irvine, *Preparation and characterisation of apatite-type lanthanum silicates by a sol-gel process*, Materials Research Bulletin, **36** (78), *1245-1258*, 2001.

[113] A. L. Shaula, V. V. Kharton and F. M. B. Marques, *Oxygen ionic and electronic transport in apatite-type* $La_{10-x}(Si,Al)_6O_{26\pm\delta}$, Journal Of Solid State Chemistry, **178** (6), *2050-2061*, 2005.

[114] A. Mineshige, *et al.*, *Electrical properties of* $La_{10}Si_6O_{27}$*-based oxides*, **179** (21–26), *1009-1012*, 2008.

[115] J. McFarlane, *et al.*, *Synthesis and Conductivities of the Apatite-type Systems,* $La_{9.33+x}Si_{6-y}M_yO_{26+z}$ *(M = Co, Fe, Mn) and* $La_8Mn_2Si_6O_{26}$, Ionics, **8** (1-2), *149-154*, 2002.

[116] M. Y. Gorshkov, A. D. Neuimin, N. M. Bogdanovich and D. I. Bronin, *Electroconductivity and transport numbers of solid electrolytes* $La_{10-x}Ca_xA_6O_{27-}$ *and* $La_{9.33+\delta}A_{6-x}Al_xO_{26}$ *(A = Si, Ge) with apatite-like structure*, Russian Journal of Electrochemistry, **42** (7), *737-743*, 2006.

[117] A. Chesnaud, *et al.*, *Influence of synthesis route and composition on electrical properties of* $La_{9.33+x}Si_6O_{26+3x/2}$ *oxy-apatite compounds*, Solid State Ionics, **179** (33), *1929-1939*, 2008.

[118] S. Nakayama and M. Highchi, *Electrical properties of apatite-type oxide ionic conductors* $RE_{9.33}(SiO_4)_6O_2$ *(RE = Pr, Nd and Sm) single crystals*, Journal of Materials Science Letters, **20** (10), *913-915*, 2001.

[119] J. E. H. Sansom, D. Richings and P. R. Slater, *A powder neutron diffraction study of the oxide-ion-conducting apatite-type phases,* $La_{9.33}Si_6O_{26}$ *and* $La_8Sr_2Si_6O_{26}$, Solid State Ionics, **139** (3-4), *205-210*, 2001.

[120] J. R. Tolchard, M. S. Islam and P. R. Slater, *Defect chemistry and oxygen ion migration in the apatite-type materials* $La_{9.33}Si_6O_{26}$ *and* $La_8Sr_2Si_6O_{26}$, Journal Of Materials Chemistry, **13** (8), *1956-1961*, 2003.

[121] P. Briois, *et al.*, *Synthesis and characterization of apatite structure sputter deposited coatings dedicated to intermediate temperature solid oxide fuel cells*, Journal Of The Electrochemical Society, **158** (12), *B1479-B1484*, 2011.

[122] A. Karthikeyan, M. Tsuchiya and S. Ramanathan, *Apatite-phase synthesis from interdiffusion in doped* CeO_2*-*SiO_2 *thin-film superlattices and in situ conductivity studies*, Electrochemical and Solid State Letters, **11** (11), *K101-K103*, 2008.

[123] H. M. Christen and G. Eres, *Recent advances in pulsed-laser deposition of complex oxides*, Journal of Physics-Condensed Matter, **20** (26), 2008.

[124] M. S. Islam, J. R. Tolchard and P. R. Slater, *An apatite for fast oxide ion conduction*, Chemical Communications, (13), *1486-1487*, 2003.

[125] V. A. Sadykov*, et al.*, *Studies of oxygen transport mechanism in electrolytes based on doped lanthanum silicate with apatite structure using techniques of oxygen isotopic heteroexchange and impedance spectroscopy*, **47** (4), *427-441*, 2011.

[126] P. J. Panteix*, et al.*, *Influence of anionic vacancies on the ionic conductivity of silicated rare earth apatites*, Materials Research Bulletin*,* **43** (5), *1223-1231*, 2008.

[127] J. R. Tolchard and P. R. Slater, *A high temperature powder neutron diffraction structural study of the apatite-type oxide ion conductor,* $La_{9.67}Si_6O_{26.5}$, Journal of Physics and Chemistry of Solids*,* **69** (10), *2433-2439*, 2008.

[128] E. Bechade*, et al.*, *Diffusion path and conduction mechanism of oxide ions in apatite-type lanthanum silicates*, Chemistry of Materials*,* **21** (12), *2508-2517*, 2009.

[129] P. R. Slater and J. E. H. Sansam, *The synthesis and characterisation of new apatite-type oxide ion conductors*, Solid state phenomena*,* **90-91** *195-200*, 2003.

[130] A. Jones, P. R. Slater and M. S. Islam, *Local defect structures and ion transport mechanisms in the oxygen-excess apatite* $La_{9.67}(SiO_4)_6O_{2.5}$, Chemistry of Materials*,* **20** (15), *5055-5060*, 2008.

[131] K. Fukuda*, et al.*, *Anisotropy of oxide-ion conduction in apatite-type lanthanum silicate*, Solid State Ionics*,* **217** *40-45*, 2012.

[132] Y. Kim*, et al.*, *Oxide ion conduction anisotropy deconvoluted in polycrystalline apatite-type lanthanum silicates*, Journal Of Materials Chemistry*,* **21** (9), *2940-2949*, 201

LIST OF MOST USED ABBREVIATION AND SYMBOLS

List of Abbreviations

CPE	Constant phase element
EIS	Electrochemical impedance spectroscopy
Eq.	Equation
Fig.	Figure
GB	Grain boundaries
HR – TEM	High resolution electron microscopy
ICP-OES	Ion coupled plasma – optical emission spectroscopy
PLD	Pulsed laser deposition
RC	Element resistor and capacitance connected in parallel
SOFC	Solid oxide fuel cell
TEM	Transmission electron microscopy
XRD	X – ray diffraction
YSZ	Yttria stabilized zirconia

List of Symbols

a	Lattice constant
A	Cross section area
a_{film}	Film lattice constant
a_h	Holes activity
$a_{substrate}$	Substrate lattice constant
$a_{V_O^{\bullet\bullet}}$	Oxygen vacancies activity
b	Burger vector
C	Capacitance
C_{bulk}	Bulk capacity
C_{el}	Capacitance of the electrodes
C_{stray}	Stray capacitance of a measurment cell
$C_{substrate}$	Capacitance of the substrate
C_{wiring}	Capacitance of the wires and mesurment cell
C_{GB}	Grain boundaries capacity
$c_{dop,\infty}$	Dopant bulk concentration
c_j	Concentration of an arbitrary charge carrier j
$c_{j,\infty}$	Bulk concentration of an arbitrary charge carrier j
$c_{maj,\infty}$	Bulk concentration of the enriched charge carrier j in the Gouy - Chapmann case
d_g	Grain size
ΔG_B^0	Standard Gibbs energy of the band-band transfer reaction

ΔG_{ox}^{0}	Standard Gibbs energy of the oxidation reaction
ΔG_{red}^{0}	Standard Gibbs energy of the reduction reaction
ΔG_{S}^{0}	Standard Gibbs energy of the Schottky reaction
ΔG_{F}^{0}	Standard Gibbs energy of the Frenkel reaction
ΔH_{As}	Association enthalpy
$\Delta\phi$	Space charge potential
Δy	Distance between electrodes
Δz	Length of the electrode
$\Delta Y^{\parallel}$	Interface sheet conductance
$e^{/}$	Electrons according to Kroeger Vink notation
e	Electron charge, 1.602 10^{-19} C
$E_{a,0}$	Activation energy
$f_{V_{O}^{\bullet\bullet}}$	Oxygen vacancies fugacity
F	Faraday constant 96485 C mol^{-1}
f	Lattice mismatch
$G^{\parallel}$	Conductance parallel to the interface
$h^{\bullet}$	Holes according to Kroeger Vink notation
H_m	Migration enthalpy
$I(t)$	Alternate current
i	Imaginary number $(\sqrt{-1})$
I_0	Alternate current at time t=0
k	Boltzmann constant, 1.381 10_{-23} J K^{-1}
$\bar{K}$	Equilibrium constant at high defects concentration

K^0	Pre exponential factor
K_B	Equilibrium constant of the band-band tranfer reaction
K_F	Equilibrium constant of the Frenkel reaction
K_{ox}	Equilibrium constant of the oxidation reaction
K_{red}	Equilibrium constant of the reduction reaction
K_S	Equilibrium constant of the Schottky reaction
L	Thickness of the film
$u_{V_{\ddot{O}}}$	Oxygen vacancies mobility
n	Electron concentration
p	Hole concentration
Q	Constant phase element
R	Resistance
R_{bulk}	Bulk resistance
R_{el}	Electrodes resistance
R_{GB}	Grain boundaries resitance
$R_{multilayer}$	Total resistance of a multilayer
R_q	Root Mean Square as defined in Eq. 3.6
$R_{substrate}$	Substrate resistance
R_{wiring}	Resistance of the wires and measurment cell
R_{YSZ}	Resistance of the phase ysz
$R_{Y_2Zr_2O_7}$	Resistance of the phase $Y_2Zr_2O_7$
t	Time
T	Absolute temperature

$U(t)$	Alternate voltage
U_0	Alternate voltage at time t=0
$V_O^{\bullet\bullet}$	Oxygen vacancies according to Kroeger Vink notation
$V_{Zr}^{////}$	Zirconium vacancies according to Kroeger Vink notation
$Y^{\|}$	Sheet conductance
$Y^{\|}_{\infty}$	Bulk sheet conductance
$Y_{Zr}^{/}$	Yttrium substitutional on Zr lattice position according to Kroeger - Vink notation
Z^*	Impedance
$Z^{/}$	Real part of the Impedance
$Z^{//}$	Imaginary part of the Impedance
z_{dop}	Charge of an arbitrary j charge carrier
z_{maj}	Charge number of the enriched charge carrier j in the Gouy - Chapmann case
$Zr_i^{\bullet\bullet\bullet\bullet}$	Interstial zirconium according to Kroeger Vink notation
α	Fitting parameter for the impedance spectra
ε_{bulk}	Bulk relative permittivity
ε_{GB}	Grain boundaries relative permittivity
$\lambda_{\text{Cu-K}_\alpha}$	Wavelength of copper K_α radiation
λ^*	Space charge width in the Mott – Schottky case, as defined in Eq. 2.33
λ	Debye length as defined in Eq. 2.28
μ_j^0	Standard chemical potential of an arbitrary mobile defect *j*
μ'_j	Chemical potential of an arbitrary mobile defect *j*

$\widetilde{\mu}_j$	Electrochemical potential of an arbitrary mobile defect *j*
ϕ	Electrostatic potential
ρ	Local charge density
$\sigma^{\parallel}$	Conductivity parallel to the interface
Σ	Charge density
σ_{bulk}	Bulk conductivity
σ_j	Partial electrical conductivity of an arbitrary *j* charge carrier
$\sigma_{V_O^{\bullet\bullet}}$	Oxygen vacancies partial conductivity
σ	Total electrical conductivity
τ	Relaxation time constant
θ	Bragg angle
Θ	Degree of influence in a symmetrical Gouy Chapmann case, as defined in 2.27

INDEX OF FIGURES

ACKNOWLEDGEMENTS

I would like to express my deep gratitude to Prof. Dr. Joachim Maier for having given me the possibility of doing my Ph.D. in his group. His constructive suggestions and discussions with him improved enormously the quality of this dissertation.

I would like to thank Prof. Dr. Anke Weidenkaff and Prof. Dr. Thomas Schleid for having accepted of being part of my Ph.D. exam committee.

Particular gratitude goes to my direct supervisor Dr. Giuliano Gregori, with whom I had the pleasure to work every day during my Ph.D. Our daily discussions, his suggestions, his constant support were a great support to me.

I sincerely appreciated all the people who gave a contribution to make this work possible. I want to thank Dr. Gennady Logvenov for the helpful scientific discussions. Georg Christiani and Benjamin Stuhlhofer for the precious advices on PLD sample preparation.

I gratefully thank Dr. Yi Wang, Dr. Prof. Peter van Aken for the TEM characterization and helpful scientific discussions.

I would like to thank Dr. Rotraut Merkle for the precious advices in many occasions.

I express my gratitude to my colleagues Chia-Chin Chen, Federico Baiutti, Michael Weissmayer for our fruitful discussions, which helped me to understand and solve many problems. I gratefully thank also former colleagues who helped me at the beginning of my PhD for their helpful suggestions: Dr. Piero Lupetin, Dr. Marcus Göbel and Dr. Kiran Adepalli.

Annette Fuchs, Uwe Traub, Udo Klock and Peter Senk are thanked for their technical support. A special thank goes to Sofia Weiglein for her precious help.

Curriculum Vitae
ELISA GILARDI

Personal Information:
Name: Elisa Gilardi
E-mail: e.gilardi@fkf.mpg.de
Nationality: Italian
Date of Birth: 27/07/1986

Current position:

- *June 2011 - Present:* PhD candidate at Max Planck Institute for Solid State Research, Stuttgart, department of Physical chemistry supervised by Prof. Dr. Joachim Maier

Education and training:

- *1st October 2009 - 31st March 2010:* Erasmus period at Technische Universitët Braunschweig at Physicalische Chemie Institute in "Laser chemistry" group.
- *September 2008 - September 2010*
Msc in Chemistry; University of Pavia (Italy). Final Mark: 110/110.
Thesis title: 'Catalytic conversion of biogas in fluidized bed reactor supported by plasma'.
- *October 2005- September 2008*
Bsc in Chemistry; University of Pavia (Italy). Final Mark: 110/110
Thesis title: 'Application of micellar system with lipophilic ligands for removal of metal ions by ultrafiltration in watery solution'.
- *October 2005 - September 2010*
Alumna at Collegio Nuovo-Fondazione Sandra e Enea Mattei, Pavia (Italy).
- *September 2001- July 2005*
High School Diploma, Linguistic School. Linguistic High School 'Angelo Omodeo', Mortara (Italy) Final Mark: 100/100.

Publications:
K.Song, H. Schmid, V. Srot, E. Gilardi, G. Gregori, K. Du, J. Maier, and P. A.van Aken, APL Materials 2, 032104 (2014)
E. Gilardi, G. Gregori, Y. Wang, W. Sigle, P.A. van Aken, J. Maier, Interfacial dislocation effects on the ionic transport of $Y_2Zr_2O_7$ epitaxial thin films; to be submitted.
E. Gilardi, G. Gregori, J. Maier
Characterization of the strain effect on $Y_2Zr_2O_7$ / 8 % Yttria stabilized zirconia multilayers; in preparation